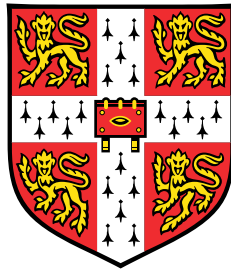


Spatially Resolved Charge Transport and Recombination in Metal-Halide Perovskite Films and Solar Cells



Gregory Demaray Tainter

Department of Engineering
University of Cambridge

This dissertation is submitted for the degree of
Doctor of Philosophy

Abstract

Metal-halide perovskites show great promise as solution-processable semiconductors for efficient solar cells and LEDs. In particular, the diffusion range of photogenerated carriers is unexpectedly long and the luminescence yield is remarkably high. While much effort has been made to improve device performance, the barriers to improving charge transport and recombination properties remain unidentified.

I first explore charge transport by investigating a back-contact architecture for measurement. In collaboration with the Snaith group at Oxford, we develop a new architecture to isolate charge carriers. We prepare thin films of perovskite semiconductors over laterally-separated electron- and hole-selective materials of SnO_x and NiO_x , respectively. Upon illumination, electrons (holes) generated over SnO_x (NiO_x) rapidly transfer to the buried collection electrode, leaving holes (electrons) to diffuse laterally as majority carriers in the perovskite layer. We characterise charge transport parameters of electrons and holes, separately, and demonstrate that grain boundaries do not prevent charge transport. Our results show that the low mobilities found in applied-field techniques do not reflect charge diffusivity in perovskite solar cells at operating conditions. We then use the back-contact architecture to investigate recombination under large excess of one charge carrier type. Recombination velocities under these conditions are found to be below 2 cm s^{-1} , approaching values of high quality silicon and an order of magnitude lower than under common bipolar conditions. Similarly, diffusion lengths of electrons and holes exceed $12 \text{ }\mu\text{m}$, an order of magnitude higher than reported in perovskite devices to date. We report back-contact solar cells with short-circuit currents as high as 18.4 mA cm^{-2} , giving 70% external charge-collection efficiency. We then explore the behaviour of charge carriers in continuously illuminated metal-halide perovskite devices. We show that continuous illumination of perovskite devices gives rise to a segregated charge carrier population, and we find that the distance photo-induced charges travel increases significantly under these conditions. Finally, we examine intermittancy in the photoluminescence intensity of metal-halide perovskite films.

To my loving family.

Declaration

I hereby declare that except where specific reference is made to the work of others, the contents of this dissertation are original and have not been submitted in whole or in part for consideration for any other degree or qualification in this, or any other university. This dissertation is my own work and contains nothing which is the outcome of work done in collaboration with others, except as specified in the text and Acknowledgements. This dissertation contains fewer than 65,000 words including appendices, bibliography, footnotes, tables and equations and has fewer than 150 figures.

Gregory Demaray Tainter
November 2018

Acknowledgements

I have been fortunate enough to benefit from the support and assistance of many people, most of whom I hope I have acknowledged here. To begin, I would like to thank my supervisor Dr Hannah Joyce for her support and advice throughout my PhD. In addition, I am thankful for the excellent guidance Dr Felix Deschler has provided since taking me under his wing in 2016. I would also like to thank Prof Richard Phillips for providing initial supervision and training me in all things optics. Finally, I would like to acknowledge Prof Sir Richard Friend for additional supervision and discussion.

I would like to thank the excellent film and device fabrication experts I have worked with on this PhD. Specifically Dr Maximilian Hörantner at Oxford University not only for fabricating back-contact devices, but also for important discussions to develop our understanding of device function. I am grateful to Dr Cheng Li at the University of Bayreuth, both for supplying flickering perovskite films, and for his visit and contributions in a blistering week of measurements and discussion. In addition, thanks to Mojtaba Abdi-Jalebi for providing vertical devices to test our ideas on. I would also like to acknowledge the hard work put in by Haralds Āboliņš to produce thin films and Suhas Mahesh at Oxford University for his work on back-contact devices.

I am grateful to Dr Luis Pazos-Outón, not only for discussions and collaborations on back-contact devices, but for support, generating ideas, and always challenging me and bringing out the best. Thanks are also due to Dr Ravichandran Shivanna, not only for helping me build and maintain our setup, but also for discussion and helping me generate new ideas. I am grateful to Dr Robin Lamboll, for modelling the investigated architecture and for helping me work through my ideas even as he began his new job. In addition, I would like to thank Sarwat Baig, the Deschler group, especially Lissa Eyre, and the wider OE group; especially Dr Jasmine Rivett, Dr Johannes Richter, and Dr Nate Davis. Each of them have made fantastic colleagues and friends both in and out of the lab.

Funding for this work was generously provided by the Cambridge Overseas Trust and the NanoDTC, and I am grateful to all those involved who have given their support.

I would like to thank the OE staff, particularly Roger Beadle, Alex Crook and Richard Gymer, for their hard work supporting our research endeavours. I am grateful to the NanoDTC administrators, especially Dr Karishma Jain, for supporting and facilitating a wonderful experience. Thank you to Dr Krishna Kumar for producing the base Latex template which I have used for this thesis.

Finally, I would like to thank those outside the lab who have made this possible. My NanoDTC cohort for the fantastic years we have spent here in Cambridge. My Blüten/Munich family for supporting me from abroad and harbouring me when I needed to get out of Cambridge. Becca, for her patience and dedication to taking me away from science every now and again. And to my family, who have continually supported me however far away I manage to get.

Contents

List of Figures	xv
List of Tables	xvii
Nomenclature	xix
1 Introduction	1
2 Background	5
2.1 Metal-halide perovskite semiconductors	5
2.1.1 Crystal structure	5
2.1.2 Electronic state structure	7
2.1.3 Photoresponse of metal-halide perovskites	10
2.1.4 Processing of metal-halide perovskites	16
2.2 Transport in crystalline semiconductors	18
2.2.1 Carrier mobility and diffusivity	18
2.2.2 Charge carrier scattering	21
2.2.3 Carrier transport measurement techniques	23
2.3 Recombination in crystalline semiconductors	30
2.3.1 Band-band recombination	31
2.3.2 Shockley-Read-Hall recombination	32
2.3.3 Surfaces and grain boundaries	33
2.3.4 The continuity equation, diffusion length, and recombination in perovskites	34
2.4 Junctions in semiconductor devices	35
2.4.1 The p - n homojunction	35
2.4.2 Junctions in metal-halide perovskite devices: semiconductor heterojunctions	38

2.5	Principles of photovoltaic device operation	39
2.5.1	Working mechanism	40
2.5.2	Theoretical and practical efficiency limits	41
3	Experimental methods	45
3.1	Sample fabrication	45
3.1.1	Back-contact device preparation	45
3.1.2	Perovskite layer deposition for contacted films	47
3.1.3	Mixed-halide perovskite films in flickering study	47
3.1.4	Mixed-cation “sandwich” devices	48
3.2	Device testing	49
3.3	Principles of phase-sensitive detection	49
3.4	Photoluminescence spectroscopy	51
3.4.1	Photoluminescence quantum yield measurements	51
3.4.2	Confocal photoluminescence microscopy	51
3.4.3	Time-correlated single photon counting	53
3.5	Scanning photocurrent microscopy	54
3.6	Comparing laser intensities and obtained photocurrent amplitudes	55
4	Electron and hole transport dynamics in polycrystalline perovskite films	57
4.1	Background and motivation	58
4.2	Characterising back-contact devices	59
4.3	Scanning photocurrent spectroscopy on back-contact architectures	61
4.4	Characterising charge carrier transport	64
4.5	Discussion	70
4.6	Conclusion	72
5	Effects of illumination on perovskite materials and devices	73
5.1	Background and motivation	73
5.2	Continuous background illumination of vertical devices	75
5.3	Effects of background illumination on back-contact devices	80
5.4	Effects of background illumination on charge transport	86
5.5	Influence of charge density and discussion	88
5.6	Conclusion	92

6	Recombination in polycrystalline perovskite films and devices	93
6.1	Background and motivation	93
6.2	Probing recombination in operating back-contact devices	94
6.3	Recombination in isolated perovskite films	97
6.4	The effect of charge segregation on steady-state photoluminescence . .	100
6.5	Modelling device behaviour	101
6.6	Discussion	107
6.7	Conclusion	108
7	Photoluminescence flickering in perovskite thin films	109
7.1	Background and motivation	109
7.2	Changes in PL spectra upon flickering	110
7.3	Changes in TRPL decays upon flickering	115
7.4	Influence of atmosphere	118
7.5	Discerning emissive levels and discussion	119
7.6	Conclusion	122
8	Summary and Outlook	125
	References	129

List of Figures

2.1	Schematic of perovskite crystal structure	6
2.2	Calculated metal-halide band structure	11
2.3	Metal-halide perovskite absorption coefficient	14
2.4	Perovskite film deposition techniques	16
2.5	Mobility vs temperature of GaAs	22
2.6	Charge mobility via the time-of-flight technique	25
2.7	Scanning photocurrent measurement	29
2.8	Abrupt p - n junction	36
2.9	Heterojunctions in metal-halide perovskite materials	39
2.10	Current-voltage characteristics of a solar cell	40
2.11	Schematic of a typical perovskite solar cell	44
3.1	Multiplication of signals to enable lock-in based detection	50
3.2	Schematic of confocal measurement	52
3.3	Schematic of TCSPC measurement	53
3.4	Schematic of SPCM measurements	55
4.1	QIBC devices: architecture, performance, and SPCM characterisation .	60
4.2	Schematic of nanostructured architecture and photocurrent measurement	62
4.3	Optical and Electron Micrographs of investigated films	63
4.4	Photocurrent obtained at varying excitation frequencies	65
4.5	Photocurrent amplitude and phase with varying excitation—junction distance	67
4.6	Photocurrent and hole diffusion length vs local average laser power . .	69
5.1	Vertical device architecture and large-area time resolved PL measurement setup	75

5.2	Effect of applied bias and background illumination on time-resolved photoluminescence of a perovskite device	79
5.3	Schematic of photocurrent measurements with background illumination	81
5.4	SPCM measurement with background illumination	82
5.5	Photocurrent amplitude and phase measured at varying distance from the electrode junction with background illumination	85
5.6	Photocurrent amplitude and extraction length with varying laser intensities	87
5.7	Simulated carrier densities versus distance from excitation point for each investigated illumination condition	89
6.1	Comparison of photoluminescence spectra and decay over device active area	95
6.2	Time-resolved photoluminescence measurements of perovskite films deposited over electrode materials	99
6.3	Modelling PL quenching as a result of charge segregation	102
6.4	Predicted charge distributions and photocurrents for varying excitation—junction separations	105
7.1	Measurement of the temporal evolution of local PL spectra	111
7.2	Changes in PL spectra with time	112
7.3	Evolution of PL intensity and wavelength with time	114
7.4	Tracking the temporal evolution of PL decays in time-resolved PL measurements	115
7.5	Temporal evolution of PL_0 and PL lifetime	116
7.6	Evolution of count rate, PL_0 , and PL lifetime	118
7.7	Evolution of PL intensity with exposure to dry N_2	120
7.8	Discerning emission levels via comparing PL intensity and wavelength .	123

List of Tables

2.1	Comparison of transport measurement techniques	30
3.1	Comparison of photocurrent and laser intensity	56
4.1	Survey of obtained transport parameters	71
6.1	Summary of PLQE and TRPL measurements of perovskite films on electrode materials	98
6.2	Parameters used in device modelling	106

Nomenclature

Roman Symbols

E_g	bandgap energy
k_B	Boltzmann's constant
D	charge carrier diffusion coefficient
j	current density
L_D	charge carrier diffusion length
m^*	charge carrier effective mass
n	electron density
q	elementary charge
p	hole density
\hbar	reduced Planck constant
a	monomolecular recombination coefficient
b	bimolecular recombination coefficient
T	temperature
\mathbf{k}	wave vector

Greek Symbols

ω	frequency
μ	charge carrier mobility

τ charge carrier scattering time

τ_l charge carrier lifetime

τ_{Lum} luminescence lifetime

Subscripts

0 initial value, e.g. PL_0 is PL intensity at time zero

p hole population

h hole

n electron population

e electron

i intrinsic value or initial state

OC open-circuit

SC short-circuit

Acronyms / Abbreviations

DFT density functional theory

EBIC electron beam-induced current

EQE external quantum efficiency

FA formamidinium ($HC(NH_2)_2^{7+}$)

FET field-effect transistor

FTO fluorine-doped tin oxide

IBC interdigitated back-contact

LED light-emitting diode

MA methylammonium ($CH_3NH_3^{7+}$)

PV photovoltaic

PLQE photoluminescence quantum efficiency

PL photoluminescence

PMMA poly(methyl methacrylate)

QIBC quasi-interdigitated back-contact

SPCM scanning photocurrent microscopy

SRH Shockley-Read-Hall

THz terahertz spectroscopy

TCSPC time-correlated single photon counting

TRPL time-resolved photoluminescence

TRMC time-resolved microwave conductivity

TOF time-of-flight

WLB white light background

Chapter 1

Introduction

Despite increasing concern over the impact of fossil fuels on global climate, the growing energy demands of the world population continues to drive rising CO₂ emissions. Indeed, the International Energy Agency projects global energy demands to increase by 30% by 2040.¹ To reduce our impact on climate, and to enable more localised energy production, development and deployment of renewable energy sources is of critical importance.

Almost all activity on Earth is powered by the sun. The wind, plant and animal life, and, more indirectly, fossil fuel-driven human activity are each the result of the energy delivered to our planet via solar radiation. Indeed, the sunlight reaching the surface of the Earth each hour has enough energy to power global civilisation for a year.² Developing means of more directly harvesting this enormous quantity of energy will significantly reduce the impact our energy-hungry society has on global climate and atmospheric pollution.

Photovoltaic solar cells directly convert sunlight into electricity, without moving parts or any effect on the environment during operation. Due to high cost of manufacture, solar cells have seen limited use up to now, perhaps best-known in iconic photographs of space-based telescopes and manned space stations. In the previous decade, breakthroughs in production have resulted in an exponential growth in the deployment of silicon solar cells. Indeed, the share of renewable electricity production in the UK has almost reached 25%, with solar PV generation increasing by 38% in 2016 to reach 11% of renewable electricity production in the UK.³ 95% of solar cells employ crystalline silicon as the absorbing material, which, in Northern Europe, require ~2.5 years of continuous operation to ‘payback’ the energy required to produce them.⁴ This does not include the energy required to transport modules.

This increase in silicon PV deployment has been driven by a significant drop in the price and energy cost of fabricating silicon solar cells. Despite these improvements, the production of silicon is inherently energy expensive, requiring high-temperature processes in excess of 1000 °C. To avoid such energy costs, several semiconducting systems which are capable of low-temperature processing have been developed, including organic semiconductor devices and dye-sensitised solar cells. These classes of devices have struggled with poor efficiency and/or limited device lifetime, however, and therefore the search for more suitable materials has continued.

Metal-halide perovskite materials are a class of materials which are solution-processable much like organic systems, yet exhibit many of the properties of crystalline perovskite materials: low energetic disorder, long charge diffusion ranges, and high luminescence yields. Thus, they have generated a great deal of research interest since first being incorporated into solar cells in 2009. This has yielded impressive results, with efficiencies of metal-halide perovskite-based devices exceeding 23% in the lab,⁵ approaching the efficiencies of the highest-performing silicon devices.⁶

In many ways, this blistering pace of device development has outstripped the pace of fundamental studies of material properties. Many questions remain concerning the behaviour of metal-halide perovskite materials: What effect does polycrystallinity have on charge transport? What determines the values of transport properties, and which techniques provide accurate measurements? What is the effect of electrodes on charge carriers in films and devices? What is the origin of spatial variation in luminescence and device performance? This thesis aims to both outline a means of probing these questions, as well as investigating the origins of some of these effects. The work focuses on spatially- and temporally-resolved measurements of luminescence and current resulting from photoexcitation.

In the next chapter, we will outline relevant background theory and more thoroughly introduce the metal-halide perovskite material system. As this is a study based on photoluminescence and photocurrent measurements, we focus on the response of metal-halide perovskites to illumination and the nature of transport and recombination in crystalline semiconductors. In addition, we discuss the behaviour of semiconductor junctions and the operating principles of solar cells.

Chapter 3 details sample preparation and methods of measurement. In addition, principles of photocurrent measurements via lock-in based detection are outlined. Finally, details of how laser intensities are compared are provided.

In Chapter 4, we investigate an architecture which employs charge-selective electrodes to isolate one charge carrier type within a perovskite film. We characterise the transport behaviour of electrons and holes individually, and find diffusivities of $D_n = 0.13 \text{ cm}^2 \text{ s}^{-1}$ and $D_p = 0.07 \text{ cm}^2 \text{ s}^{-1}$. We investigate the range of charge transport, and find unexpectedly long diffusion lengths exceeding $12 \text{ }\mu\text{m}$. Finally, we present a quasi-interdigitated back-contact (QIBC) solar cell with a short-circuit current of 18.4 mA cm^{-2} , reaching 70% external quantum efficiency.

In Chapter 5 we investigate the behaviour of the photo-induced charge carrier population. To do so, we incorporate the application of a steady-state white light background illumination on time-resolved photoluminescence and photocurrent measurements. We study the effect of discontinuous laser illumination on steady-state segregated charge carrier populations. We find evidence that the presence of steady-state segregated charge populations reduces the effect of charge segregation in pulsed measurements on vertical devices. Furthermore, we find that charge transport properties within segregated carrier populations is improved. Indeed, we show that at low laser-induced charge carrier densities, charge extraction lengths in back-contact measurements increase significantly as a result of background illumination, reaching $25 \text{ }\mu\text{m}$.

Next, Chapter 6 investigates the low recombination rates found in photocurrent measurements more closely. We study films and devices of perovskite materials deposited over charge-selective electrodes. We show that charge segregation on introduction of charge-selective electrodes reduces the total charge recombination rate, and recombination velocities are found to be below 2 cm s^{-1} . We model this charge segregation behaviour, and investigate its influence on photocurrent measurements.

Chapter 7 investigates an unexpected phenomenon in perovskite films: intermittency in photoluminescence. We use spatially- and temporally-resolved measurements to investigate this “flickering” in photoluminescence, and identify potential origins of the effect. We find that the behaviour of flickering films is highly complex, especially relative to blinking perovskite nanocrystals. However, we find strong evidence that “supertraps,” highly efficient nonradiative recombination pathways reported in nanocrystal systems, contribute to flickering behaviour in films.

Chapter 2

Background

2.1 Metal-halide perovskite semiconductors

This section introduces the metal-halide perovskite material, focusing on the methylammonium lead triiodide composition: $\text{CH}_3\text{NH}_3\text{PbI}_3$ (subsequently referred to as MAPbI_3). Studies of metal-halide perovskite structures date back to 1893 when CsPbI_3 and CsPbBr_3 were first reported.⁷ These compounds were not identified as perovskite materials until further characterisation by Møller,⁸ who also first reported on the photoconductivity of the material in 1958. The first synthesis of inorganic-organic hybrid perovskite materials incorporating methylammonium were reported by Weber in 1978.⁹ Subsequently, a large body of work was done by Mitzi who characterised the inorganic-organic material's synthesis and electronic and structural properties over 20 years.¹⁰ Interest in metal-halide perovskites gained wider attention upon reports of solar cells incorporating the material by: Kojima et al. in 2009,¹¹ who reached 3.8% efficiency, and Lee et al. in 2012,¹² who reported a device with 10.9% efficiency. A remarkable pace of development over the subsequent six years has resulted in devices exceeding 23% efficiency⁵ and has initialised efforts to develop commercial applications for metal-halide perovskite materials.¹³

2.1.1 Crystal structure

The term *perovskite* refers to a crystal structure having the general chemical composition: ABX_3 , where A and B are cations of different sizes and X are anions. B cations have 6-fold coordination, leading to BX_6 octahedra with larger A cations located at octahedron faces. The name derives from the Russian mineralogist L. A. Perovski, who characterised

the structure of CaTiO_3 . There are several metal oxides which can crystallise in the perovskite structure, and properties such as ferroelectricity of perovskite compounds have been of interest.¹⁴

A schematic of the inorganic-organic perovskite crystal structure of most interest for solar cell applications is presented in Figure 2.1, where methylammonium (MA) molecules act as A cations. The material undergoes phase transitions at varying temperatures, having a high-temperature cubic phase, a room-temperature tetragonal phase, and a low temperature orthorhombic phase.¹⁵ All measurements here are performed at room temperature, when MAPbI_3 is in a tetragonal phase which has the space group $I4/mcm$.¹⁶

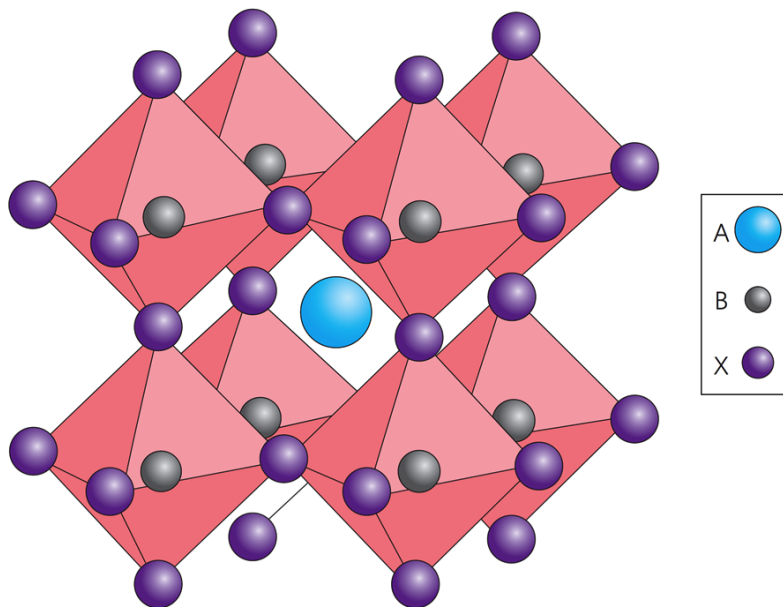


Figure 2.1 Schematic of the perovskite crystal structure. In the investigated inorganic-organic hybrid methylammonium perovskite material, an organic CH_3NH_3 molecule (A) sits at the centre of lead-iodide octahedra (B,X). Figure reproduced with permission from Ref. [17].

This general structure has been found to be robust to variation of constituent components, allowing variation in the A cation and X halide to tune properties while still maintaining impressive device performance. For example, replacing the methylammonium (MA) with formamidinium (FA) moves the bandgap from 1.55 eV to 1.45 eV. Similarly, replacing iodide in the MAPbI_3 system with chloride or bromide results in bandgaps of 2.3 and 3.1 eV.^{18,19} This tuning of perovskite composition has impacts beyond material bandgap, however, including on the stability of obtained crystal phases,²⁰ electronic transport properties,²¹ and carrier lifetimes.²² In addition, it has

been shown that optoelectronic devices of high efficiency can be obtained by replacing the organic A cation with inorganic cesium, though the bandgap of these all-inorganic materials remains too high and only a 10% efficient device has been demonstrated.²³ It has been shown that mixing compositions results in intermediate material properties, resulting in a large variety of possible compositions and many of the highest performing materials are mixed-cation, mixed-halide inorganic-organic perovskites; such as the $\text{Cs}_{0.05}\text{MA}_{0.16}\text{FA}_{0.79}\text{Pb}(\text{I}_{0.83}\text{Br}_{0.17})_3$ composition which has produced cells with 21.2% efficiency.²⁴

Finally, there is interest in replacing the Pb cation due to the toxicity of Pb. There have been several reports of lead-free perovskite materials with impressive charge diffusion ranges, such as silver-bismuth- ($\text{Cs}_2\text{AgBiBr}_6$)²⁵ and tin-based perovskites (FASnI_3).²⁶ To-date the highest-performing devices have relied on tin-based perovskites which are approaching 10% efficiency.^{27,28} Thus, the tuning of device optical, electrical, and chemical properties via changes in composition aims to deliver a material with an ideal bandgap (1.2 – 1.4 eV, as defined by the Shockley-Queisser limit),²⁹ maximised conversion efficiency and material stability, and minimised toxicity.

2.1.2 Electronic state structure

The dielectric constant of metal-halide perovskite materials is high,³⁰ resulting in excited charges acting as free charge carriers. Free charge carriers delocalise over a crystal lattice, and their behaviour is heavily dependent upon the nature and periodicity of the crystal. In order to describe the behaviour of free charge carriers within a semiconductor, we first introduce the concept of allowed electron energy bands which gives rise to the crystalline semiconductor bandgap. First, we consider the energy landscape of crystalline materials and construct the Hamiltonian for a perfect crystal:³¹

$$\mathcal{H} = K_Z + K_e + V_{Z-Z'} + V_{e-e'} + V_{e-Z} \quad (2.1)$$

which considers the energy of the nuclei (K_Z), the energy of the electrons (K_e), the interaction of nuclei ($V_{Z-Z'}$), the interaction of electrons ($V_{e-e'}$), and the interaction of electrons with nuclei (V_{e-Z}). This Hamiltonian is far too complex to solve, and therefore a series of assumptions and simplifications are made. First, electrons are split into core and valence electrons. Core electrons are those which are strongly bound to nuclei, and therefore are localised to form ionic cores centred at each nucleus. Valence electrons are those in higher electronic energy states, which are only partially

filled. Second, the Born-Oppenheimer approximation assumes that due to the large discrepancy in mass between the valence electrons and ionic cores, the ionic cores can be taken to be stationary. As a result of these approximations we reduce the Hamiltonian to the sum of three terms:³¹

$$\mathcal{H} = \mathcal{H}_{ions}(\mathbf{R}_j) + \mathcal{H}_e(\mathbf{r}_i, \mathbf{R}_{j0}) + \mathcal{H}_{e-ions}(\mathbf{r}_i, \delta\mathbf{R}_j) \quad (2.2)$$

where $\mathcal{H}_{ions}(\mathbf{R}_j)$ includes ionic motion under the influence of the ionic potential plus the time-averaged electronic potentials, $\mathcal{H}_e(\mathbf{r}_i, \mathbf{R}_{j0})$ is the Hamiltonian for electrons relative to the ion cores frozen into their equilibrium positions (\mathbf{R}_{j0}), and $\mathcal{H}_{e-ions}(\mathbf{r}_i, \delta\mathbf{R}_j)$ is the interaction of electrons with ions displaced from equilibrium by $\delta\mathbf{R}_j$, also known as the electron-phonon interaction.

The electronic band structure relates to allowed energy-momentum ($E - \mathbf{k}$) states for electrons in a periodic lattice, therefore we are interested in the Hamiltonian for electrons: $\mathcal{H}_e(\mathbf{r}_i, \mathbf{R}_{j0})$. The mean-field approximation assumes that every electron experiences the same average potential $V(\mathbf{r})$, which simplifies the system substantially. We then consider the one-electron Hamiltonian with a given eigenstate labelled \mathbf{k} . The Bloch theorem states that if potential energy $V(\mathbf{r})$ is periodic, as in periodic crystals, then the solution is a wavefunction $\psi_{\mathbf{k}}(\mathbf{r})$ of Schrödinger's equation:³¹

$$\mathcal{H}_{1e}\psi_{\mathbf{k}}(\mathbf{r}) = \left(-\frac{\hbar^2}{2m^*}\nabla^2 + V(\mathbf{r}) \right)\psi_{\mathbf{k}}(\mathbf{r}) = E_{\mathbf{k}}\psi_{\mathbf{k}}(\mathbf{r}) \quad (2.3)$$

take the form of a Bloch function:³²

$$\psi_{\mathbf{k}}(\mathbf{r}) = u_{\mathbf{k}}(\mathbf{r}) \exp(i\mathbf{k} \cdot \mathbf{r}) \quad (2.4)$$

where $u_{\mathbf{k}}(\mathbf{r})$ is a function which has the full periodicity of the potential. Thus, the eigenstates relate to a given wave vector \mathbf{k} , which is a plane wave within the crystal lattice. Allowed energy states arise from allowed wave vectors $\psi_{\mathbf{k}}$, and their energy can be calculated via the potential $V(\mathbf{r})$. By plotting the energies of electronic states ($E_{\mathbf{k}}$) versus possible wave vectors (\mathbf{k}), the electronic band structure is calculated.

These solutions are periodic relative to \mathbf{k} , as $\exp(i\mathbf{k} \cdot \mathbf{r}) = \exp(i(\mathbf{k} + 2\pi n) \cdot \mathbf{r})$. It is conventional, therefore, to consider solutions for $-\pi/a < \mathbf{k} < \pi/a$, where a is the period of the crystal, and this region is termed the first Brillouin zone. To build a basic understanding of how these systems form, we consider a one-dimensional lattice. Further, we examine the limiting case in which the periodic potential $V(\mathbf{r})$ is very

small while retaining the symmetry properties of our crystal. In this case, any function $e^{i\mathbf{K}_n \cdot \mathbf{r}}$ is an acceptable $u_{\mathbf{k}}$, and the energy of a wave vector \mathbf{k} is:

$$E = \frac{\hbar^2}{2m} |\mathbf{k} + \mathbf{K}_n|^2 \quad (2.5)$$

where \mathbf{K}_n is any lattice vector. For small lattice vectors, this approaches the free electron dispersion relation, $E \propto \mathbf{k}^2$, giving a parabolic relation. Increasing the wave vector, we approach π/a , and find two means of fulfilling the boundary conditions:³³

$$\psi_+ = \cos\left(\frac{\pi x}{a}\right), \quad \text{and} \quad \psi_- = \sin\left(\frac{\pi x}{a}\right) \quad (2.6)$$

Each function describes a standing wave, one with electron probability density peaking at ion positions (ψ_+), and one with probability density peaking between ions (ψ_-). Due to the higher potential away from ions, ψ_- will have a higher energy than ψ_+ , thus a discontinuity in energy will form at the edge of the Brillouin zone. In this way, bands of allowed electron energies are formed. In real semiconductors the situation becomes much more complex, with bands often overlapping between varying Brillouin zones or wave vector directions. In a semiconductor, a discontinuity between allowed energy states forms between the highest occupied electronic states and the lowest unoccupied electronic states. The high-energy, occupied band is called the valence band, while the lowest-energy, unoccupied band is termed the conduction band. The difference in energy between the minimum allowed energy in the conduction band and the highest available energy in the valence band is called the bandgap, and is of great interest especially for optical and electronic properties. Due to the fundamental importance of material band structures, various methods have been developed to calculate them, including density functional theory (DFT) and the pseudopotential method.^{31,34}

Briefly, we introduce several influences band structure have on the optical and electronic properties of materials. First, the bandgap between occupied and unoccupied states determines the energy of allowed electronic transitions. This influences optical properties as it determines the wavelengths of light which are absorbed and emitted by a material. The size of the bandgap also determines the number of carriers which, for a given temperature, are within the conduction band. Therefore the bandgap influences the relationship between electrical conductivity and temperature. Second, the extrema of the valence and conduction bands can either lie at the same wave vector \mathbf{k} , or may be offset in \mathbf{k} -space. When the extrema have identical \mathbf{k} vectors, the material is termed a direct semiconductor. In this case, electrons in the conduction band which settle

to their minimum energy, and empty states in the valence band (holes) which rise to their maximum energy within the valence band, tend toward the same \mathbf{k} vector. In an indirect semiconductor, the maximum of the valence band and the minimum of the conduction band have different \mathbf{k} vectors, and as a result recombination of electrons and holes requires a transfer of momentum. As the momentum of a photon is very small, electronic transitions with a change in \mathbf{k} vector require a phonon and become less probable. The classic example of this are the two semiconductors Si and GaAs. Si is an indirect semiconductor, and is a relatively weak absorber and emitter of light but benefits from very extended charge diffusion ranges. GaAs is a direct semiconductor, and is an efficient absorber and emitter of light, but relative to Si charge diffusion ranges are reduced. Finally, we note that the quadratic relationship of energy to wave vector: $E = \hbar\mathbf{k}^2/2m$, includes a mass term in the denominator. In real semiconductors, the E - \mathbf{k} relationship is approximated similarly with an effective mass, m^* , which is related to charge transport and absorption in subsequent sections.

There have been several reports which have calculated the band structure of perovskites.³⁵⁻³⁷ An example of a calculated band structure of MAPbI₃ is presented in Figure 2.2. We observe that MAPbI₃ is predicted to have a direct transition, with a bandgap of ~ 1.6 eV. Further details related to the nature of the bandgap are presented in Section 2.1.3. The band structure has been predicted to be primarily composed of electronic states within the lead-halide octahedra, while the organic cation acts primarily as a spacer which affects the bandgap.³⁸ Strong spin-orbit coupling is present in lead-halide perovskites as a result of the heavy lead atoms.^{39,40}

2.1.3 Photoresponse of metal-halide perovskites

As halide-perovskite materials are of great interest for their application to solar cells, we first discuss the absorption of light in a crystalline semiconductor. This process is described quantum mechanically as the coupling of photons and electrons using time-dependent perturbation theory. We then describe the probability of transition per time (Ω_{fi}) between a final (f) and an initial state (i) by Fermi's golden rule:⁴¹

$$\Omega_{fi}(\hbar\omega) = \frac{2\pi}{\hbar} |\mathbf{H}_{fi}'|^2 \delta(E_f - E_i - \hbar\omega) \quad (2.7)$$

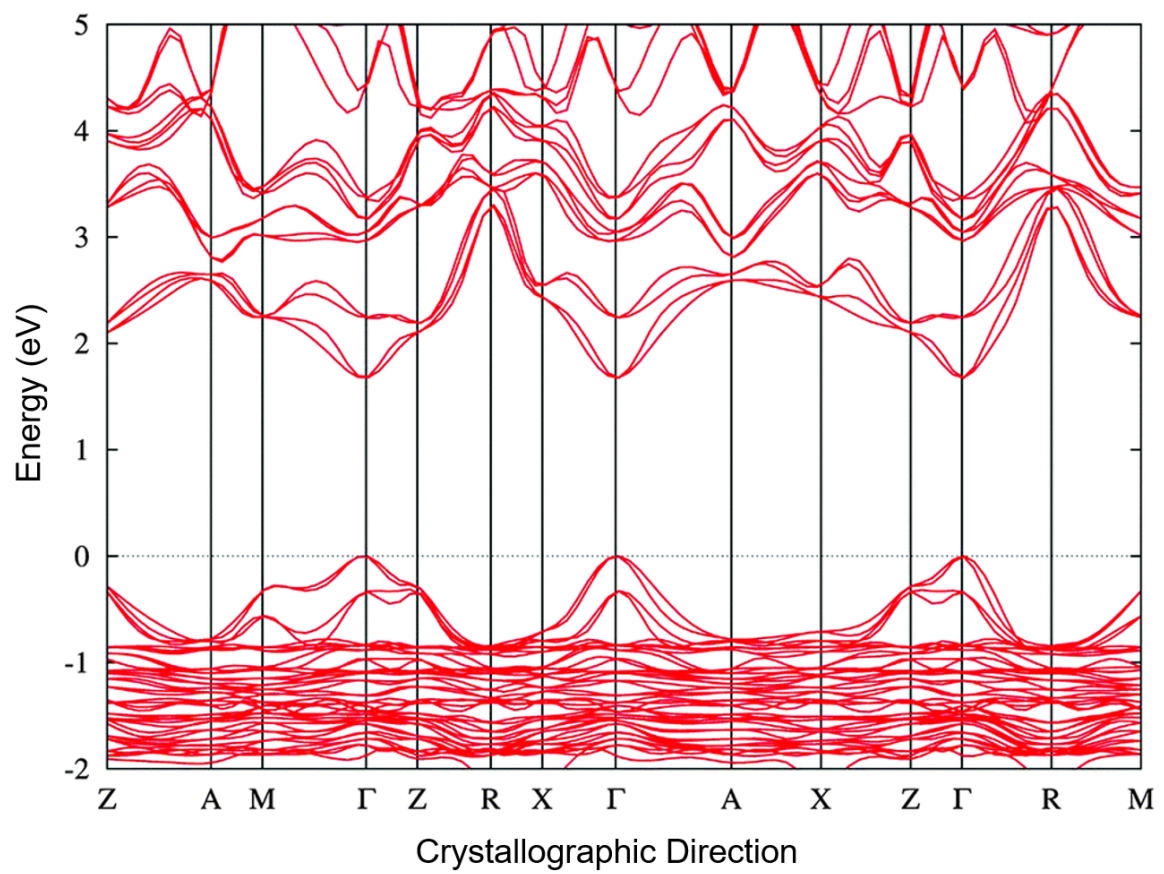


Figure 2.2 Calculated band structure of MAPbI₃. Note that at the Γ point a direct bandgap is predicted. Figure reproduced with permission from Ref. [35].

where $\hbar\omega$ is the photon energy, and $E_{f,i}$ are the energies of the final and initial states. Here, \mathbf{H}'_{fi} is the matrix element:

$$\mathbf{H}'_{fi} = \langle \psi_f | \mathcal{H}' | \psi_i \rangle \quad (2.8)$$

which encloses the perturbation Hamiltonian (\mathcal{H}') and the unperturbed final and initial states ($\psi_{f,i}$). The perturbation Hamiltonian includes contributions from the crystal and from the incident electromagnetic wave. Taking \mathbf{A} to be the vector potential of the electromagnetic field, the Hamiltonian for an electron within the field becomes:⁴¹

$$\mathcal{H}' = \frac{1}{2m} (\hbar\mathbf{k} - q\mathbf{A})^2 \quad (2.9)$$

where q is the fundamental electric charge. Using the electric dipole approximation to neglect the \mathbf{A}^2 term, the Hamiltonian becomes:

$$\mathcal{H}' = -\frac{q}{m} \mathbf{A} \mathbf{p} \approx q \mathbf{r} \cdot \mathbf{E} \quad (2.10)$$

where \mathbf{p} is the electric dipole moment of the electron, and \mathbf{E} the electric field of the incident light. To generalise this to find the dielectric function of a semiconductor with conduction and valence band Bloch functions (c and v), we assume \mathbf{A} is weak and apply this to 2.1.3 to find the absorption rate (R) for photons of a given energy $\hbar\omega$:⁴¹

$$R(\hbar\omega) = \frac{2\pi}{\hbar} \int_{\mathbf{k}_c} \int_{\mathbf{k}_v} |\langle c | \mathcal{H}' | v \rangle|^2 \delta(E_c(\mathbf{k}_c) - E_v(\mathbf{k}_v) - \hbar\omega) d^3\mathbf{k}_c d^3\mathbf{k}_v \quad (2.11)$$

where the integrals over the allowed energies for wave vectors \mathbf{k}_c and \mathbf{k}_v are the density of states of the conduction and valence band, respectively. Using E_{cv} as an abbreviation of $E_c(\mathbf{k}) - E_v(\mathbf{k})$, we return to considering simple isotropic, parabolic system as described in Section 2.1.2. In this case the E - \mathbf{k} relations is:⁴¹

$$E_{cv}(\mathbf{k}) = E_g + \frac{\hbar^2}{2} \left(\frac{1}{m_e^*} + \frac{1}{m_h^*} \right) \mathbf{k}^2 \quad (2.12)$$

where E_g is the bandgap and m_e^* and m_h^* are the effective masses of the electron and the hole, respectively. Neglecting the energy-dependence of the matrix element of the Hamiltonian, the absorption coefficient (α) is then determined by the square-root of

the joint density of states:

$$\alpha(E) \propto \frac{\sqrt{E - E_g}}{E} \approx \sqrt{E - E_g} \quad (2.13)$$

We observe that absorption increases with increasing photon energy. This ideal dependence of absorption often has a low-energy exponential tail. The Urbach tail is the result of transitions between states below the band edges, which is the result of disorder in a crystal. The absorption for energies below the bandgap becomes:⁴²

$$\alpha(E) \propto \exp\left(\frac{E - E_g}{E_U}\right) \quad (2.14)$$

where E_U is the characteristic width of the absorption edge, the Urbach parameter.⁴¹

As briefly introduced previously, MAPbI₃ has a bandgap of 1.55 eV, but incorporation of different halides can alter the material's photoresponse. For example, Figure 2.3 presents the absorption coefficient for mixed-halide compositions MAPb(Br_xI_{1-x})₃. Note that the onset of absorption is very high, with absorption coefficients reaching $1 \times 10^4 \text{ cm}^{-1}$ at energies of 0.1 eV above the bandgap.⁴³ In addition, the absorption is high over a large range of photon energies, stretching well into the ultraviolet range of the spectrum. Finally, the rise of the absorption edge shows a very small Urbach tail, with E_U less than 20 meV,⁴³ indicating a remarkably low level of energetic disorder. These properties are ideal for solar cell applications as high absorption allows for thin device active layers.

Up to now, we have considered the response of general crystalline materials and introduced the bandgap and absorption behaviour of metal-halide perovskite materials. The response of metal-halide perovskites to photoexcitation outside these two well-documented characteristics, however, is an exciting area of research. Here, we briefly provide an overview of several topics of interest.

First, the nature of the excited state was heavily debated in early reports. The absorption spectra of metal-halide perovskites has a shoulder at the band edge, which is particularly visible for MAPbBr₃ in Figure 2.3. At low temperatures, this shoulder develops into a peak clearly excitonic in nature. As a result, several reports suggested that relaxed charge carriers at room temperature were excitonic.⁴⁴⁻⁴⁶ However, the high photovoltaic device performance,⁵ the fluence dependence of photoluminescence,⁴⁷ the high carrier mobility,⁴⁸ detailed analysis of the excitonic peak,⁴⁹ and the low exciton

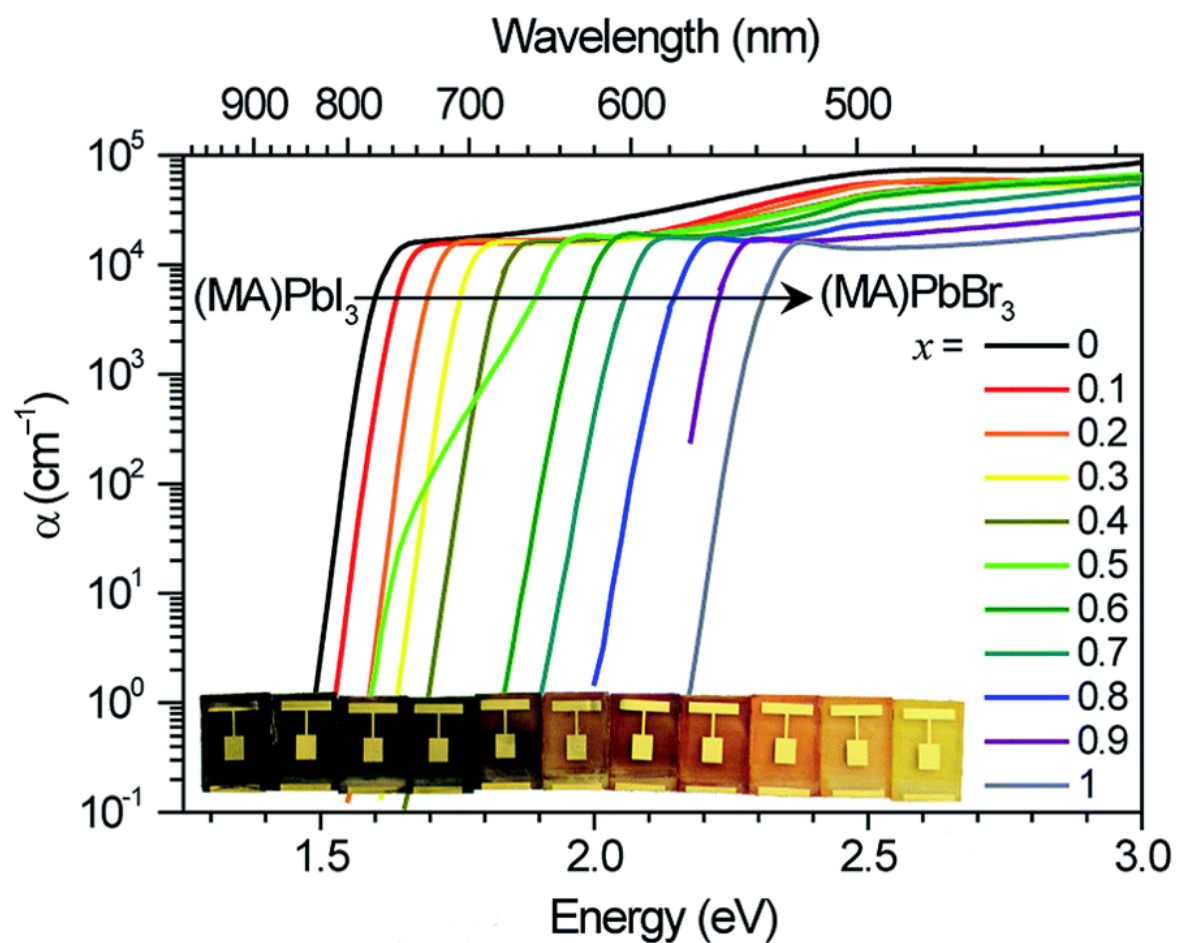


Figure 2.3 Absorption coefficient of $\text{MAPb}(\text{Br}_x\text{I}_{1-x})_3$ thin films. Inset: photograph of $\text{MAPb}(\text{Br}_x\text{I}_{1-x})_3$ photovoltaic devices from $x = 0$ to $x = 1$ (left to right). Figure reproduced with permission from Ref. [43].

binding energy⁵⁰ demonstrate that photoexcitation produces free carriers at room temperature in metal-halide perovskite materials.

Second, the nature of the bandgap remains a topic of debate, with several reports arguing that the conduction band states taken to be degenerate in Figure 2.2 are split in energy, with two minima in energy at $\mathbf{k} \neq \Gamma$. This has been predicted to be the result of the strong spin-orbit coupling within the material, which causes a Rashba^{40,51} or Dresselhouse splitting⁵² of the bands near band extrema. Such splitting has been predicted to cause a slightly indirect bandgap, which has been argued slows bimolecular recombination and extends charge carrier lifetimes.⁵² Strong experimental evidence of Rashba splitting has been demonstrated at low temperatures,⁵³ but recent experimental evidence indicates that emission is an inverse absorption process at room temperature.⁵⁴ While the exact nature of the bands at the bandgap remains open, the material appears to combine the high emissive performance of a direct semiconductor with surprisingly long charge carrier lifetime.

Third, the influence of photoexcitation on the chemical structure of hybrid perovskites is of great interest. It was reported early on that the photoluminescence of mixed-halide systems changes as a response to illumination,⁴³ and this behaviour has been explained via photo-induced halide migration.^{55,56} While the origins of photo-induced halide migration remains unclear, it has been suggested that such photo-induced migration contributes to the undesirable device characteristics of hysteresis in current-voltage measurements and degradation in performance.^{57,58} A large effort has been made to reduce hysteresis and photo-induced device degradation,⁵⁹⁻⁶¹ and recently a report has shown a stabilisation of intermediate photoluminescence behaviour of mixed-halide systems on incorporation of K cations.⁶² Somewhat counter intuitively to photo-induced ion migration, it has been shown that a period of “light soaking” can improve metal-halide perovskite device performance.⁶³ Several reports have suggested that a photo-induced structural transformation takes place,^{64,65} while others have argued that light-soaking effects are photochemical in nature and result in passivation of nonradiative loss channels.^{66,67}

Thus, despite the impressive development of perovskite-based photovoltaic devices, questions remain surrounding the material’s response to photo-excitation. We will introduce further questions in subsequent sections, but note that each of the previous investigations have been performed either on isolated films to better understand the behaviour of the active layer itself, or on vertical “sandwich” device architectures where both electron- and hole-collecting electrodes are present.

2.1.4 Processing of metal-halide perovskites

In addition to impressive device performance, the ease of processing metal-halide perovskite materials makes them ideal candidates for large-scale application. The highest-performing silicon devices are formed from high-quality single crystals,⁶ largely due to the additional recombination pathways and reduced diffusion ranges in polycrystalline materials.⁶⁸ The highest-performing metal-halide perovskite devices, however, have been achieved using polycrystalline thin films.⁵ Despite the tolerance to polycrystallinity of perovskite films, it has been shown that high film quality boosts performance.⁶⁹ In addition, it has been shown that single crystals of metal-halide perovskite materials show improved charge diffusion ranges. The influence of grain boundaries in polycrystalline films remains an active area of investigation, with some reports claiming that grain boundaries are detrimental due to increased recombination⁷⁰ or prevention of charge transport.⁷¹ On the other hand, reports have suggested that grain boundaries do not contribute to recombination^{72,73} or may even have beneficial effects on charge separation.⁷⁴ Here we outline several means of achieving metal-halide perovskite materials, with a focus on film deposition techniques.

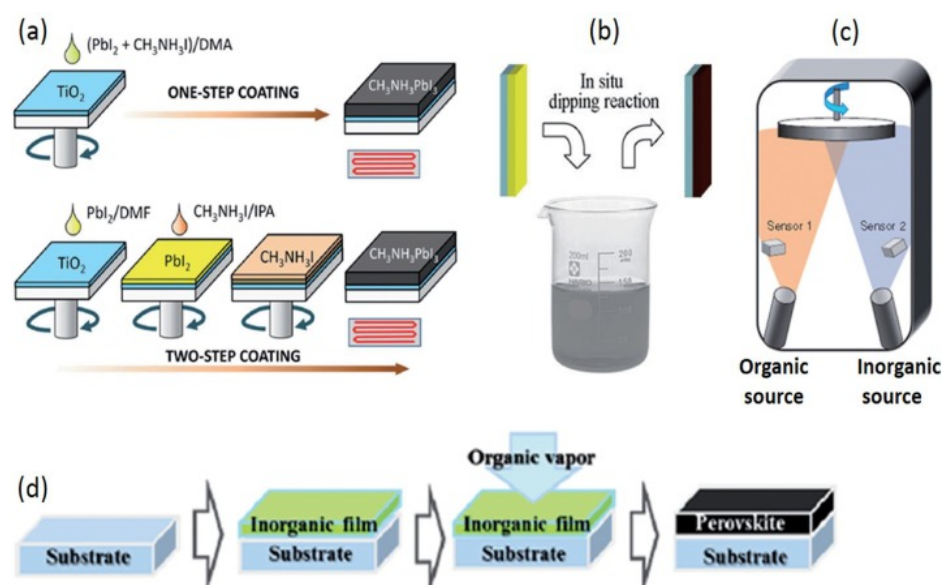


Figure 2.4 Perovskite film deposition techniques. (a) One-step and two-step spin coating techniques. (b) Soaking of PbI_2 films in organic-containing solvent to achieve perovskite film. (c) Coevaporation of organic (e.g. MAI) and inorganic (e.g. PbI_2) components. (d) Vapour-assisted solution processing, in which an inorganic film is first prepared via solution processing techniques such as spin coating, and subsequently exposed to an organic vapour to form the perovskite film. Figure reproduced with permission from Ref. [75].

Solution processing techniques

Solution processing is the most common means of achieving metal-halide perovskite films, due to the ease of fabrication and potential for large-scale cost-effective manufacture. Figure 2.4a presents the two primary methods of spin coating: (i) a one-step application of a premixed precursor solution, and (ii) a two-step application, first of PbI_2 followed by MAI. As the composition of the perovskite is often tuned with incorporation of other precursors, the one-step deposition process from a solution containing a defined mixture of precursors is the most common technique in use.⁶⁹ After spin coating the film is dried or annealed. In the two-step method, a layer of PbI_2 is deposited over the substrate, and subsequently a solution containing the organic component (e.g. MAI) is spin coated over this layer resulting in the formation of the perovskite material. The film morphology is controlled by varying several parameters: the rate and duration of spin coating, the temperature and atmosphere under which coating and annealing processes are accomplished, the type of solvents employed, and finally the surface treatment of the substrate onto which the perovskite is deposited. Indeed, it was further found that modifying the two-step process to include a dip or soak in the solution containing the organic component resulted in higher quality films (as in Figure 2.4b). The highest-performing ($>23\%$) devices have been achieved using a modified one-step deposition process termed the antisolvent method. This involves deposition of a single precursor solution via spin coating, but additionally an anti-solvent is introduced to the film during rotation.⁵

Vapour deposition techniques

Vapour deposition was first accomplished by Liu et al. via coevaporation of MAI and PbI_2 .⁷⁶ Evaporation is achieved within a N_2 -filled glove box and at 10^{-5} mbar pressure using an organic source (e.g. MAI) and an inorganic source (e.g. PbI_2) as in Figure 2.4c. Evaporated films are annealed after deposition, resulting in highly uniform nanocrystalline perovskite films. This technique has yielded devices exceeding 20% efficiency.⁷⁷ Despite this, vapour deposition is expensive relative to solution-based techniques as it requires high vacuum deposition. An intermediate method was developed by Chen et al.⁷⁸ which is similar to the two-step solution processing method, and is presented in Figure 2.4d. In this method, the substrate is coated in the PbI_2 layer, and subsequently only the organic material is deposited via vapour deposition and a final heating step enables interdiffusion to form the perovskite film.

Growth of single crystals

While perovskite devices have predominantly been composed of polycrystalline thin films, several groups have succeeded in producing single crystals of metal-halide perovskite materials.^{79–81} Single crystals are produced via crystallisation from solution or in vapour-assisted solution-based techniques. Mixed-halide perovskite single crystals have been obtained, and have even been incorporated into functioning photodetector devices.⁸² The low throughput of fabrication prevents broad applications for single crystals, but single crystals are a powerful platform to investigate fundamental properties of metal-halide perovskites⁷⁹ and show extended diffusion ranges relative to the polycrystalline material.⁸³

2.2 Transport in crystalline semiconductors

In the previous section, the high absorption of metal-halide perovskite materials was introduced which allows thin films of perovskite material to absorb the majority of the energy in sunlight. Once absorbed, the sun's energy must still be transported out of the device in order to accomplish solar energy harvesting. Metal-halide perovskite materials have been demonstrated to possess impressive charge transport ranges, which is vital to device operation. This thesis will examine the motion of charge carriers within perovskite films and devices. Therefore this section presents fundamental concepts of charge transport in crystalline semiconducting materials, and introduces several methods which have been employed to probe charge transport in metal-halide perovskites.

2.2.1 Carrier mobility and diffusivity

In the first section we described the formation of allowed electronic states of charge carriers, and introduced the concept of valence and conduction bands in semiconductors. In very simple terms, charge carrier motion is dependent on the number of excitations with the freedom to move, the degree of that freedom, and the quantity of driving force for charge motion. Excitation of electrons from the valence band to the conduction band results in an increase in the degrees of freedom of the excited electron, as the allowed electronic states at similar E - \mathbf{k} values will predominantly be unoccupied at low excitation density. Similarly, the absent electron in the valence band will act as a positive-charged *hole*, with its own transport dynamics and a large degree of freedom

of motion. Thus, the concentration of excited electrons (n) and holes (p) will have an effect on the magnitude of charge transported.

Such mobile charges will respond to any gradient in their energy landscape or Fermi level. We distinguish between two processes which carriers might undergo due to changes in Fermi level: **drift** and **diffusion**. Drift is the motion of charge carriers as a response to an electric field (\mathbf{E}), and diffusion is the motion resulting from gradients in charge carrier concentration ($\nabla n, \nabla p$).⁴¹ Here, we aim to introduce charge carrier motion due to these two driving forces, and will show how diffusion and motion within an applied field are linked.

To begin we consider the force (\mathbf{F}) on a single electron under the influence of an electric field:⁴¹

$$\mathbf{F} = m^* \frac{d\mathbf{v}}{dt} = \hbar \frac{d\mathbf{k}}{dt} = q\mathbf{E} \quad (2.15)$$

where \mathbf{v} is the velocity of the electron and m^* is the mass of the electron. By considering the effect on all conductive electrons over a time δt , we see that the \mathbf{k} vector for each electron is shifted by:

$$\delta\mathbf{k} = \frac{q\mathbf{E}}{\hbar} \delta t \quad (2.16)$$

which describes the change in the momentum of a population of electrons in the absence of any scattering processes, termed *ballistic* transport. In a real semiconductor impurities, phonons, defects, and surfaces contribute to scattering charge carriers. The relaxation-time approximation assumes that the probability for a charge carrier scattering event is proportional to the average carrier velocity.⁴¹ Thus, an average relaxation time or carrier scattering time τ is introduced: $d\mathbf{v}/dt = -\mathbf{v}/\tau$. The maximum velocity reached by an electron in a static electric field is then:⁴¹

$$\mathbf{v} = \frac{q\mathbf{E}\tau}{m^*} \quad (2.17)$$

We next introduce the concept of charge carrier mean free path λ_m , and an average charge carrier thermal velocity, $v_{th} = \lambda_m/\tau$. The current density (\mathbf{j}) fulfils Ohm's law:⁴¹

$$\mathbf{j} = qn\mathbf{v} = \frac{nq^2\mathbf{E}\tau}{m^*} = \sigma\mathbf{E} = qn\mu\mathbf{E} \quad (2.18)$$

where σ is the conductivity and μ is the mobility. Conductivity depends directly upon carrier concentration, while μ is the response of charges to applied field: $\mu = v/E$. Here we note that the effective mass m^* is related to the curvature of the band structure for each charge (E- \mathbf{k} relationship outlined in Section 2.1.2). We observe that a higher effective mass for a charge carrier will result in a lower charge acceleration and therefore reduced charge transport. In addition, the scattering time τ will depend upon the local scattering processes within the material, and therefore be specific to each charge carrier type. Therefore we observe different mobilities for electrons and holes:

$$\mu_n = \frac{q\tau_n}{m_e^*} \quad \text{and} \quad \mu_p = \frac{q\tau_p}{m_h^*} \quad (2.19)$$

Next we consider the response of a charge carrier to a gradient in concentration. Fick's law describes the evolution of a population as a result of a microscopically random walk of particles, and shows that a gradient in particle concentration will result in a current proportional to the magnitude of the gradient. Therefore, in semiconductors:⁸⁴

$$\mathbf{j}_n = qD_n\nabla n \quad (2.20)$$

where D_n is the proportionality constant called the diffusion coefficient or diffusivity. Diffusion is related to random thermal motion as well as charge carrier scattering, therefore we aim to relate it to charge mobility. We consider the situation in which a gradient in electron concentration is established via non-uniform doping. In this case:⁸⁴

$$qn\mu_n\mathbf{E} = -qD_n\nabla n \quad (2.21)$$

taking ∇n to match the doping profile, the resulting electric field will be:

$$\mathbf{E} = -\frac{1}{n} \frac{k_B T}{q} \frac{dn}{dx} \quad (2.22)$$

substituting this field into equation 2.21, we obtain:

$$D_n = \frac{k_B T}{q} \mu_n \quad (2.23)$$

which is known as the Einstein relation and holds for electrons and holes in non-degenerate semiconductors.⁸⁴

Having introduced and related the drift and diffusion of charge carriers, we present the current-density equations:⁴¹

$$\mathbf{J}_n = q\mu_n n \mathbf{E} + qD_n \nabla n, \quad \mathbf{J}_p = q\mu_p p \mathbf{E} + qD_p \nabla p, \quad (2.24)$$

$$\text{and} \quad \mathbf{J}_{total} = \mathbf{J}_n + \mathbf{J}_p \quad (2.25)$$

where \mathbf{J}_n and \mathbf{J}_p are the electron and hole current densities, respectively. The current-density equation describes the behaviour of charge carriers under steady-state conditions. We will expand upon them to introduce time-dependent effects in discussing charge recombination in Section 2.3.

2.2.2 Charge carrier scattering

In the previous section we introduced the relaxation-time approximation, which aims to describe carrier scattering mechanisms via an average scattering (or relaxation) time for charge carriers. As such, charge scattering time τ is composed of multiple processes, potentially including charge scattering off e.g. impurities, grain boundaries, or other charge carriers. By assuming that each scattering mechanism is independent, the Matthiesen rule can be used to obtain the total scattering rate:⁸⁴

$$\frac{1}{\tau} = \sum_i \frac{1}{\tau_{phonon}} + \frac{1}{\tau_{impurities}} + \frac{1}{\tau_{grain\ boundaries}} + \dots \quad (2.26)$$

Here we briefly introduce several scattering mechanisms.

A scattered charge carrier will move into a new $E-\mathbf{k}$ state, and therefore the scattering rate with phonons is proportional to the density of final states available: $\tau \propto g(E)$, where $g(E)$ is the density of states. In the case of scattering from impurities, it is common to express the scattering rate as a power law, such as: $\tau(E) = \text{constant} \cdot E^s$, where s is a characteristic exponent.⁸⁶ For non-ionised impurity scattering of low energy carriers in parabolic bands, $s = -1/2$, following the parabolic curve of the density of states as expected in phonon scattering. The nature of the impurity has great effect, however, as in the case of ionised impurities $s = +3/2$. Thus, the contribution of impurity scattering is often written as $\tau = \tau_0(E/k_B T)^s$, where τ_0 is a constant and s varies from $-1/2$ to $+3/2$ depending on the strength of screening.⁸⁶ Taken together, general trends of scattering rates may be understood from rough knowledge of the density of states.

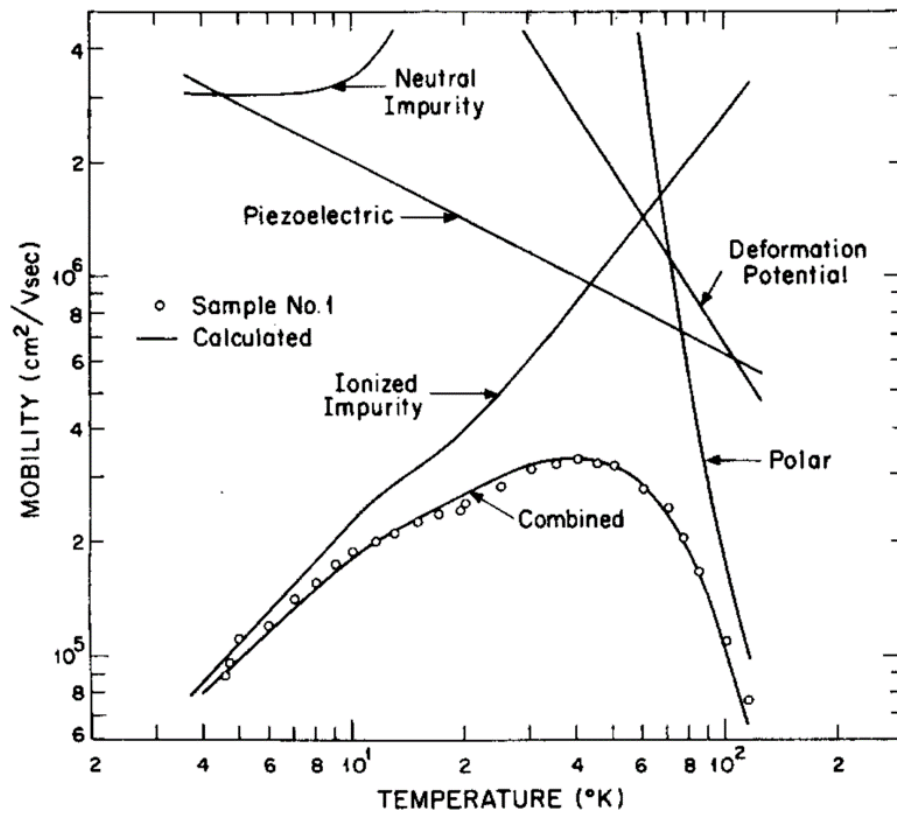


Figure 2.5 Mobility vs temperature of *n*-type GaAs ($N_D \sim 5 \times 10^{13} \text{ cm}^{-3}$, $N_A \sim 2 \times 10^{13} \text{ cm}^{-3}$). Solid lines are theoretical mobilities resulting from various scattering mechanisms and combined mobility. Figure reproduced with permission from Ref. [85].

Scattering from grain boundaries is an important effect in polycrystalline materials.⁴¹ The effect of grain boundaries can be relatively complicated, as they can scatter carriers as they encounter the change in lattice orientation⁸⁷ or act as traps for charge carriers.⁴¹ To give an example of the effect of charge trapping, we consider polycrystalline silicon as described in Ref. [41]. At low carrier densities, all free carriers are trapped at grain boundaries, reducing conductivity. Despite this, no barrier to transport exists. Intermediate charge density results in partially filled traps at grain boundaries, and the formation of an electronic barrier (ΔE_b) which must be overcome with thermal excitation of charge carriers to achieve transport. Finally, at high free carrier concentrations the traps are filled and the barrier vanishes.

As a result of the many contributions to charge scattering, it is very complex to accurately predict the charge transport parameters: mobility and diffusivity. Figure 2.5 shows the mobility versus temperature for high-quality *n*-type GaAs, as well as predicted contributions of various scattering mechanisms. As stated previously, the exact nature of the band structure in metal-halide perovskites remains under debate, therefore a range of transport parameters have been predicted. In the case of MAPbI₃, first principles calculations only considering acoustic phonon scattering predicted charge mobilities of several thousand cm² Vs⁻¹,^{36,88} while reports introducing Rashba splitting effects predict mobilities of several hundred cm² Vs⁻¹.⁸⁹ These values remain much higher than experimentally measured values which we will introduce further in the next section.

2.2.3 Carrier transport measurement techniques

In this thesis, we develop a means of probing directly charge transport dynamics in metal-halide perovskite materials. Therefore we present here a short introduction to several of the most common means of probing transport dynamics, and briefly discuss the benefits and limitations in each case. A summary comparing several measurement methods is provided in Table 2.1, and additionally a summary of reported transport parameters obtained from various techniques is presented in Table 4.1 at the end of Chapter 4.

Time-resolved terahertz (THz) absorption spectroscopy

THz spectroscopy employs a short pump pulse to generate excitations followed by a time-delayed probe pulse, in this case in the terahertz energy range (1-100 meV). The response

of the carrier population to the applied oscillating electric field is measured, which is directly proportional to the photoconductivity of the material. THz spectroscopy is an indirect measurement of charge transport parameters (D and μ), however, requiring assumptions of the underlying mechanism of charge transport.⁹⁰ That said, for bulk systems well-known Drude-like behaviour has been reported.⁹¹ Mobilities have been reported to be 8 - 35 cm² Vs⁻¹ in polycrystalline MAPbI₃ films,⁹²⁻⁹⁴ while the highest mobility in MAPbI₃ experimentally measured to-date exceeded 500 cm² Vs⁻¹ as reported by Valverde-Chávez et al. on MAPbI₃ single crystals.⁹⁵

Thus, THz spectroscopy is a common probe of transport parameters, and reveals that charge mobilities are highly dependent on the characteristics of the sample. In addition, the reported mobilities are heavily influenced by the model of charge transport which is applied. The reported values are often higher than those reported using other techniques. Finally, THz spectroscopy is not able to distinguish between types of charge carrier.

Time-resolved microwave conductivity

Time-resolved microwave conductivity (TRMC), like THz spectroscopy, probes the temporal response of photoconductivity after optical excitation. Microwave radiation is of even lower energy than in the case of THz, therefore the frequency of radiation is reduced and TRMC is sensitive to slower dynamics than THz spectroscopy. Nevertheless, reports of carrier mobility using TRMC have similar trends in reported values, ranging from 3 - 20 cm² Vs⁻¹ for MAPbI₃.^{93,96} Similar to THz spectroscopy, TRMC is an indirect measurement and requires an established theoretical model in order to extract material parameters.

Applied field techniques: TOF, FET and Hall effect

The two previously discussed pump-probe techniques, THz spectroscopy and TRMC, employ low energy radiation to study the transient alternating current conductivities of investigated materials. Several methods employ externally applied field to investigate the motion of charge carriers, including: time-of-flight (TOF),⁹⁷ field-effect transistor (FET),⁹⁸ space charge limited current (SCLC),⁹⁹ charge extraction by linearly increasing voltage (CELIV),¹⁰⁰ and Hall effect measurements.¹⁰¹ Here we will introduce the most common techniques: TOF, FET and Hall effect.

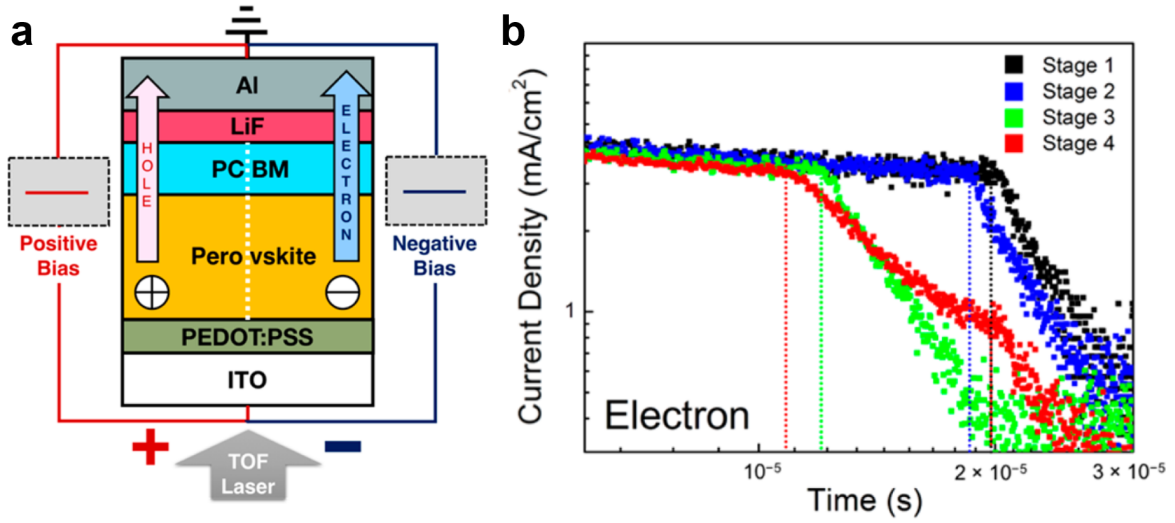


Figure 2.6 a) Schematic of a TOF measurement. Both electron and hole dynamics are accessible by varying the applied voltage. b) Current vs time under 2 V applied bias for electrons in a MAPbI₃ device. Dotted lines indicate t_{tr} . Figure reproduced with permission from Ref. [102].

Let us begin with a brief introduction to TOF measurements. The measurement requires a contacted device with selective electrodes, an example architecture is given in Figure 2.6a. A pulsed excitation is used to inject mobile charges, and the resulting photocurrent decay with time is measured under applied bias (Figure 2.6b). The mobility is given by:

$$\mu = \frac{d^2}{V \times t_{tr}} \quad (2.27)$$

where d is the known distance charges travel (e.g. film thickness, given by measurement geometry), V the applied bias, and t_{tr} the transient time. Thus, the TOF technique is a powerful means of directly probing hole and electron mobilities in a device architecture, and the shape of the photocurrent decay can be employed to investigate the nature of charge trapping in perovskite materials.⁹⁰ Mobilities found in TOF measurements vary greatly, with many reports showing much lower mobilities than in other measurements, having values of $\sim 1 \times 10^{-4} \text{ cm}^2 \text{ Vs}^{-1}$. Higher mobilities have been reported for architectures without charge selective electrodes, such as lateral measurements by Grill et al. which reported mobilities as high as $6 \text{ cm}^2 \text{ Vs}^{-1}$.¹⁵³

Another means of directly probing transport behaviour is via the preparation of field-effect transistors employing perovskite as the active layer. FETs employ a gate

voltage to induce a conductive region between two electrodes, probing lateral transport through films and is an effective measure of doping in a semiconducting material. FET measurements, similar to the case of many TOF measurements, tend to give very low carrier mobility, often on the order of $1 \times 10^{-4} \text{ cm}^2 \text{ Vs}^{-1}$.⁹⁰ Recently, a FET with $\mu = 0.5 \text{ cm}^2 \text{ Vs}^{-1}$ was reported,¹⁰³ and the authors suggested the low mobility may be the result of ionic screening.

Thus, it is possible the relatively low mobilities found via TOF and FET measurements are the result of high compensation ratios within perovskite materials, resulting from mobile charged defects and ions. Most importantly, this implies that applied field techniques underestimate the mobility of charge carriers at operating conditions for solar cells. In addition, the quantity of ionic defects is likely dependent on sample preparation, which may contribute to the large variation in mobilities reported.

The Hall effect is a well-established, steady-state technique to characterise the transport properties and doping concentration in semiconductors. The method involves the simultaneous application of electric and magnetic field, and therefore requires four electrodes, two to apply field and two for voltage detection as a result of the Lorentz force. Once more, results are heavily dependent on sample morphology, though obtained mobilities are higher than in other applied-field techniques, ranging from $0.5 - 8 \text{ cm}^2 \text{ Vs}^{-1}$ for polycrystalline films.^{90,104}

Transient absorption (TA) Spectroscopy

TA spectroscopy is a well-established technique used to investigate the photo-response of materials especially in the ultrafast regime. First, a short laser pulse (10 fs – 10 ps) generates excitations. Then a weak time-delayed pulse is used to probe the pump-induced changes in sample absorption. This method can probe charge dynamics over a broad range of timescales (10^{-13} – 10^{-4} s), but the wide variety of varying contributions makes interpretation of results challenging. As a result, it is common to investigate the lifetime of excited species using the method, but extracted transport properties differ greatly from those found in other measurements. For example, Richter et al. investigated the thermalisation of excited species on the picosecond timescale, and found very low scattering rates translating to mobilities as high as $500 \text{ cm}^2 \text{ Vs}^{-1}$ on these timescales.¹⁰⁵

Despite this, adaptations of the technique have been used to examine charge diffusion on longer timescales. High quality single crystals probed via transient reflection spectroscopy by Yang et al. were found to be well fitted by a 1D, surface recombination-

dominated model,¹⁰⁶ and they reported diffusivities of $D = 0.27 \text{ cm}^2 \text{ s}^{-1}$ for MAPbBr₃ single crystals. In addition, by using spatially resolved TA charge transport can be mapped allowing diffusivity to be more directly examined. Guo et al. reported a diffusivity of $\sim 0.05 \text{ cm}^2 \text{ s}^{-1}$ on a MAPbI₃ thin film.¹⁰⁷ Thus, TA can be a powerful probe of local or ultrafast charge transport, but TA is unable to discern between charge carriers and requires large excitation densities to achieve acceptable signal-to-noise ratios.⁹⁰

Photoluminescence-based techniques: scanning PL, TRPL, and PL Quenching

Photoluminescence (PL) spectroscopy is a powerful, common technique which involves exciting a sample optically and detecting the resulting luminescence. Standard PL, however, does not resolve charge dynamics or spatial information. One means of investigating charge transport is to spatially resolve photoluminescence measurements. As the intensity of emission is proportional to the number of excited states, the spread of PL from a point excitation gives information on charge transport parameters. TRPL involves exciting a sample with a pulsed light source and investigating the temporal evolution of the resulting photoluminescence.

Once more, as the photoluminescence is directly proportional to the population of emitting states, the dynamics of photogenerated charges is directly accessible. Therefore, combining spatial and temporal resolution of photoluminescence is a powerful means of probing very local behaviour of perovskite materials, such as the variation between grains¹⁰⁸ and the effect of grain boundaries.⁷² Tian et al. characterised charge diffusion within individual perovskite grains (and diffusion into neighbours). Using this technique, they reported diffusivities on MAPbI_{3-x}Cl_x ranging from 1.5 - 3.3 $\text{cm}^2 \text{ s}^{-1}$.¹⁰⁹

To extract diffusivities without spatial resolution, other techniques involving modelling based on assumed behaviour are performed. For example, Stranks et al. combined TRPL with PL quenching resulting from application of a charge extraction layer to extract charge carrier diffusivity.¹¹⁰ Otherwise, the nature of transport and recombination must be assumed to allow charge transport parameters to be modelled.

TRPL can access several temporal regimes, but of most interest to charge transport in devices is the regime often accomplished via time-correlated single photon counting: 100 ps - 10 μs . Reports coupling TRPL to modelled charge behaviour give diffusion lengths in the hundreds of nanometers and diffusivities of under $0.02 \text{ cm}^2 \text{ s}^{-1}$ in polycrystalline MAPbI₃.¹¹¹

The ease and relatively long timescales of measurement make TRPL very widely employed. However, the technique relies on predicting several complicated behaviours, including recombination, photon recycling,¹¹² and lateral charge diffusion.⁷² In addition, PL intensity is proportional to the population of both electrons and holes, which limits its ability to distinguish between electrons and holes.

Scanning current techniques

Scanning current techniques include scanning photocurrent measurements (SPCM), also known as optical-beam induced current (OBIC),¹¹³ and electron-beam induced current (EBIC). Scanning measurements are a well-established technique for characterising charge diffusion ranges, and are accomplished by monitoring the photocurrent of a electrically contacted material resulting from the excitation of charge carriers via an optical- or electron-beam. Figure 2.7a provides a schematic of such a measurement performed on a single crystal. As the excitation–collection distance can easily be varied, the range of charge diffusion can be directly investigated. The technique is commonly performed at zero applied bias, resulting in short-circuit conditions. We note that, similar to scanning photoluminescence techniques, the method is a powerful means of investigating the spatial variation in film behaviour. Indeed, scanning techniques have been used to investigate the spatial variation of device performance in many technologies, including silicon,¹¹⁴ GaAs,¹¹⁵ and perovskites.¹¹⁶ To examine charge transport, it is helpful to use a simplified system in which contacts are well-defined and the excitation is rastered in a controlled geometry. An example of the photocurrent decay resulting from rastering away from a charge collection electrode in a MAPbI₃ single crystal is presented in Figure 2.7b. The charge diffusion range in perovskite thin film devices has been reported to be $\sim 1 \mu\text{m}$ using the EBIC technique,¹¹⁷ while single crystal studies have reported diffusion ranges $> 10 \mu\text{m}$.⁸³

Here, we note that scanning current studies, up to now, have only directly probed the diffusion range of generated carriers. Cited reports have only employed the photocurrent amplitude to investigate the distance charges travel, but do not use scanning techniques to investigate the temporal response of current. In their work on single crystals, for example, Semonin et al. reported mobilities based upon TRMC measurements.⁸³

Scanning photocurrent measurements are typically accomplished using lock-in based detection, and therefore the photocurrent amplitude and phase are both accessible from the measurement. In this way, the temporal response of the investigated system can be accessed, providing a direct measurement of charge carrier transport parameters. This

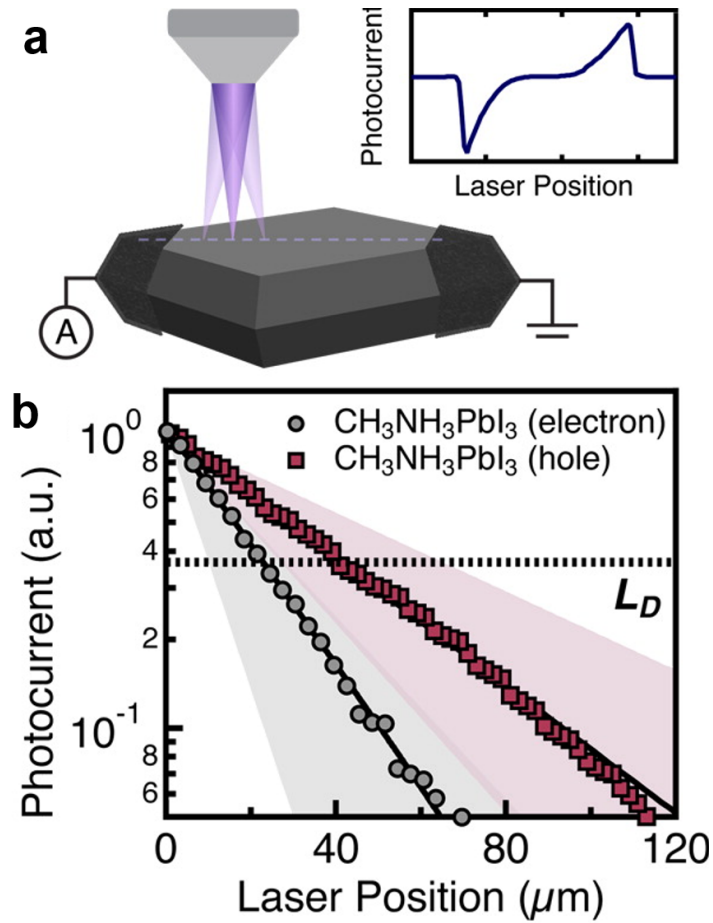


Figure 2.7 a) Schematic of the scanning photocurrent technique as applied to single crystals. b) Photocurrent vs distance for two types of MAPbI₃ single crystal, the dotted line indicates the distance at which photocurrent drops to $1/e$. Figure reproduced with permission from Ref. [83].

Table 2.1 Comparison of transport measurement techniques.

Method	Charge density (cm^{-3})	Temporal window (s)	Sample	Limitations
THz	$> 10^{18}$	$10^{-12} - 10^{-9}$	film	cannot distinguish carriers
TRMC	$> 10^{18}$	$10^{-10} - 10^{-4}$	film	cannot distinguish carriers
TA	$> 10^{18}$	$10^{-13} - 10^{-8}$	film	cannot distinguish carriers, challenging to interpret
TOF	$> 10^{14}$	$10^{-9} - 10^{-6}$	device	requires applied field and thick films
FET	–	–	device	requires applied field
Hall	$> 10^{16}$	$10^{-6} - 10^{-4}$	device	requires high electrical conductivity
TRPL/PLQ	$> 10^{15}$	$10^{-12} - 10^{-4}$	film or device	cannot distinguish carriers, many assumptions needed
SPCM	$> 10^{16}$	$10^{-6} - 10^{-4}$	device	carriers only distinguished in certain geometries

technique then provides a powerful means of directly accessing transport with several advantages: no influence of screening effects, measurement over device-relevant time scales, measurement over device-relevant length scales, and no assumptions needed to interpret results.

2.3 Recombination in crystalline semiconductors

We have introduced the concept of exciting free carriers in semiconductors, and discussed how these excitations move. Specifically, we have looked at electron promotion to, and motion within, the conduction band. The process of electron relaxation to the valence band, thereby removing an excited species, is termed recombination of electrons and holes. Thus, the process of interband relaxation governs the return of a semiconductor to equilibrium after light absorption. In addition, it should be noted that the relaxation of an excitation within a semiconductor represents a loss in an energy-harvesting device such as a solar cell. Here we will introduce the most important characteristics of charge recombination in metal-halide perovskites, and introduce the time-dependent continuity equations for charge transport and recombination.

2.3.1 Band-band recombination

Band-band recombination is the relaxation of an electron in the conduction band directly to the valence band, annihilating a hole and releasing a photon. In a direct semiconductor this process requires no change in momentum, and therefore is a two particle process. This process is then governed by the same mathematics as absorption, introduced in Section 2.1.3, where the probability of transition is related to the number of available states. Therefore, the probability of emission will depend on the number of transitions available, i.e. the number of excited electron-hole pairs in the system. The number of electrons and holes is normalised to electron and hole densities n and p . The rate of recombination is therefore bimolecular ($R_{bi.}$), and is written as:

$$R_{bi.} = b(np - n_i p_i) \quad (2.28)$$

where n_i (p_i) is the intrinsic electron (hole) density. Here, b is the bimolecular recombination constant and is determined by the band structure, carrier temperature, and carrier-carrier screening. The inclusion of intrinsic carrier densities accounts for spontaneous excitation of charge carriers at thermodynamic equilibrium.

Under illuminated conditions excess electron and hole populations ($\Delta n, \Delta p$) are generated, resulting in a recombination rate of:

$$R_{bi.} = b[(\Delta n + n_i)(\Delta p + p_i) - n_i p_i] \quad (2.29)$$

$$= b(\Delta n \Delta p + \Delta n p_i + \Delta p n_i) \quad (2.30)$$

Each absorption event will generate one electron and one hole. Taking $\Delta n = \Delta p = n$, and assuming the excited carrier population is much larger than the intrinsic carrier population, we simplify the bimolecular recombination rate to:

$$R_{bi.} \approx bn^2 \quad (2.31)$$

Note that the rate of recombination scales quadratically with carrier population.

Direct band-band transitions are the inverse of optical absorption of charge carriers, and therefore generate photons. The van Roosbroeck-Shockley relation relates generation of carriers via black-body radiation to the recombination rate. At thermal equilibrium, using the Boltzmann approximation for the distribution of light we relate

emission and absorption as:¹¹⁸

$$bn_i^2 = \int_0^\infty \frac{8\pi n_s^2}{c^2} \frac{\omega^2 \alpha(\omega) d\omega}{\exp(\hbar\omega/k_B T) - 1} \quad (2.32)$$

where α is the absorption coefficient, n_s the refractive index, and ω is the frequency of light.

As absorption of light and emission of light are linked, radiative recombination is viewed as unavoidable. It is primarily dependent on the fundamental properties of the material used, not on impurities or fabrication methods, and therefore high absorption necessarily translates into a high radiative coefficient.¹¹⁹

2.3.2 Shockley-Read-Hall recombination

In an ideal semiconductor, recombination would only occur via band-band recombination. Real semiconductor materials, however, contain defect sites which can localise carriers. These defects form energetic levels within the semiconductor bandgap, often called trap states, which allow trapped carriers to recombine with opposite charged carriers within the band. This form of recombination, proposed roughly simultaneously by Shockley and Read¹²⁰ and Hall,¹²¹ is called Shockley-Read-Hall (SRH) recombination. In general, the net rate of recombination is:

$$R_{SRH} = \frac{np - n_i^2}{\tau_n(n + n_t) + \tau_p(p + p_t)} \quad (2.33)$$

where n_t (p_t) is the population of electrons (holes) in filled traps and τ_n (τ_p) is the time for electrons (holes) to be captured by traps. The capture time of charge carriers depends on the number of trap states (N_t), the capture cross-section ($\sigma_{n,p}$) and the velocity of carriers (v_{th}), as:

$$\tau_{l,n} = (\sigma_n v_{th} N_t)^{-1} \quad \tau_{l,p} = (\sigma_p v_{th} N_t)^{-1} \quad (2.34)$$

Thus, we note that while the number of trapped species is in the denominator of Equation 2.33, the capture time $\tau_{n,p}$ decreases with increasing trap density. Therefore increasing the density of traps increases the rate of SRH recombination. As the number of traps is dependent on the quality of semiconductor material, it is considered an avoidable form of recombination in semiconductor devices.

SRH recombination is commonly referred to as monomolecular recombination, though Equation 2.33 is not strictly monomolecular. Let us consider two conditions in which SRH will simplify to the monomolecular case. First, we consider the situation in which a semiconductor is heavily doped such that one carrier is dominant. Taking holes to be the dominant carrier, we then take $p \gg n \geq n_i$. Assuming charge trapping times are similar ($\tau_n \sim \tau_p$), we can approximate Equation 2.33 to $R_{SRH} = n/\tau_n$. Here we observe that τ_n describes the monomolecular charge lifetime, τ_l . This situation is common in traditional semiconductors where charge densities are often dominated by doping.

Second, consider the case when excited free carriers are large in number, much larger than intrinsic carrier and trap densities. In this case, $\Delta n = \Delta p \gg n_i, p_t, n_t$, and we see that $R_{SRH} \approx n/(\tau_n + \tau_p)$. Here we observe that the monomolecular lifetime τ_l depends on the trapping time of both electrons and holes. Metal-halide perovskite materials have a low density of intrinsic carriers ($\sim 10^4 \text{ cm}^{-3}$),¹²² and the low Urbach energy of perovskites (Section 2.1.3) indicates a low density of trap states.

2.3.3 Surfaces and grain boundaries

Surfaces and grain boundaries in semiconductors represent regions where there is likely to be a large concentration of defect states, due to broken bonds and high concentration of impurities. As a result of these concentrations localising to a surface, it is often useful to consider density per unit area.¹¹⁹ Thus, we can define surface recombination velocities ($S_{n,p}$) by multiplying the density of traps per unit area (N'_{st}), with the capture cross-section ($\sigma_{n,p}$): $S_{n,p} = (\sigma_n v_{th} N'_{st})$. Trapping time $\tau_{n,p}$ is the product of the thickness of the layer of traps (Δx), and $S_{n,p}$. Thus, surface recombination per unit area is:

$$R_{surf} \Delta x = \frac{np - n_i^2}{(n + n_t)/S_n + (p + p_t)/S_p} \quad (2.35)$$

If we consider the case of one carrier being dominant, $n \gg p$, then we may simplify surface recombination to $R_{surf} \Delta x = S_p(p - p_i)$.

2.3.4 The continuity equation, diffusion length, and recombination in perovskites

We now consider the change in charge carrier populations with time. We consider the density of electrons (n) in a specific region of semiconductor. The net change in electron concentration will then be the difference between the rate of charge carrier generation (G_n) and recombination (R_n), plus the net current of charges flowing in and out of the system. Thus, we write:

$$\frac{\partial n}{\partial t} = G_n - R_n + \frac{1}{q} \nabla \cdot \mathbf{J}_n \quad (2.36)$$

Here we introduce the current-density equations (Equation 2.24) and previously considered recombination pathways:

$$\frac{\partial n}{\partial t} = G_n - R_{SRH} - R_{Surf} - R_{bi} + n\mu\nabla\mathbf{E} + \mu\mathbf{E}\nabla n + D_n\nabla^2 n \quad (2.37)$$

Letting \mathbf{E} and $\nabla\mathbf{E}$ be zero, and combining the monomolecular approximations of Equations 2.33 and 2.35 into a single term (a), we write:

$$\frac{\partial n}{\partial t} = G_n - an - bn^2 + D_n\nabla^2 n \quad (2.38)$$

Yielding an equation describing the evolution of the electron population in the absence of field when $\Delta n = \Delta p \approx n \gg n_i$. When monomolecular recombination is dominant, the total lifetime of charge carriers is $\tau_l \sim 1/a$. An identical expression can be written for holes.

It is clear that the recombination coefficients, a and b , relate to charge transport as they determine the timescale over which charge movement is possible. In Section 2.2 we discussed charge diffusivity ($D_{n,p}$) in relation to mobility and charge scattering. We now formally introduce the diffusion length, L_D , which relates the dynamics of charge transport to the charge lifetime, and is related to root mean square displacement of carriers before charge recombination (or extraction). The mean square displacement in one dimension is $\langle x^2 \rangle = 2D\tau_l$, and the diffusion length will therefore vary depending upon the geometry investigated. To simplify interpretation, it is common to report $L_D = \sqrt{D\tau_l}$ as the diffusion range of charge carriers.

The diffusion range of charge carriers in metal-halide perovskites is remarkably long, especially considering the solution-based polycrystalline nature of prepared films and

devices. The bimolecular recombination coefficient of metal-halide perovskites is on a similar order of magnitude as that of GaAs. Richter et al. characterised b in MAPbI₃ to be $8.1 \times 10^{-11} \text{ cm}^3 \text{ s}^{-1}$,¹²³ which is similar to other reported values⁹² and will be used in this thesis. As mentioned in previous sections, the bimolecular recombination coefficient (b) is largely intrinsic to a material. Therefore, efforts to extend charge diffusion range often focus on reducing the monomolecular, trap-assisted recombination coefficient (a). Extended diffusion ranges were attained in classic semiconductor materials via careful control of fabrication techniques. Expensive, slow methods of single-crystal silicon growth and surface treatments produce material with minority carrier diffusion ranges exceeding 1 mm.¹²⁴ Many efforts have been made to reduce recombination in perovskite devices, via passivation of perovskite interfaces,¹²⁵⁻¹²⁷ light and atmospheric treatments,⁶⁶ as well as optimisation of metal-halide perovskite composition.^{62,128} Due to the variety of sample morphologies, as well as variation in passivation techniques, a wide range of charge carrier lifetimes have been reported. Lifetimes of polycrystalline MAPbI₃ in literature stretch from the hundreds of nanoseconds¹²³ to a recent report reporting a lifetime $>30 \mu\text{s}$ due to passivation treatments.⁶⁶

2.4 Junctions in semiconductor devices

Junctions of semiconductor materials form the basis of many electronic devices. This includes solar cells, where excited charges must reach, and cross into, extraction electrodes. In this thesis the influence of extraction layers on carrier behaviour in metal-halide perovskite materials is discussed, and therefore we outline the fundamental properties of p - n homo- and hetero-junctions. Finally, we discuss the nature of electrode-perovskite junctions. The theory in this section is based on Ref. [84].

2.4.1 The p - n homojunction

When the doping concentration within a semiconducting material changes abruptly from acceptor impurity N_A to donor impurity N_D , a p - n junction is formed (Figure 2.8a). At thermal equilibrium the current flowing across the junction must be zero. We consider the current-density equation in one dimension for electrons (Eq. 2.24), and use the Einstein relation to translate D to μ , giving:

$$0 = \mathbf{J}_n = q\mu_n n \mathbf{E} + qD_n \nabla n = q\mu_n \left(n \mathbf{E} + \frac{kT}{q} \frac{dn}{dx} \right) = \mu_n n \frac{dE_F}{dx} \quad (2.39)$$

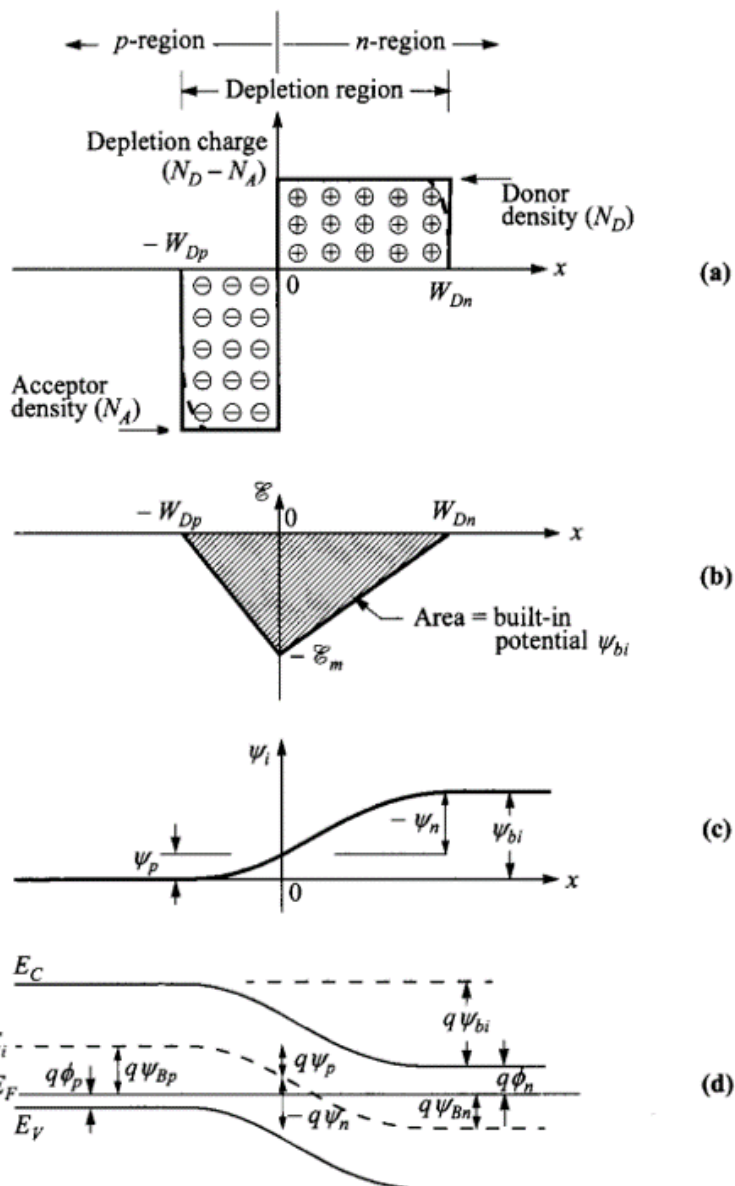


Figure 2.8 Abrupt p - n junction at equilibrium, showing the (a) space-charge, (b) electric field, (c) potential and (d) energy bands with distance. The built-in field is ψ_{bi} . Figure reproduced with permission from Ref. [84].

where E_F is the Fermi energy level of the semiconductor. Clearly, the condition of zero electron or hole current requires that dE_F/dx must be zero. Therefore the Fermi level must be constant throughout the material.⁸⁴ As a result, a built-in potential Ψ_{bi} will develop as shown in Figures 2.8b,c, and d. The built-in potential is related to the bandgap and the conduction and valence band energies by:

$$q\Psi_{bi} = E_g - (E_{c,n} + E_{v,p}) = E_g - (q\phi_n + q\phi_p) \quad (2.40)$$

where $E_{c,n}$ and $E_{v,p}$ are the energy levels of the n -type conduction band and p -type valence band, respectively. The built-in field is then related to the concentration of carriers in the two regions away from the junction as:

$$q\Psi_{bi} = \frac{k_B T}{q} \ln\left(\frac{n_{n0}}{n_i}\right) + \frac{k_B T}{q} \ln\left(\frac{p_{p0}}{p_i}\right) \approx \frac{k_B T}{q} \ln\left(\frac{n_{n0}}{n_{p0}}\right) = \frac{k_B T}{q} \ln\left(\frac{p_{p0}}{p_{n0}}\right) \quad (2.41)$$

where n_{n0} (p_{p0}) and n_{p0} (p_{n0}) are the electron (hole) concentrations in the n -type and p -type regions, respectively.

As a result, a built-in field will also be formed across the junction. We apply the depletion approximation, in which it is assumed that the potential across the junction depletes the junction region of all charge carriers forming a box profile (Figure 2.8a). Due to depletion of mobile electrons and holes within the field, a charged region will form, and the total charge on each side of the junction will cancel such that $N_A W_{D,p} = N_D W_{D,n}$, where $W_{D,n}$ ($W_{D,p}$) is the width of the charge depletion region in the n -type (p -type) material. The Poisson equation becomes:⁸⁴

$$-\frac{d^2\Psi}{dx^2} = \frac{dE}{dx} = \frac{\rho(x)}{\epsilon} = \frac{q}{\epsilon} [N_D - n(x) - N_A + p(x)] \quad (2.42)$$

where ϵ is the dielectric constant. Assuming $n(x) = p(x) \approx 0$, we integrate and obtain the field as a function of distance, x :

$$E(x) = -\frac{qN_A(x + W_{D,p})}{\epsilon} \quad \text{for} \quad -W_{D,p} \leq x \leq 0, \quad (2.43)$$

$$= -\frac{qN_D}{\epsilon}(W_{D,n} - x) \quad \text{for} \quad 0 \leq x \leq W_{D,n} \quad (2.44)$$

The current-voltage characteristics of p - n junctions are determined by the distance charges injected from either side of the depletion region can travel before recombination.

Therefore we define a saturation current, J_0 :

$$J_0 = \frac{qD_p p_{n0}}{L_{D,p}} + \frac{qD_n n_{p0}}{L_{D,n}} \quad (2.45)$$

which is the current an ideal p - n junction will reach at negative bias as:

$$J(V) = J_0 \left[\exp\left(\frac{qV}{k_B T} - 1\right) \right] \quad (2.46)$$

which is known as the Shockely equation.¹²⁹

2.4.2 Junctions in metal-halide perovskite devices: semiconductor heterojunctions

While the p - n junction is of both fundamental and practical importance to many semiconductor material systems, to date no reproducible controlled means of doping metal-halide perovskite materials has been demonstrated.⁴⁸ This has prevented the fabrication of a classic p - n homojunction from the material. Instead, devices rely on the junction of perovskites with dissimilar semiconducting materials, such as inorganic materials including SnO_x , TiO_2 , and NiO_x ; or organic compounds including 2,2',7,7'-tetrakis(N , N -di- p -methoxyphenyl-amine)9,9'-spirobifluorene (Spiro-OMeTAD), [6,6]-phenyl- C_{60} -butyric acid methyl ester (PCBM), or poly(3,4-ethylenedioxythiophene)-poly(styrenesulfonate) (PEDOT:PSS). These materials are used as selective electrodes: they extract only one charge carrier type. To accomplish this, electrode materials are chosen with high bandgaps relative to perovskite materials, and are chosen to have conduction (valence) band energies near the conduction (valence) band energy of the metal-halide perovskite to achieve electron (hole) extraction. Thus, the opposite charge carrier is energetically prevented from transferring to the wrong electrode. This is visible in Figure 2.9, where we observe that the valence band in the proposed electron extraction materials (solid colour lines) is far below the energy of the valence band in perovskites (solid purple line), preventing hole transfer.

Also visible in Figure 2.9 is the presence of band bending, similar to that in p - n junctions (Figure 2.8). Band bending is the result of built-in potential at the interface (see Section 2.4.1), though in the case of heterojunctions the dissimilarity in material properties adds complication to the equations presented in Section 2.4.1. Namely, the difference in band structure moving across the junction adds terms to the expression

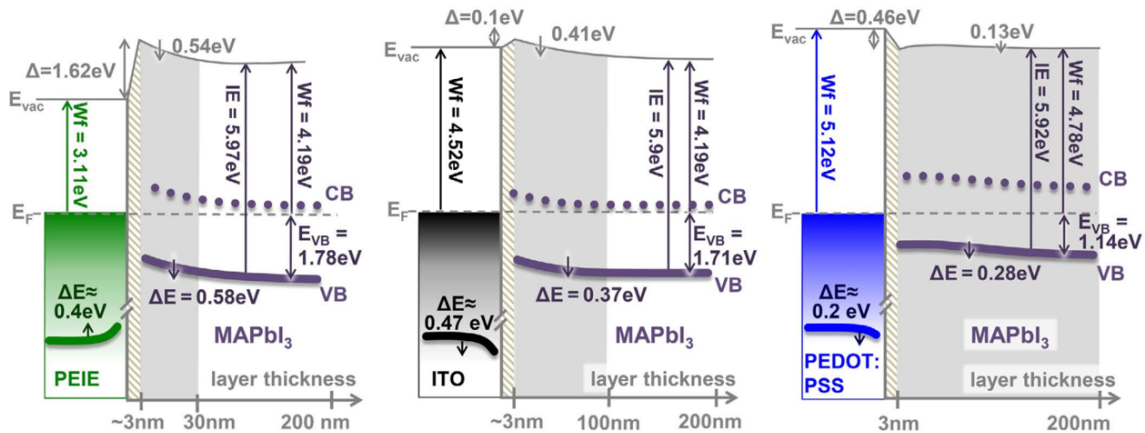


Figure 2.9 Schematics of heterojunctions in metal-halide perovskite materials, left-to-right: PEIE–MAPbI₃, ITO–MAPbI₃, and PEDOT:PSS–MAPbI₃. Each schematic divides the perovskite layer into three regions: (i) a shaded interface region, (ii) a grey region of band bending, and (iii) the equilibrium region, shaded in white. It can be observed that the conduction bands of PEIE and ITO align well with that of MAPbI₃, suggesting that they would make good electron extraction layers. Note that the band bending predicted from UPS and XPS measurements would create a barrier to electron extraction at the interface, however. (Figure reproduced with permission from Ref. [130].)

for built-in field, and the differences in dielectric constant need to be accounted for when calculating electric field.

2.5 Principles of photovoltaic device operation

Solar cells use the photovoltaic effect to harvest energy via the absorption of light. The photovoltaic effect was first reported in 1839 by Edmund Becquerel, while the first device to use the effect to harvest light energy was developed in 1876.¹¹⁹ The development of photovoltaic devices based on silicon, begun in 1954 using a silicon *p-n* junction,¹³¹ has delivered solar cell devices which are currently seeing expanding deployment for large-scale energy production. Subsequent development has led to several other promising technologies, including devices based on GaAs, CdTe, and organic materials. In this section we will introduce the *p-n* junction solar cell and discuss efficiency limits of photovoltaic devices. The theory in this section is based on References [84, 119].

2.5.1 Working mechanism

The photovoltaic effect is the generation of voltage upon the absorption of light. Absorption of photons with energy above the bandgap of a semiconductor creates an excited state which can travel (Section 2.2) and will eventually decay via recombination (Section 2.3). The photovoltaic effect in a p - n junction arises when charges are generated and diffuse towards the junction. Such free charges will be subjected to the field present at the junction, and be accelerated to either end of the junction. To harvest the energy captured in the absorption process, the excited carriers must be collected. To accomplish this, electrodes are used for charge collection and application of external bias.

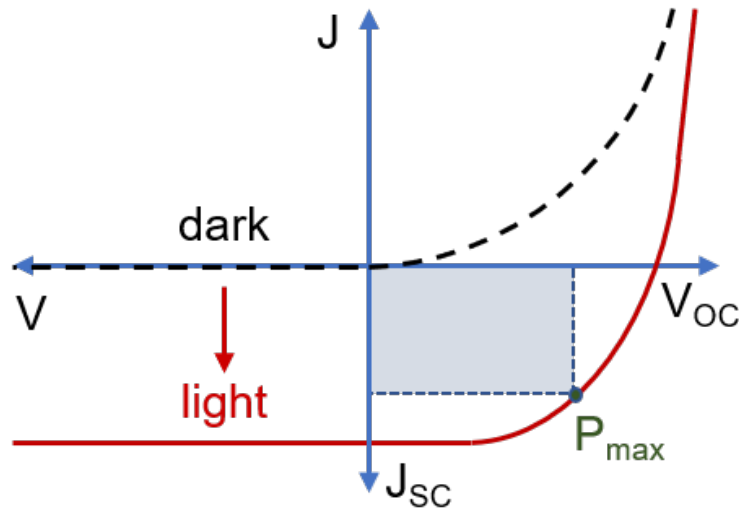


Figure 2.10 Current-voltage characteristics of a solar cell: the operation of a p - n junction in the dark (black dashed curve); and the short-circuit current (J_{SC}), open-circuit voltage (V_{OC}), and maximum power point (P_{max}) are indicated for the device under illumination (red curve).

To understand the current-voltage behaviour of the device, we recall the Shockley equation for p - n junctions (Equation 2.46). We recognise that photogenerated carriers will travel in the reverse direction of the saturation current, and therefore flip the sign of positive current and add a term for photogenerated current density, J_{SC} :

$$J(V) = J_{SC} - J_0 \left[\exp\left(\frac{qV}{k_B T}\right) - 1 \right] \quad (2.47)$$

We observe that if no external voltage is applied, a maximum current density equal to J_{SC} is obtained. These are short-circuit conditions, and therefore the current is

termed the short-circuit current ($I_{SC} = J_{SC} \times area$), as shown in Figure 2.10. Ideally, the current density at short-circuit would be equal to the number of photons absorbed per second, per area.

Setting $J = 0$, we calculate the voltage at which no current is extracted:

$$V_{OC} = \frac{k_B T}{q} \ln\left(\frac{J_{SC}}{J_0} + 1\right) \quad (2.48)$$

which is the expression for open-circuit voltage, V_{OC} . The power output is $P = I \times V$, and therefore there will be a point of maximum power where this product is maximised, (P_{max}). Considering Figure 2.10, we observe that this maximum power point is somewhere closer to the origin than the product of V_{OC} and J_{SC} . It is useful to observe how close to ideal ‘rectangular’ current-voltage behaviour a device is, however, and therefore the fill factor (FF) is defined relative to the maximum current and voltage attainable in the fourth quadrant:

$$FF = \frac{P_{max}}{V_{OC} I_{SC}} \quad (2.49)$$

Finally, the efficiency of a device will be the power harvested by the solar cell divided by the power incident upon it, and we define efficiency as:

$$\eta = \frac{FF \times I_{SC} \times V_{OC}}{P_{sunlight}} \quad (2.50)$$

2.5.2 Theoretical and practical efficiency limits

Shockley-Queisser limit

In 1961 Shockley and Queisser derived a theoretical efficiency limit of a solar cell based on a single $p-n$ junction.¹³² Their model made several assumptions: i) the sun and the $p-n$ junction are perfect black body radiators at 6000 K and 300 K, respectively. ii) Photons of energy below the bandgap ($\hbar\omega < E_g$) cannot be absorbed by the material. iii) Excitations generated by photons with excess energy ($\hbar\omega > E_g$) lose excess energy before extraction; that is, excitations cool to the band edge. iv) All recombination is purely band-band recombination and radiative.

Using these assumptions Shockley and Queisser calculated the variation of maximum efficiency with semiconductor bandgap, finding a peak of 33% for bandgaps of 1.1 –

1.3 eV. MAPbI₃ has a bandgap of 1.6 eV, slightly outside of the peak region but retaining a theoretical limit of 31% efficiency.

Nonradiative recombination

As mentioned in Section 2.3, real semiconductors possess nonradiative recombination pathways. Clearly, high rates of recombination will reduce the number of charges which reach electrodes for extraction. More surprisingly, it was demonstrated in 1967 by Ross that nonradiative recombination reduces the open-circuit voltage.¹³³ In particular, near V_{OC} the rate of charge extraction reduces, meaning charge carriers have more time to recombine and therefore the impact of nonradiative recombination on V_{OC} can be higher than on J_{SC} .^{134,135}

Under open-circuit conditions, charge extraction is zero. Thus, all charges must recombine, Ross related the V_{OC} to external photoluminescence quantum efficiency (η_{PL}) as:

$$V_{OC} = V_{ideal} - \frac{k_B T}{q} |\ln(\eta_{PL})| \quad (2.51)$$

where V_{ideal} is the maximum potential attainable by the system, which is primarily determined by the energetic structure of the constituent materials (i.e. bandgap), but also depends on the intensity of incident illumination.¹³³

Thus, as mentioned in Section 2.3, reduction of nonradiative recombination is of great interest to improve device efficiency.

Charge transport

Given that nonradiative recombination is detrimental to device performance, it is desirable to maximise the collection of charge carriers at operating conditions ($V < V_{OC}$). Therefore, the distance over which charge carriers are capable of moving determines the geometries of photovoltaic devices. As introduced in Section 2.2, charge diffusivity (D) and mobility (μ) give the kinetics of charge motion in semiconductor materials. The diffusion length (L_D), which combines transport and recombination information, therefore gives a direct order of magnitude of device dimensions. For example, silicon has diffusion ranges exceeding 100 μm for both charge types, leading to devices with thicknesses of several hundred μm .¹³⁶ The diffusion range in perovskite materials is on the order of several to tens of μm , therefore any charges generated in a device of 100 μm thickness would recombine before reaching a collection electrode.

For this reason, metal-halide perovskite vertical “sandwich” devices are generally $<1 \mu\text{m}$ in thickness.

Metal-halide perovskite devices: the “sandwich” architecture

The highest-performing metal-halide perovskite solar cells are composed of a double heterojunction structure. The most typical, and highest-performing design is a vertical “sandwich” architecture (Figure 2.11a).^{5,62,128} Regardless of precise design, double heterojunction solar cells employ two wide bandgap materials as collection electrodes with the metal-halide perovskite acting as the active layer: absorbing, separating, and transporting excitations to the electrodes. A schematic of a typical energetic alignment of the double heterojunction system is presented in Figure 2.11b. In contrast, back-contact architectures are the highest-performing silicon architectures, with Yoshikawa et al. reporting the highest-ever single-junction device efficiency this past year with 26.3% efficiency.⁶ Back-contact devices are those in which both charge-collection electrodes are buried, therefore all charge collection is accomplished on the bottom, unilluminated side of the device. Three groups have reported on metal-halide perovskite devices with back-contact architecture.^{112,137,138} We will discuss the scope for back-contact perovskite devices further in Chapters 4 and 6.

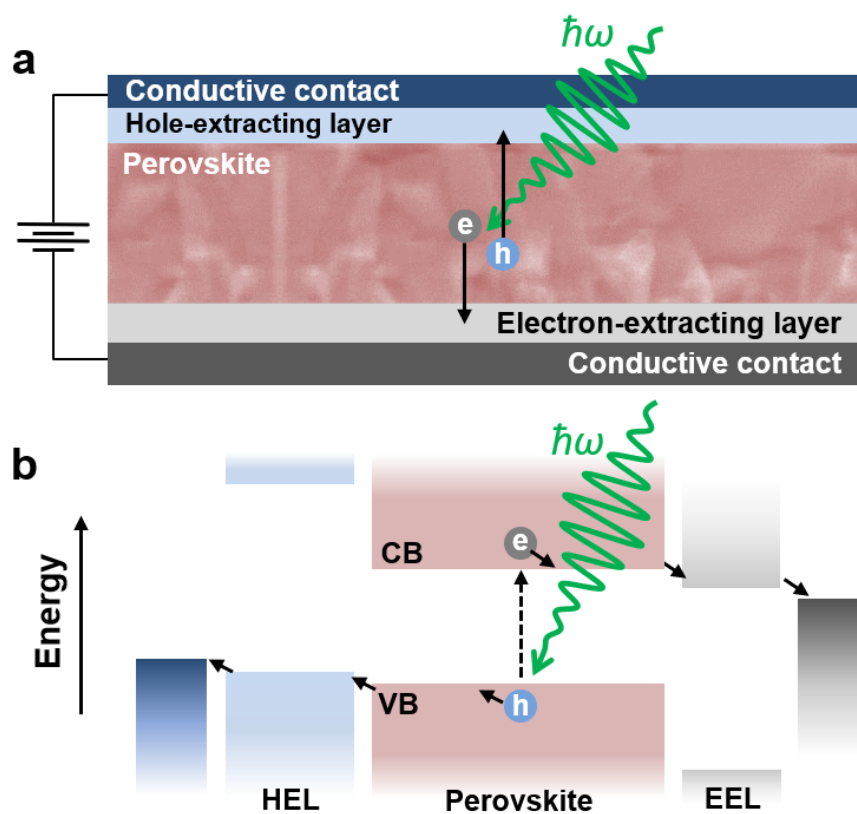


Figure 2.11 Schematic of typical metal-halide perovskite solar cell. The excitation of an electron-hole pair by a photon with $\hbar\omega > E_g$ is depicted. a) Typical vertical “sandwich” architecture, where the active perovskite material is enclosed by charge-selective extraction layers on the top and bottom surfaces. The direction of charge transport required to contribute to photocurrent is depicted by arrows. b) Schematic of a typical energetic alignment of the perovskite double heterojunction solar cell. The energetic transitions of charge carriers which contribute to photocurrent are indicated by arrows. Note that the influence of band bending is not presented here, as it is highly dependent on the specific material system.

Chapter 3

Experimental methods

3.1 Sample fabrication

Samples measured in this thesis were prepared by four parties: back-contact devices in photocurrent measurements presented in Chapters 4 and 5 were prepared by collaborators Maximilian Hörantner and Suhas Mahesh at the University of Oxford, uncontacted and contacted MAPbI₃ films measured in Chapter 6 were prepared in Cambridge by Haralds Āboliņš, MAPbI_{3-x}Cl_x films measured in Chapter 7 were prepared at the University of Bayreuth by Cheng Li, and finally vertical devices measured in the beginning of Chapter 5 were prepared in Cambridge by Mojtaba Abdi-Jalebi.

3.1.1 Back-contact device preparation

All quasi-interdigitated back-contact (QIBC) devices presented here were prepared by Maximilian Hörantner and Suhas Mahesh.

Substrate preparation

The glass substrates were been purchased from Pilkington Inc. with a coated fluorinated tin oxide (FTO) layer of 7 or 15 Ω /sq. FTO was partially removed from the substrate via etching with zinc powder and 2 M HCl to create non-conductive stripes for later needed counter-electrode fabrication. The etched substrates were rinsed in deionized (DI) water and cleaned rigorously by brushing Hellmanex solution with a toothbrush before rinsing again in a stream of DI water. N₂ was used to dry the substrates that were then subsequently rinsed in acetone and 2-propanol and then etched for 10 min in O₂ plasma.

Spin-coated SnO_x *n*-type layer

The SnO_x layer was prepared by following the method described by Anaraki et al.¹³⁹ 0.05 M SnCl₄ · 5H₂O was dissolved over 30 s of stirring in 2-propanol and then spin-coated in volumes of 200 μl onto the cleaned and etched glass/FTO substrates with 3000 rpm for 30 seconds at 200 rpm s⁻¹ acceleration. The substrates were then dried for 10 min at 100 °C and 60 min at 180 °C. Meanwhile, a chemical bath was prepared by mixing 40 ml DI water with 500 mg of urea, 500 μl of HCl (37%), 10 μl of 3-mercaptopropionic acid and 108 mg of SnCl₂ · 2H₂O (for a final concentration of 0.012 M). The cooled substrates were then immersed fully into the chemical bath and a lid was placed onto the beaker to prevent evaporation. The bath was kept at 70 °C within an oven for 180 min and afterwards the samples were sonicated for 2 min in DI water. The substrates were dried under a stream of dry air and then put onto a hotplate at 180 °C for 60 min.

Photoresist patterning

The image reversal photoresist AZ 5214 E was spin-coated at 5000 rpm for 45 seconds and baked for 50 seconds at 110 °C according to the datasheet provided by the manufacturer. UV-light exposure was accomplished with a wavelength of 265 nm and 250 mJ through a chrome patterned glass photomask. Subsequent image reversal was achieved by baking for 120 seconds at 120 °C leading to the solubility of the regions designed for the fingers of the rear contacts. These were dissolved through immersion in a developer bath of AZ 726 MIF for roughly 40 seconds, resulting in a patterned photoresist layer.

Al₂O₃ + Ni + NiO_x shell hole-conducting electrode

In the case of back-contact devices, the patterned photoresist layer was coated with 100 nm of insulating Al₂O₃ and 100 nm of nickel through e-beam evaporation. The lift-off of the remaining photoresist regions was performed in an 80 °C heated bath of dimethylsulfoxide (DMSO). In the case of films, 100 nm of nickel was evaporated directly onto glass substrates. In each case the Ni was subsequently annealed at 300 °C for 20 minutes to create a shell of oxidized Ni as a *p*-type electron blocking layer.

Perovskite layer deposition for QIBC devices

For back-contacted solar cells, the 3:0.98:0.02 molar ratio of $\text{CH}_3\text{NH}_3\text{I}:\text{PbCl}_2:\text{PbI}_2$ was well dissolved in DMF with a concentration of 38.5 wt% and spin-coated onto the substrates with patterned electrodes at 2000 rpm for 45 seconds in a dry air atmosphere. The drying of the deposited solution was performed under a weak air flow for 30 seconds before letting the substrates rest for 15 min at room temperature. Subsequently, an additional drying step of 15 min at 70 °C on a hotplate was performed, before the films were annealed in an oven for 90 min at 100 °C and 15 min at 120 °C. After the perovskite annealing procedure and the cooling of the substrates to room temperature, a layer of poly(methyl methacrylate) (PMMA) was deposited by spin coating a solution of 15 mg PMMA, dissolved in 1 ml of chlorobenzene, at 2000 rpm for 45 seconds. Resulting perovskite films have a characteristic grain size of roughly 500 nm.

3.1.2 Perovskite layer deposition for contacted films

Perovskite films investigated in Chapter 6 were prepared on three types of substrates: glass, NiO_x -Ni-glass, and SnO_x -FTO-glass. In the case of films deposited on electrode materials, the electrodes were prepared as described above for QIBC devices, save for nickel being evaporated directly onto glass as opposed to on Al_2O_3 . The perovskite film was accomplished first by dissolving a 3.05:1 molar ratio of $\text{CH}_3\text{NH}_3\text{I}$ to $\text{Pb}(\text{CH}_3\text{CO}_2)_2 \cdot 3 \text{H}_2\text{O}$ into DMF with a concentration of 48 wt%. Solutions were then spin-coated onto substrates at 4000 rpm for 30 seconds in a nitrogen-filled glovebox. The films were then annealed on a hotplate for 15 min at 100 °C. After the perovskite annealing procedure and the cooling of the substrates to room temperature, a layer of PMMA was deposited by spin-coating a solution of 15 mg PMMA, dissolved in 1 ml of chlorobenzene, at 4000 rpm for 30 seconds. These films were prepared by Haralds Āboliņš.

3.1.3 Mixed-halide perovskite films in flickering study

Perovskite films investigated in Chapter 7 were prepared as described by Li et al.¹⁴⁰ Glass substrates were washed and cleaned in acetone and then isopropanol for 10 min each in an ultrasonic bath. Glass substrates were then treated within an ozone chamber for approximately 10 min. Precursor solutions were prepared in a nitrogen glove box (less than 10 ppm water and oxygen content). Precursors were mixed, i.e. MAI and PbCl_2 (3:1), in anhydrous *N, N*-dimethylformamide (DMF), and the solution was spin coated on glass substrates at 3000 rpm for 60 s. Then, these as-spun films

were annealed at 100 °C in N₂ atmosphere for 60 min. All samples investigated in Chapter 7 were prepared by Cheng Li.

3.1.4 Mixed-cation “sandwich” devices

In Chapter 5 we investigate the response of a high-performing mixed-cation “sandwich” device architecture to background illumination. The device is composed of a triple cation composition: Cs_{0.06}FA_{0.79}MA_{0.15}Pb(I_{0.85}Br_{0.15})₃. These devices were fabricated by Mojtaba Abdi-Jalebi.

Photoanodes were fabricated on laser patterned FTO-coated glass (NSG 10, Nippon sheet glass, Japan). Initially, FTO substrates were cleaned sequentially in 2% Hellmanex detergent, 2-propanol and ethanol, and then treated with an ultraviolet/O₃ cleaner for 15 min. A hole-blocking layer of compact TiO₂ was deposited by spray pyrolysis using a precursor solution of titanium di-isopropoxide bis(acetylacetonate; 0.6 ml titanium acetylacetonate in 8 ml ethanol) on a hot plate at 450 °C. The titanium acetylacetonate was prepared by pouring acetylacetone (Wako Pure Chemical Industries, Ltd.) into titanium isopropoxide (Kanto Chemical Co., Inc.) with a mole ratio of 2:1. For the preparation of the mesoporous TiO₂ scaffold, a commercial TiO₂ paste (Dyesol 18NRT) and two synthesized TiO₂ pastes (NP36 and NP50) were diluted with ethanol (2:7, weight ratio) and were then deposited by spin coating at 5000 r.p.m. for 30 s. After drying at 125 °C, the TiO₂ films were gradually heated to 500 °C and annealed at this temperature for 20 min.

The films are prepared by dissolving PbI₂ (1.2 M), FAI (1.11 M), MABr (0.21 M) and PbBr₂ (0.21 M) in a mixture of anhydrous DMF:DMSO (4:1, volume ratios, v:v) followed by addition of 5 volume percent from CsI stock solution (1.5 M in DMSO). Solutions were then spin coated using a two-step program at 2000 and 6000 rpm for 10 and 40 seconds, respectively, adding 150 µL of chlorobenzene after 30 seconds during the spinning routine. We then annealed the films at 100 °C for 1 hour. All the film preparations were performed under nitrogen in a glove box.

After infiltration of TiO₂ scaffold with the perovskite active layer, the hole transport material (HTM) was deposited by spin coating at 4000 rpm for 30 s. The spin coating formulation of HTM was prepared by dissolving 72.3 mg spiro-MeOTAD, 28.8 ml 4-tert-butylpyridine, 17.5 ml of a stock solution of 520 mg ml⁻¹ lithium bis (trifluoromethylsulphonyl) imide in acetonitrile and 29 ml of a stock solution of 300 mg ml⁻¹ tris(2-(1H-pyrazol-1-yl)-4-tert-butylpyridine) cobalt(III) bis (trifluoromethyl sulphonyl) imide in acetonitrile in 1 ml chlorobenzene. Finally, 70 nm of gold was thermally

evaporated on top of the device to form the back contact. The device fabrication was carried out under controlled atmospheric conditions with a humidity of <1%.

3.2 Device testing

Back-contact perovskite devices (QIBCs) were illuminated from the PMMA side with AM1.5 simulated sunlight (ABET Technologies Sun 2000, calibrated with NREL certified KG5 filtered Si reference diode). Devices, in air at 20 °C, were light soaked for ~1 minute at 1 sun and then measured with a Keithley 2400 in forward and reverse bias voltage scan directions. Scans were performed at 0.38 V s⁻¹ with a hold time of 5 s at 1.2 V. The devices were not masked but the active area was well defined via e-beam lithography which established the photomask, which covers an area of 0.09 cm² per device. Devices were characterised by Maximilian Hörantner and Suhas Mahesh.

3.3 Principles of phase-sensitive detection

Lock-in amplifiers were developed in the 1930s,^{141,142} and extract a signal's amplitude and phase relative to a reference signal using homodyne detection in conjunction with low-pass filtering. Here we will briefly outline the working principles of lock-in based detection, based on Reference [143].

We consider the general case of a signal of interest V_{sig} , which can be described by a sine function as:

$$V_{\text{sig}} = V_S \sin(\omega t + \theta) \quad (3.1)$$

where t is time and V_S , ω , and θ are the signal amplitude, frequency, and phase. In any lock-in based measurement, a reference signal will be compared to a signal of interest and represented similarly as:

$$V_{\text{ref}} = V_R \sin(\Omega t + \Theta) \quad (3.2)$$

where t is time and V_R , Ω , and Θ are the reference amplitude, frequency, and phase.

Multiplication of the two signals together yields:

$$V_{\text{ref}} V_{\text{sig}} = \frac{1}{2} V_S V_R \left[\cos([\omega - \Omega]t + \theta - \Theta) - \cos([\omega + \Omega]t + \theta + \Theta) \right] \quad (3.3)$$

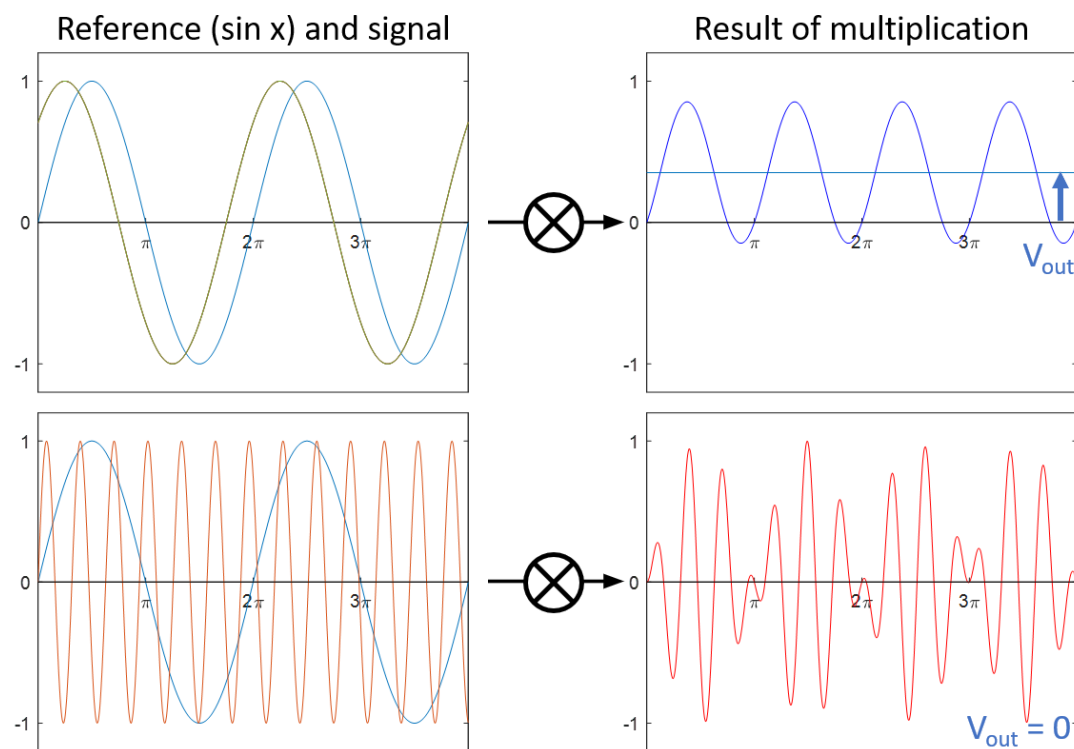


Figure 3.1 Schematic of multiplication of AC signals for lock-in based detection. The upper panels show the multiplication of two sine functions of the same frequency, yielding an AC signal with a DC offset. The lower panels show the multiplication of two sine functions having different frequencies, resulting in no DC offset.

The resulting output is therefore composed of two AC signals, one at the difference frequency ($\omega - \Omega$) and one at the summed frequency ($\omega + \Omega$). By passing the resulting frequency through a low pass filter, the low frequency component is isolated. In the general case, the resulting low frequency AC signal will oscillate around 0 V. However, if the frequencies are identical ($\omega = \Omega$) the low frequency component will become:

$$V_{\text{ref}}V_{\text{sig}} = \frac{1}{2}V_S V_R \cos([\omega - \Omega]t + \theta - \Theta) = \frac{1}{2}V_S V_R \cos(\theta - \Theta) \quad (3.4)$$

Yielding a DC offset signal proportional to the cosine of the phase offset. As the phase of the reference signal is readily adjusted, this process can be used to obtain the amplitude and phase of a given signal. To exemplify this process, Figure 3.1 shows the multiplication of two signals of the same frequency (upper panels) and two signals with unique frequencies (lower panels). Passing the signals through a low pass filter would result in a DC offset in the case of identical frequencies, and no offset for signals having different frequencies.

In this thesis lock-in based detection is used to measure the photocurrent resulting from illuminating a photovoltaic device. Thus, a reference signal corresponding to the “on” and “off” illumination states of the device is needed, and this is achieved via the output signal of a chopper wheel. Obtained currents are converted to voltages via a preamplifier before being fed into a lock-in amplifier. The chopper, preamplifier, and lock-in amplifier were all obtained from Stanford Research Systems (SR540, SR570, and SR830, respectively).

3.4 Photoluminescence spectroscopy

3.4.1 Photoluminescence quantum yield measurements

The PLQE of the samples was measured using an integrating sphere method, described elsewhere.¹⁴⁴ A continuous wave 532 nm diode laser was used to photo-excite the samples with an intensity of 75 mW cm⁻². Emission was measured using an Andor iDus DU490A InGaAs detector.

3.4.2 Confocal photoluminescence microscopy

Confocal microscopy uses a pinhole to limit the detection of light out of the focal plane. The technique has been used by several groups studying metal-halide perovskites, par-

ticularly to study the local variation in photoluminescence⁵⁶ or device performance.¹⁴⁵ The setup described here employs both point detection and point illumination via fibre-coupling and a high-precision piezoelectric stage enabling submicron resolution photoluminescence mapping. The fundamental scheme of the measurements performed is presented in Figure 3.2. The system used is composed of a WITec alpha 300s microscope using fibre-coupled lasers including a 405 nm Coherent CUBE laser and a Fianium WhiteLase High Power Supercontinuum laser (WL-SC-IR-8). Collection is accomplished via a 50 μm multimode fibre, which guides light to a detection system. For standard photocurrent measurements, light is guided to a Princeton Instruments SP-2300i spectrometer fitted with an Andor iDus 401 CCD detector. Two lenses were used: a 100x Nikon ($\text{NA} = 0.95$) and a 40x Olympus ($\text{NA} = 0.6$). Measurements are performed in reflection mode, in air unless stated otherwise.

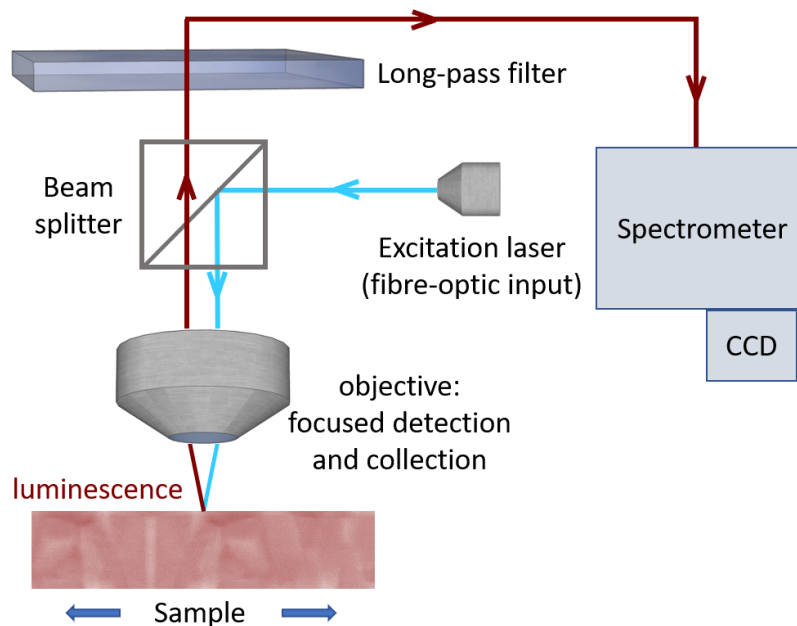


Figure 3.2 Schematic of confocal measurement. Two laser sources, each fibre coupled, are used: a 405 nm continuous wave laser and a supercontinuum WhiteLase 6 ps pulsed laser with a 450 nm band pass filter in the excitation beam path. Two objectives are used: a 100x ($\text{NA} = 0.95$) and a 40x ($\text{NA} = 0.6$). Resulting photoluminescence is passed through a longpass filter to remove the excitation. Spectrally resolved detection is accomplished via a CCD mounted on a spectrometer.

3.4.3 Time-correlated single photon counting

Two lasers were used to perform free space TCSPC measurements on films. A scheme of free space measurement is presented in Figure 3.3a. Measurements were performed using a PicoQuant LDH405 pulsed laser (407 nm wavelength and excitation pulse length and fluence of 100 ps and 5 nJ cm^{-2} , respectively) to excite perovskite films with a repetition rate of 100 kHz. PL was collected at 90° to the incident beam, passed through a monochromator to select the wavelength, then into a photomultiplier detector (Hamamatsu R3809U-50). In the case of the TCSPC data acquired on perovskite samples deposited on SnO_2 , measurements were performed using a Fianium WhiteLase High Power Supercontinuum laser (WL-SC-IR-8) using a 10 nm bandpass filter centred at 450 nm to select the excitation wavelength at a repetition rate of 200 kHz. In this case detection was accomplished using an MPD PDM single-photon avalanche photodiode (SPAD). The excitation pulse length and energy were 6 ps and 5 nJ cm^{-2} , respectively. Light was collected at an angle of 30° relative to the incident beam and passed through a 700 nm longpass filter to remove the contribution of the excitation.

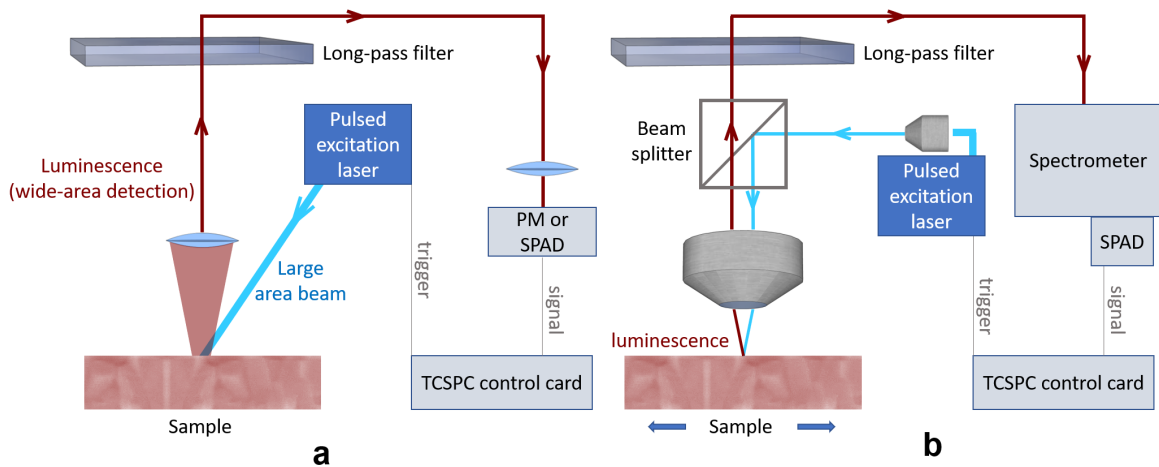


Figure 3.3 a) Schematic of free space TCSPC measurement. A pulsed 407 nm or supercontinuum laser with a 450 nm band pass filter are directed without focus to generate a large excitation spot ($>1 \text{ mm}$ diameter) on the sample. Resulting PL is collected and passed through a longpass filter before being directed to a photomultiplier or single photon avalanche diode. b) Schematic of local TCSPC accomplished via a WITec 300s microscope. Pulsed supercontinuum light is fibre-coupled after a 450 nm bandpass filter. Resulting PL is collected via a confocal pinhole and a longpass filter is used to remove the excitation wavelengths. Detection is accomplished via a spectrometer and a SPAD. In each case the laser trigger and PM/SPAD signal pulses are used to generate photoluminescence decays.

In addition to free space measurements, TCSPC measurements are presented in Chapters 6 and 7 via a confocal microscope. The setup is identical to that presented previously using the Fianium laser, however the detection is accomplished via an avalanche photo diode (APD) mounted on the Princeton instruments spectrometer, as depicted in Figure 3.3b. Repetition rates for confocal measurements were 5 MHz.

3.5 Scanning photocurrent microscopy

Combined photoluminescence and photocurrent was measured using a WITec alpha 300s setup. The schematic for photocurrent measurements is presented in Figure 3.4. The excitation source was a 405 nm continuous wave laser (Coherent CUBE), chopped using a Stanford Research SR 540 chopping unit at 800 Hz with a 50% duty cycle. The light was coupled through an optical fibre to the microscope and focused using a 40x Olympus lens (NA = 0.6, spot size 1.5 μm). Samples rested on an X-Y piezo stage of the microscope. The PL signal was collected in reflection mode with the same 40x objective and detected using a Princeton Instruments SP-2300i spectrometer fitted with an Andor iDus 401 CCD detector. A longpass filter with a cut-off wavelength of 450 nm was fitted before signal collection to block the excitation.

Photocurrent detection was accomplished using micro needle probes which feed a Stanford Research SR 570 preamplifier. The signal from the preamplifier was detected as current intensity and phase shift using a Stanford Research SR 830 lock-in amplifier (referenced to the chopper frequency). By movement of the sample stage, maps of combined PL and photocurrent were recorded. All measurements were performed under short-circuit conditions. All movements of the stage and lenses, and all spectral and photocurrent data was recorded using WITec Control 4 software. All measurements were performed in air. All photocurrent and PL data trends for spatial scans are the result of averaging over at least 10 scans.

Conversion of the measured phase offset ($\Delta\theta$) of photocurrent signal to characteristic rise time (T_{Rise}) via the chopping frequency. For 800 Hz chopping frequency, conversion was as follows:

$$T_{\text{rise}} = \frac{\Delta\theta}{360} \times \frac{1}{800 \text{ Hz}} \quad (3.5)$$

Photocurrent measurements presented in chapters 4 and 5 were performed with 50 - 3200 nW of average illumination power. These powers translate to intensities of 0.7 - 45 W cm⁻².

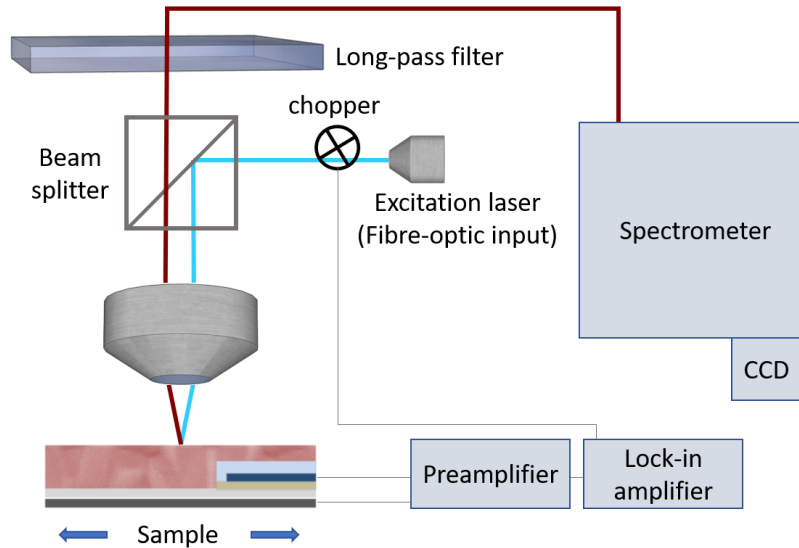


Figure 3.4 Schematic of scanning photocurrent microscopy setup. The setup is similar to that described in Figure 3.2, using the 405 nm continuous wave laser. In this case, however, the laser excitation is chopped using an SR 540 chopping unit at 800 Hz and 50% duty cycle. The device investigated is contacted via micro needle-probes and current resulting from photoexcitation is detected using a preamplifier and lock-in amplifier using the chopping signal to improve the signal-to-noise ratio and to supply temporal information via detected photocurrent phase.

3.6 Comparing laser intensities and obtained photocurrent amplitudes

Several types of spectroscopy are employed in this thesis, each involving laser illumination in different situations, ranging from continuous illumination localised to a small spot via a microscope objective, to measurements of a relatively large area of sample illuminated with short pulses of light. To ease in comparison, fluences will be compared to one sun of illumination. 1 sun of illumination is 1000 W cm⁻², but spans over a wide range of wavelengths, many of which are not absorbed by the perovskite materials studied here. As carrier density is the value of interest, this thesis will use the number of available photons for absorption per second to compare illumination conditions. Using the ASTM reference spectra for AM1.5 illumination, the integrated

Table 3.1 Comparison of photocurrent and laser intensity. Charge injection is accomplished via a chopped 405 nm laser source focused to a small spot ($\sim 1.5 \mu\text{m}$) resulting in high local intensity. Photocurrents are obtained via lock-in based detection. The EQE presented here is the number of number of electrons out calculated from the current, divided by the photon flux into the system.

Ave. Power (μW)	Photons Delivered (s^{-1})	Suns	Current (nA)	“EQE”
0.05	1×10^{11}	10	8.8	0.54
0.1	2×10^{11}	20	17	0.52
0.2	4×10^{11}	40	28	0.43
0.4	8×10^{11}	80	50	0.38
0.8	16×10^{11}	160	88	0.33
1.6	33×10^{11}	310	141	0.27
3.2	66×10^{11}	620	235	0.22

number of photons with energy greater than 1.55 eV incident on the Earth’s surface is $1.5 \times 10^{21} \text{ m}^{-2} \text{ s}^{-1}$.¹⁴⁶ To provide an example conversion, PLQE measurements were taken at 75 mW cm^{-2} with 532 nm illumination. This corresponds to a photon flux of $2 \times 10^{21} \text{ m}^{-2} \text{ s}^{-1}$ or approximately 1 sun of illumination. Table 3.1 provides further comparisons of laser power to number of suns for confocal photoluminescence and photocurrent measurements.

In the case of photocurrent measurements, each amplifier unit has a variable level of amplification, spanning roughly nine orders of magnitude for each system. The amplification settings for diffusion length measurements presented in Chapters 4 and 5 were $1 \times 10 \mu\text{A V}^{-1}$ and $1 \times 10 \text{ mV V}^{-1}$ for the preamplifier and lock-in amplifier, respectively. The total amplification was therefore seven orders of magnitude. To fully quantify the output current in photocurrent measurements, the shape of the photocurrent signal and the frequency response of the investigated device must be known.¹⁴⁷ However, a rough estimate of EQE is possible via comparison of obtained photocurrent signals to the number of photons incident on the device. To provide an example of this, peak photocurrents obtained on a back-contact device measured at varying fluences are compared to the calculated number of photons delivered per second in Table 3.1.

Chapter 4

Electron and hole transport dynamics in polycrystalline perovskite films

Metal-halide perovskites are promising solution-processable materials for efficient solar cells⁵ and LEDs,¹⁴⁸ and show unexpectedly high diffusion ranges for photogenerated charges. We explore here the scope for back-contact architectures, which provide the best performance in silicon solar cells.⁶ We prepare thin films of perovskite semiconductors over laterally-separated electron- and hole-selective materials of SnO_x and NiO_x, respectively. Upon illumination, electrons (holes) generated over SnO_x (NiO_x) rapidly transfer to the buried collection electrode, leaving holes (electrons) to diffuse laterally as majority carriers in the perovskite layer. We characterise the transport behaviour of charge carriers propagating laterally through polycrystalline films: quantifying charge diffusivities and demonstrating that in our architecture diffusion lengths exceed 12 μm, which is an order of magnitude higher than values reported in operating devices to date.^{110,117} We report back-contact solar cells with short-circuit currents as high as 18.4 mA cm⁻², giving 70% external quantum efficiency. With improved control of fabrication, we consider it possible to achieve back-contact perovskite devices with 20% efficiency for electrode separations of 10 μm or more. We note also that this device structure provides a powerful experimental platform for the study of electron- or hole-only transport phenomena.

This chapter is based on transport measurements in Ref. [149].

4.1 Background and motivation

Design of high efficiency devices requires an understanding of charge transport lengths and recombination rates. In LEDs the distance charges travel limits device dimensions, while nonradiative recombination reduces solar cell device efficiency. In the classic semiconductors gallium arsenide and silicon, transport dynamics of individual charge carriers were examined in doped n - and p -type materials.^{150,151} In halide perovskites, however, excess charge tends to be compensated by intrinsic defects, or mobile ions, thus no substitutional or chemical doping has been achieved to date. Similarly, though some success has been achieved with n -type FETs, field effect mobilities are low and likely compromised by ionic screening.¹⁰³ Thus, it has proven challenging to measure individual charge transport properties in perovskite materials. In this regard metal-halide perovskites have been compared to chalcopyrites,⁴⁸ which also possess electrically-active defects resulting in high compensation ratios.¹⁵²

Charge transport dynamics can be approached theoretically and via several measurement techniques (several outlined in Chapter 2), however. Theoretical methods rely on band diagram calculations, such as DFT. There is large variation in the predicted transport behaviour of perovskite materials in literature, with predicted mobilities ranging from hundreds⁸⁹ to thousands³⁵ of $\text{cm}^2 \text{Vs}^{-1}$. Several methods are used to measure charge transport within perovskites, and similarly provide a wide range of transport values.

First we consider measurements on time scales in the nanosecond regime and beyond in the absence of applied field, achieved through techniques such as scanning photocurrent measurements, time-resolved photoluminescence (TRPL), time-resolved terahertz (THz) spectroscopy, time-resolved microwave conductivity (TRMC), photoluminescence quenching (PLQ), and transient absorption (TA) microscopy. Resulting diffusion lengths and diffusivities range from 1 – 77 μm and 0.001 – 3 $\text{cm}^2 \text{s}^{-1}$, respectively (details in Table 4.1). We note that these previous measurements either (i) rely on two independent measurements to extract transport behaviour (e.g. TRPL and PLQ in Ref. [110]), or (ii) are unable to distinguish between the transport properties of electrons and holes (e.g. TA microscopy, TRMC).

Several applied field techniques have been employed on devices including field effect transistors (FET) and time-of-flight (TOF) measurements. Both vertical⁹⁷ and lateral¹⁵³ charge transport have been studied using time-of-flight, with reported charge mobilities ranging from 0.5 to 6 $\text{cm}^2 \text{Vs}^{-1}$. In addition to the effects of applied field,

Grill et al. found that time-of-flight measurements in vertical devices are affected by charge extraction materials, and found that the thickness of selective electrode materials increases charge transport time and therefore reduces observed charge mobility.¹⁵³

In addition to the lack of an established means of investigating directly and independently the transport of electrons and holes without the application of external field, we note two other open questions in the literature: i) the effect of grain boundaries on charge transport, and ii) charge transport dynamics in operating devices. Here, we present an architecture which segregates photogenerated charge carriers using selective electrode materials. By combining phase-sensitive detection with high-precision photocurrent scanning of our architecture, we isolate the behaviour of photogenerated charges within the perovskite film. We characterise the transport dynamics of electrons and holes separately, and report diffusivities in polycrystalline MAPbI₃ films of $D_{electrons} = 0.13 (\pm 0.05) \text{ cm}^2 \text{ s}^{-1}$ and $D_{holes} = 0.07 (\pm 0.03) \text{ cm}^2 \text{ s}^{-1}$. Furthermore, we find diffusion lengths for each carrier exceed 12 μm in our architecture, and report a device with 70% external quantum efficiency, demonstrating the potential of back-contact architectures for high performing perovskite devices.

4.2 Characterising back-contact devices

In order to investigate the potential of back-contact device architectures, and the potential to harvest carriers with long extraction lengths, quasi-interdigitated back-contact (QIBC)¹³⁸ devices were fabricated in Oxford by Maximilian Hörantner and Suhas Mahesh. Here, thin films structures are accomplished by depositing polycrystalline methylammonium lead triiodide (MAPbI₃) on charge-selective hole- and electron-conducting layers: NiO_x and SnO_x, respectively. First, SnO_x is deposited over FTO, and then interdigitated fingers of an insulator (Al₂O₃) topped by an Ni/NiO_x electrode were deposited over a 3 × 3 mm active area. The distance between fingers varies from 1 – 10 μm (Figure 4.1a,b). The current-voltage characteristics of the QIBC device under AM1.5 conditions (Figure 4.1c) shows a short-circuit current density (J_{SC}) of 18.4 mA cm⁻², which is the highest J_{SC} reported to date for a perovskite back-contact device.^{138,154,155} The device power conversion efficiency (PCE) reaches 4.1%, which is limited by a fill factor of 38% and an open-circuit voltage (V_{OC}) of 0.57 V. These values are mainly affected by substantial dark leakage currents indicative of an imperfect shunt resistance which may be caused by the imperfection of the Al₂O₃ insulator.

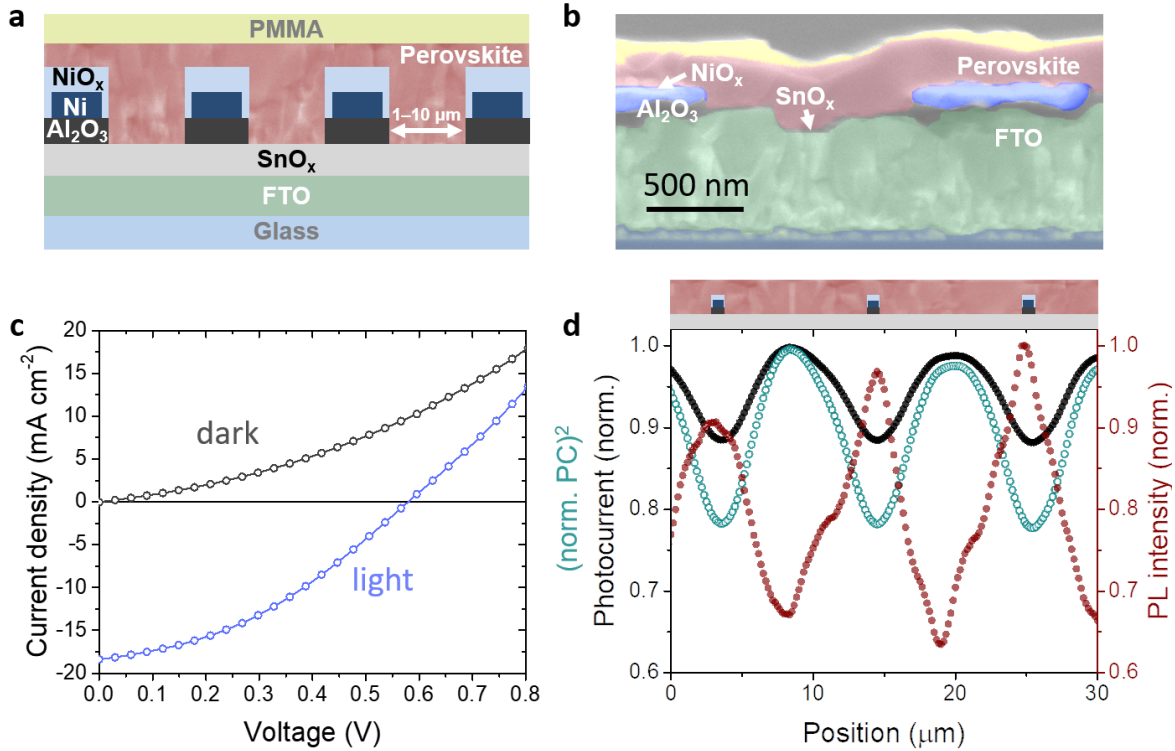


Figure 4.1 (a) Schematic of QIBC solar cell cross-section. An electron-selective SnO_x layer covers FTO coated glass, and hole-selective fingers, composed of a Ni core with a NiO_x shell, are electrically isolated from SnO_x with an Al₂O₃ layer. MAPbI₃ was spin-coated over this structure and topped with PMMA. The NiO_x contacts are 1 μm wide. (b) Coloured SEM of the device cross-section. The MAPbI₃ film has a crystallite size of ~500 nm. SEM was taken by Maximilian Hörantner. (c) JV curve of QIBC device with NiO_x finger separation of 1 μm. (PCE = 4.1%, FF = 0.38, V_{OC} = 0.57 V, J_{SC} = 18.4 mA cm⁻²) (d) Variation in photoluminescence intensity and photocurrent over the active area of a device with 10 μm separation between NiO_x electrodes. PL and photocurrent are anti-correlated, though shape and magnitude of variation of each is distinct. To highlight differences between resulting PC and PL, the square of normalised photocurrent is plotted. The <15% variation in photocurrent over the 10 μm pitch distance demonstrates that charges generated over either electrode have similar collection efficiencies. PL and photocurrent intensity are measured concurrently, using 11 W cm⁻² average power of 405 nm focused light (spot size ~1.5 μm). Photocurrent and photoluminescence intensity plotted in (d) are the result of averaging over 140 scans over a 30×70 μm section of the device.

Figure 4.1d shows the variation of photocurrent and photoluminescence over a 30 μm subsection of the active area of a device with 10 μm pitch. Illumination over the NiO_x fingers results in higher photoluminescence intensity, but reduced photocurrent; while illumination between fingers, over SnO_x , has the opposite effect. This indicates that, over NiO_x , the rate of extraction and/or the diffusivity of holes is lower than that of electrons resulting in a stronger spatial overlap of the equilibrium electron and hole populations. Photocurrent maxima over the electron extraction layer indicates that holes diffuse at a higher rate and/or have a longer lifetime, which allows a larger fraction to diffuse to the NiO_x fingers. The variation in photoluminescence is 38%, while variation in photocurrent is 15%. This difference in the magnitude of variation can partially be attributed to the bimolecular nature of PL, which make it more sensitive to the local carrier concentration. To further examine this, we also present the square of normalised photocurrent in Figure 4.1d. While this curve is more similar to the anticorrelation of photoluminescence, the magnitude of the variation and the shape are distinct. This is the result of PL probing the local overlap of equilibrium electron and hole densities, while photocurrent probes long range transport of carriers across the cell. Furthermore, the low modulation in the extracted photocurrent demonstrates that charge extraction remains relatively efficient over the channel, regardless of the location of the excitation in the device.

The reported short-circuit current of 18.4 mA cm^{-2} highlights the possibility for efficient charge collection in halide-perovskite solar cells with QIBC architecture. However, the high dark leakage currents in our devices under applied bias require improvements in electrode fabrication. Although effort is clearly required for further optimisation of cell fabrication, there appears to be no fundamental reason why QIBC perovskite cells cannot achieve fill factors and open-circuit voltages comparable with the state-of-the-art sandwich structure devices, with the advantage of the feasibility of delivering higher short-circuit current, ultimately leading to improved efficiency.

4.3 Scanning photocurrent spectroscopy on back-contact architectures

The high short-circuit currents presented in Figure 4.1 demonstrate effective charge extraction at short-circuit. We aim to use this system to explore charge transport dynamics in perovskite devices. Figure 4.2 provides a schematic of the sample architec-

ture and the measurement setup (fabrication details in Chapter 3). In our measurement architecture we investigate the junction of two continuous (>1 mm) regions composed of perovskite in contact with electron- or hole-extracting electrodes (SnO_x/FTO and NiO_x/Ni , respectively).

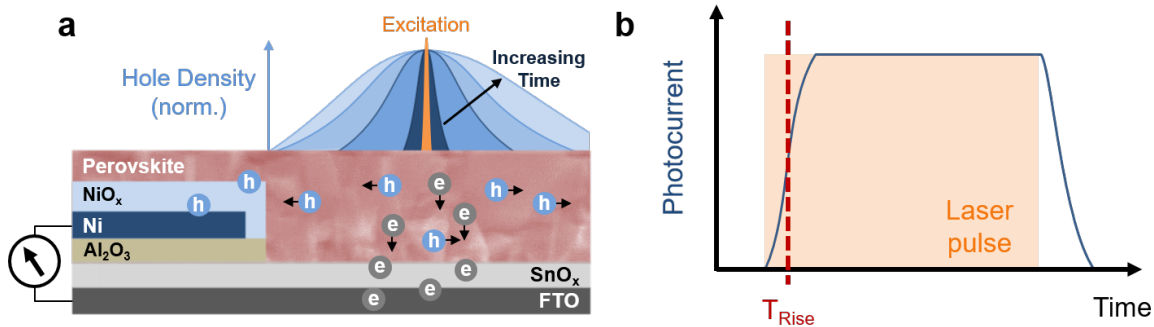


Figure 4.2 (a) Schematic of investigated architecture and spatially-resolved charge transport detection. Charge selective layers NiO_x and SnO_x extract photo-generated holes/electrons, respectively, leaving the opposite charge in the halide perovskite. Here, charges are photoexcited in the perovskite layer over SnO_x a certain distance from the NiO_x — SnO_x electrode junction. Blue curves represent the development of hole population with time after initial excitation, where majority charge carriers diffuse radially until charge generation balances charge recombination and extraction to reach steady-state conditions. Dark blue curves correspond to early times, while light blue curves approach steady-state conditions. (b) Evolution of photocurrent with time under illumination (the orange area represents illumination time) with characteristic rise time T_{Rise} , which is quantified from the photocurrent phase measured by a lock-in amplifier.

We probe our architecture using scanning photocurrent and photoluminescence microscopy^{83,113} to resolve charge population dynamics and transport in MAPbI_3 films at short-circuit, which prevents the development of a lateral electric field. A chopped continuous wave laser source is focused on a local area ($\sim 1.5 \mu\text{m}^2$) of the film, and the resulting photocurrent amplitude and phase are measured with high sensitivity using a lock-in amplifier. Upon local excitation, generated charges diffuse until steady-state conditions are reached (light blue curve, Figure 4.2a). The temporal response of the photocurrent (Figure 4.2b) is determined by the balance of transport and recombination rate of the electrical carriers. The phase delay between the chopped excitation and the photocurrent signal is used to determine a characteristic photocurrent rise time.

Figure 4.3 provides optical (a) and scanning electron (b) micrographs of investigated films. Figure 4.3a shows a typical region of measurement, with the more opaque NiO_x region visible on the left of the image. The laser is rastered over a $170 \times 10 \mu\text{m}$ section of film, with the NiO_x — SnO_x junction centred in the middle of the $170 \mu\text{m}$

raster direction. To reduce the influence of local variation in film quality, ten scans are taken and the resulting photocurrent is averaged for each excitation—junction distance. Figure 4.3b displays the typical grain size of investigated MAPbI₃ films, which is ~500 nm. Photocurrent measurement is therefore accomplished over distances much larger than the characteristic perovskite grain size.

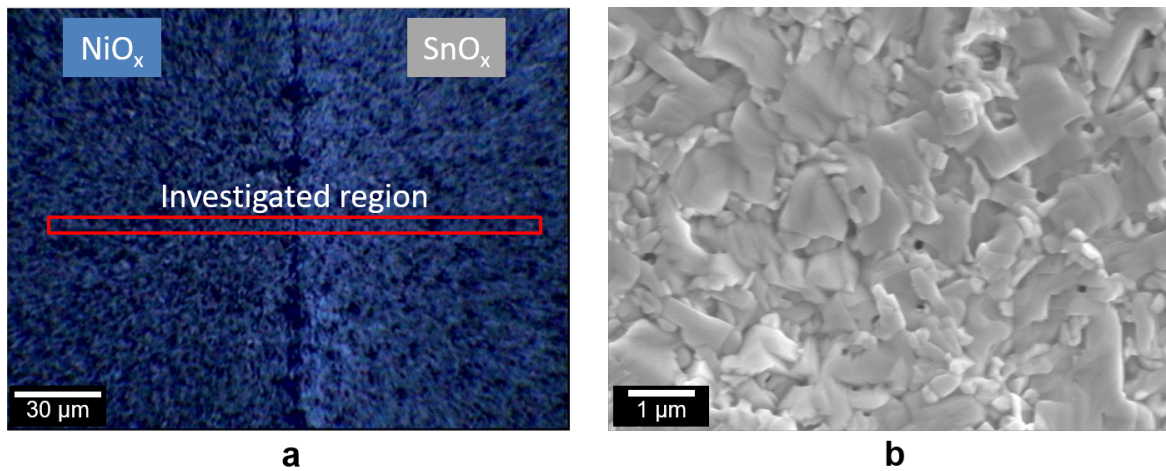


Figure 4.3 (a) Optical micrograph of typical region investigated via scanning photoluminescence and photocurrent measurements (investigated region outlined by red box). To the left, the more opaque region of MAPbI₃ deposited over the hole-conductive layer NiO_x is clearly distinguished from the region on the right of the image where MAPbI₃ is deposited over SnO_x. (b) Scanning Electron Micrograph showing the typical size of MAPbI₃ grains investigated. This SEM was captured by Suhas Mahesh.

Scanning photocurrent measurements are accomplished via chopped laser excitation, as depicted in Figure 4.2b. This serves the purpose of improving signal-to-noise (via lock-in based detection) and allowing for the temporal response of the device to be monitored. To ensure consistent measurement of the temporal response of devices, the frequency dependence of photocurrent amplitude is presented in Figure 4.4a for excitation at an excitation—junction distance of 10 μm over MAPbI₃ deposited over the SnO_x region. The magnitude of photocurrent detected by the lock-in amplifier reduces by ~30% over an order of magnitude increase in chopper frequency (going from 200 to 4000 Hz). This reduction in photocurrent at high frequencies is indicative of a long-lived photocurrent tail, reducing the magnitude of the photocurrent oscillation (Figure 4.4b). We observe that photocurrent remains within 10% of its peak value at chopping frequencies <1000 Hz. Subsequent measurements are performed at a chopping frequency of 800 Hz as it provides good signal while significantly reducing acquisition rates relative to lower frequencies.

We further note that we use phase sensitive detection to isolate the system response at the reference (chopper) frequency. As the only variable in each measurement is the distance to an electrode junction, we detect changes in signal only at the reference frequency and only as a result of changing distance to the electrode junction. As a result, any processes which act out of frequency with the excitation will not contribute.

First, we explore the influence of charge trapping. Carriers which are trapped in the system and recombine will not contribute to photocurrent. Some carriers which had been trapped may be excited back into a conductive state, however. Such detrapping of carriers will only contribute to signal if the average detrapping time is less than, or near, the characteristic timescales of the experiment (~ 100 μs). Carriers with detrapping times longer than this will not have an effect as their release will result in a random, incoherent contribution to photocurrent.

Extraction dynamics may have another possible effect on photocurrent measurements. Grill et al. showed that the thickness of charge extraction layers can effect time-of-flight measurements.¹⁵³ Slowing of charge extraction at selective electrodes will contribute to a phase shift and potentially change the shape or reduce the absolute value of photocurrent signal. The lock-in measurements presented here, however, determine the relative characteristic rise time and photocurrent amplitude while only varying the spatial separation of the excitation and electrode junction. Therefore, results presented here will be unaffected by potential slow charge extraction effects at selective electrodes which remain constant throughout the measurement.

4.4 Characterising charge carrier transport

In order to quantify charge carrier transport and recombination from photocurrent measurements a model prepared by Lamboll is used.¹⁵⁶ This model considers the diffusion of electrons and holes in the investigated geometry assuming monomolecular recombination. Here we summarise the relevant conclusions and describe how values are obtained in this work.

Lamboll showed that the complex diffusion problem presented in photocurrent measurements (Figure 4.2) can be one-dimensionalised using a correction factor to account for the radial diffusion of photogenerated carriers and the response of the lock-in amplifier used in the measurement. In his work, Lamboll shows that in the case of monomolecular recombination an exponential decay of photocurrent is expected both in the case of high rates of charge extraction yielding unipolar charge transport,

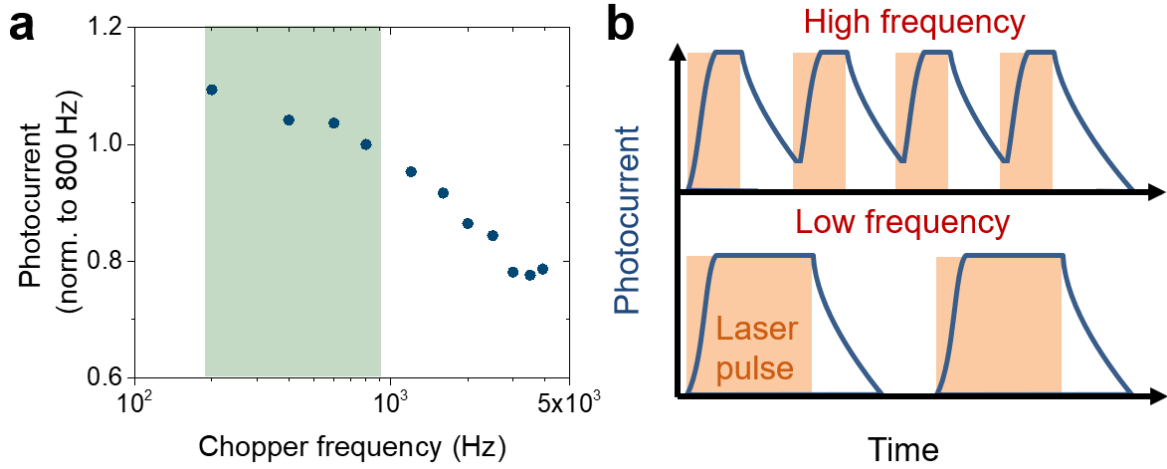


Figure 4.4 a) Photocurrent obtained at varying laser chopping frequencies. 405 nm focused light (spot size $\sim 1.5 \mu\text{m}$) at intensities of 11 W cm^{-2} is used to excite a device at an excitation—junction distance of $10 \mu\text{m}$ over the SnO_x region. b) Schematic describing the influence of chopper frequency on photocurrent measurements. We present the influence of a long-lived photocurrent tail. At high frequencies (upper graph), this tail persists beyond the arrival time of the subsequent laser pulse, reducing the magnitude of photocurrent oscillation.

and in cases of low charge extraction rates involving ambipolar transport. Lamboll therefore investigated the accuracy of the model for a range of charge diffusivities ($0.2 - 4.5 \text{ cm}^2 \text{ s}^{-1}$), and a range of charge extraction velocities ($100 - 400000 \text{ cm s}^{-1}$) which result in charge densities ranging from $10^{14} - 10^{18} \text{ cm}^{-3}$ depending on the kinetics of the investigated system. It is found that towards the limit of low extraction speed and low diffusivity, the high carrier concentration and significant contribution of radiative recombination will result in discrepancies between a one-dimensionalised model and expected system behaviour. Lamboll shows, however, that assuming variation in carrier concentration with film height is small yields highly accurate one-dimensionalised results even at the low diffusivity, low extraction rate limit. Indeed, Lamboll argues that if an electrode extraction current is amenable to one-dimensionalisation, then the whole system can be accurately represented in one-dimension, given a correction factor. Lamboll finds that photocurrent amplitude (PC) will vary with excitation—junction distance (x) as:

$$PC \propto \exp -\sqrt{\frac{k}{D}}x \quad (4.1)$$

where k is the total rate of recombination and D is the diffusivity of the carrier remaining within the perovskite film. Similarly, for time-resolved measurements the time to equilibrium (T_{Rise}) is found to vary as:

$$T_{\text{Rise}} = \frac{0.43}{\sqrt{Dk}}x + C \quad (4.2)$$

where C is an offset given by the system response. The factor 0.43 arises as a correction factor, dependent on the investigated geometry but predicted to apply for a wide range of diffusivities and rates of recombination.

By using the results of photocurrent amplitude and rise time, the diffusivity and rate of recombination can be estimated. The diffusion length here corresponds to the distance from the electrode at which the photocurrent has decayed to $1/e$ of its peak value. This is related to the distance carriers can travel within the perovskite over the electrode which does not accept them. The diffusion length is the characteristic length scale representing the expected displacement of carriers before recombination or extraction, which is related to the carrier root mean squared displacement. Here, we are sensitive to the average motion within the plane of the perovskite film, which is much larger than the film thickness, therefore we consider the mean square displacement ($\langle r^2 \rangle$) of a carrier in two dimensions:

$$\langle r^2 \rangle = \langle x^2 \rangle + \langle y^2 \rangle \quad (4.3)$$

where x and y are orthogonal displacements within the plane of the perovskite film. Classically, mean square displacement in each dimension varies with diffusion coefficient (D) and lifetime (τ_l) as: $\langle x^2 \rangle = 2D\tau_l$. Therefore, the root mean square displacement of an electron or hole in two dimensions is:

$$\sqrt{\langle r^2 \rangle} = 2\sqrt{D\tau_l} \quad (4.4)$$

We choose to present the diffusion length as $L_D = \sqrt{\langle r^2 \rangle}/2$ as it is common to report $L_D = \sqrt{D\tau_l}$.

To investigate how far charges travel in our device, the photocurrent amplitude is measured at varying distances between the excitation spot and the NiO_x — SnO_x junction (Figure 4.5a). The measured photocurrent follows an exponential decay with increasing excitation—junction distance, both when exciting over NiO_x and SnO_x . This indicates that the primary recombination pathway in the investigated system is

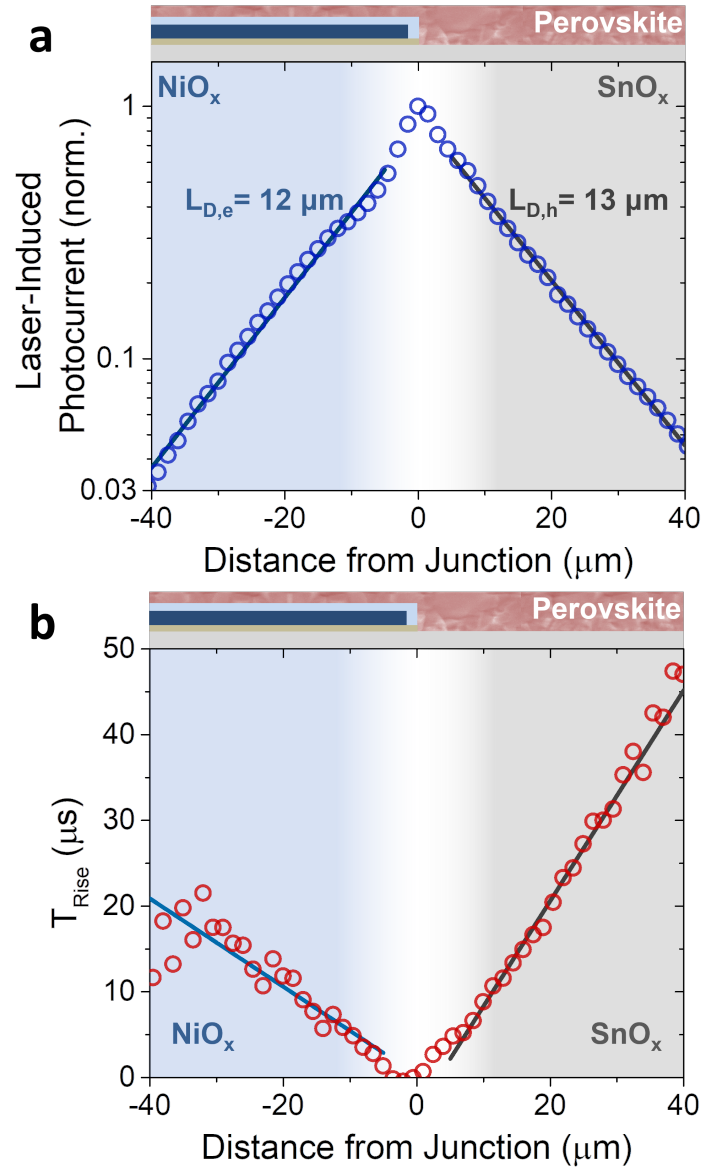


Figure 4.5 Variation of photocurrent (a) and rise time (b) with distance from the electrode junction. The photocurrent decays exponentially with distance from the electrode junction, yielding characteristic charge diffusion lengths of $L_{D,electrons} = 12 \mu\text{m}$, and $L_{D,holes} = 13 \mu\text{m}$. By fitting to a diffusion model (Ref. [156]) the charge carrier recombination velocity (v) and diffusion constant (D) were extracted: $v_{NiO_x} = 1.7 (\pm 0.5) \text{ cm s}^{-1}$ and $v_{SnO_x} = 1.1 (\pm 0.3) \text{ cm s}^{-1}$ / $D_{electrons} = 0.13 (\pm 0.05) \text{ cm}^2 \text{ s}^{-1}$ and $D_{holes} = 0.07 (\pm 0.03) \text{ cm}^2 \text{ s}^{-1}$. Measurements were taken with an average excitation power of 5.6 W cm^{-2} , or ~ 80 suns. Scans were performed over $5 \times 170 \mu\text{m}$ with sampling points every 500 nm and a 200 ms integration time.

monomolecular in nature, indicating that application of a one-dimensionalised model is appropriate. We extract the electron and hole carrier diffusion lengths for this device from exponential fits to the data, which yield values of $L_{D,electrons} = 12 \mu\text{m}$, and $L_{D,holes} = 13 \mu\text{m}$. Thus, we find that the radial root mean square displacement ($\sqrt{\langle r^2 \rangle}$) for electrons and holes traveling over the electrodes which do not accept them is $24 \mu\text{m}$ and $26 \mu\text{m}$, respectively. Near the position of the junction, we observe a deviation from the expected mono-exponential decay of photocurrent. This could be due to several effects, including: optical edge effects, inconsistencies in film thickness, field effects at the junction, ion migration effects,^{55,56,157} or a transition to grain boundary-free transport. As we cannot decouple these effects, we exclude the central region in our fits. The amount of photocurrent collected over the two regions differs, with 40% more photocurrent collected over SnO_x than over NiO_x at $40 \mu\text{m}$ excitation—junction distance. This agrees with photocurrent measurements in Figure 4.1, where photocurrent over SnO_x is found to be higher than over NiO_x for a given excitation—junction distance. We note that in either direction, over 3% of peak photocurrent is still collected at distances of $40 \mu\text{m}$, which corresponds to an EQE on the order of 1% for these large separations. This suggests that grain boundaries, which occur every $\sim 500 \text{ nm}$ in the investigated system, can be overcome by charge carriers under investigated conditions.

We investigate the temporal evolution of carrier populations from the photocurrent rise time versus distance (Figure 4.5b). The rise time increases linearly with distance, as expected, since the phase of the lock-in amplifier measures the signal onset time, not the arrival time of the integrated photocurrent.¹⁵⁶ Excitation over SnO_x (p -type perovskite) results in larger values of rise time than excitation over NiO_x (n -type perovskite). This indicates that holes take a longer time than electrons to travel to the electrode junction, indicative of a lower effective diffusion coefficient for holes. Summarising photocurrent results, both photocurrent amplitude and rise time is higher over SnO_x , indicating that holes diffuse more slowly than electrons and that charges moving over SnO_x recombine at a lower rate.

To quantify diffusivities and carrier lifetimes from our photocurrent measurements we return to the reported diffusion model presented previously. We extract recombination velocities of $v_{\text{NiO}_x} = 1.7 (\pm 0.5) \text{ cm s}^{-1}$ and $v_{\text{SnO}_x} = 1.1 (\pm 0.3) \text{ cm s}^{-1}$, as well as diffusivities of $D_{\text{electrons}} = 0.13 (\pm 0.05) \text{ cm}^2 \text{ s}^{-1}$ and $D_{\text{holes}} = 0.07 (\pm 0.03) \text{ cm}^2 \text{ s}^{-1}$. Notably, the recombination velocity in the operating QIBC devices is unexpectedly low compared with isolated “non-contacted” materials,¹⁵⁸ approaching passivated crystalline silicon, for which surface recombination values as low as 0.25 cm s^{-1} have been

reported.¹²⁴ Comparing reported recombination velocities to the film thickness (h) to calculate carrier lifetime (τ_l), $\tau_l=h/v$, we find lifetimes of 27 μs for holes in MAPbI₃ over the SnO_x electrode, and 17 μs for electrons over the NiO_x electrode.

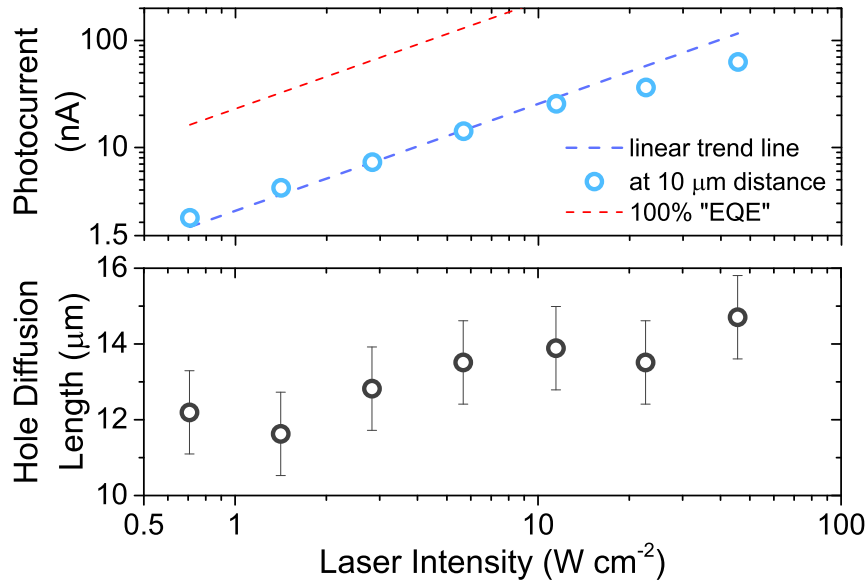


Figure 4.6 Photocurrent and hole diffusion length vs laser intensity measured over SnO_x. Upper panel: Photocurrent amplitude obtained at varying intensities. Photocurrents were obtained at 10 μm electrode—junction separation. Two linear relations are plotted, one in red shows expected 100% “EQE” at varying laser intensity as described in Chapter 3, and another linear trend line to show that the fraction of carriers being extracted reduces at high excitation densities ($>10 \text{ W cm}^{-2}$ or >100 suns). Lower panel: Hole diffusion lengths obtained at varying excitation power. Observed diffusion length increases slightly with laser intensity. Error bars correspond to the standard deviation observed for eight measurements at 5.6 W cm^{-2} .

We examine the excitation dependence of charge transport properties of MAPbI₃ polycrystalline films in Figure 4.6. Here, the absolute photocurrent obtained at 10 μm excitation—junction distance over the SnO_x region is presented at varying local laser illumination intensity. The average power of the chopped 405 nm laser varies from 0.7 W cm^{-2} to 45 W cm^{-2} . For this range, we observe in the upper plot of Figure 4.6, that photocurrent amplitude rises linearly with average excitation power until local illumination power exceeds 10 W cm^{-2} . This behaviour is expected as at high illumination intensities the proportion of photogenerated carriers which recombine radiatively increases, reducing obtained photocurrent. In addition, the red dashed line

provides the expected order of magnitude photocurrent in the case of a device with 100% EQE.

In the lower plot of Figure 4.6, we observe that the diffusion length of holes increases slightly with excitation power. This behaviour indicates that, for the investigated excitation densities, carrier-carrier scattering is not the dominant scattering process as this would result in the opposite trend. Instead, it is possible that the increasing charge density reduces the influence of trap states or reduced influence of energetic barriers to charge transport (e.g. grain boundaries).^{102,159} The dependence of diffusion length on excitation density, however, is relatively weak as diffusion length increases from 11.5 to 14.7 μm over two orders of magnitude of average excitation power.

4.5 Discussion

Our findings here have implications towards understanding broader phenomena in metal-halide perovskites and solar cells. Photo-induced halide migration in halide perovskite materials has been reported,^{55,56,157} but the origin is still under debate. We find that electron diffusivities are roughly twice that of hole diffusivities in polycrystalline MAPbI_3 . Such a difference in hole/electron diffusivity would likely lead to an excess of holes at the point of excitation, which would result in a radial field under steady-state, point excitation conditions. Any ion migration within these fields would then be reversible after the excitation is removed. While seemingly counter-intuitive, we do not expect measurements presented here to be heavily influenced by ion migration. Measurements are performed over long timescales (>30 min), with zero applied bias. Each probed volume is illuminated for a limited amount of time (~ 1 s) and there are several minutes between each raster step. Therefore we anticipate contributions of ion migration to be limited by both the short illumination duration and the extended periods of relaxation between line scans.

Furthermore, the effect of perovskite polycrystallinity on device performance remains an active area of investigation, with reports using spatially-resolved photoluminescence to study if grain boundaries impede charge transport.^{71,108} We perform measurements of photocurrent at excitation—junction separations much larger than the grain size, and find that large fractions of excited carriers travel across multiple grain boundaries. This demonstrates that under investigated conditions, grain boundaries are not major impediments to charge motion in the polycrystalline MAPbI_3 films which we have

Table 4.1 Survey of reported transport parameters in MAPbI₃ and MAPbI_{3-x}Cl_x polycrystalline films and devices.

Material	Method	D (cm ² s ⁻¹)	μ (cm ² Vs ⁻¹)	L_D (μ m)	τ_t (ns)	reference
MAPbI ₃	TRPL/PLQ	0.017(e^-), 0.011(h^+)	–	0.13(e^-), 0.10(h^+)	9.6	[110]
MAPbI _{3-x} Cl _x	TRPL/PLQ	0.042(e^-), 0.054(h^+)	–	1.1(e^-), 1.2(h^+)	270	[110]
MAPbI ₃	TRPL/THz	–	8.1	–	66	[92]
MAPbI _{3-x} Cl _x	TRPL	–	11.6	–	–	[92]
MAPbI ₃	THz	–	25	–	–	[93]
MAPbI ₃	TA Micro.	0.05-0.08	–	1.2	50	[107]
MAPbI ₃	TRPL/TRMC	–	30	4.1	66	[160]
MAPbI ₃	TRPL/TRMC	–	87	29(e^-), 77(h^+)	32 \times 10 ³ (h^+)	[66]
MAPbI ₃	TRMC	–	71	–	–	[161]
MAPbI _{3-x} Cl _x	TRPL/THz	–	27	10.6	–	[160]
MAPbI ₃	TOF	–	$\sim 4 \times 10^{-4}$ (e^- , h^+)	–	–	[97]
MAPbI ₃	TOF	–	6	–	–	[153]
MAPbI ₃	FET	–	0.5	–	–	[103]
MAPbI ₃	Hall	–	8	–	–	[104]
MAPbI _{3-x} Cl _x	EBIC	–	–	1.9, 1.5	–	[117]
MAPbI ₃	SPCM	–	–	12	–	[162]
MAPbI ₃	SPCM	0.13(e^-), 0.07(h^+)	5(e^-), 2.5(h^+)	12(e^-), 13(h^+)	>15 \times 10 ³	Reported Here

studied here. Investigating a range of different film types would shed more light on the preparation route dependency of this observation.

In addition to possible contributions of grain boundaries, the behaviour of trap states in perovskites is of significant interest. An extended tail in transient photocurrent decays attributed to long-lived trap species was reported by Leijtens et al., who estimated charge detrapping times to be ~ 10 μ s.¹⁶³ Such a detrapping time is short enough to contribute to photocurrent measurements presented here, and would lead to an increased photocurrent tail and potentially delay the onset of photocurrent resulting in a reduced apparent charge diffusivity. The number of trap states in polycrystalline perovskite films has been calculated to be $\sim 10^{15}$ – 10^{16} cm⁻³,¹⁶⁴ and Leijtens et al. found a strong excitation dependence of the contribution of the photocurrent tail, with $\sim 50\%$ of photocurrent attributed to the long-lived tail at their lowest investigated excitation density (10^{15} cm⁻³). We expect charge densities to exceed 10^{15} cm⁻³ in the presented measurements, and do not observe a change in behaviour for the lowest excitation

densities investigated here. We therefore expect a limited contribution of detrapping effects, though we are unable to rule them out entirely. Identifying the behaviour of traps is of great interest, and therefore future work should focus on measurements at reduced charge carrier densities. One route forward would be to elongate the excitation spot to a line excitation, allowing for higher currents with lower localized excitation density and further reducing the complexity of physical modelling.

Fundamentally, the diffusivity of electrons/holes ($D_{n,p}$) is related to the effective carrier mass (m^*) and momentum relaxation time (τ) by $D_{n,p} = k_B T \tau_{n,p} / m_{n,p}^*$, where k_B is the Boltzmann constant and T is the carrier temperature. Our measured diffusivity values translate to a ratio τ / m^* that is ~ 2 times larger for electrons than holes. Reports using ultrafast spectroscopy can provide an upper bound for diffusivity values. Values reported for reduced carrier effective mass ($m_e^* = 0.14 m_0$ where m_0 is the free electron mass)¹⁶⁵ and carrier scattering times ($\tau_{n,p} = 80$ fs)¹⁰⁵ predict diffusivities of $25 \text{ cm}^2 \text{ s}^{-1}$ on ultrafast time scales, before phonon scattering and morphology start to play a role. These values are much higher than the diffusivities obtained from our charge transport experiments or from other longer range transport measurements.^{110,117} While mobilities from time-of-flight and field-effect experiments may be affected by slow charge extraction of selective electrodes,¹⁵³ we do not expect these effects to contribute to measurements presented here. Therefore we suggest that, on time scales beyond the nanosecond regime, scattering rates (due to phonons, impurities, grain boundaries, etc.)⁸⁵ increase.

4.6 Conclusion

We introduce a back-contacted device and measurement architecture which enables the transport of electrons and holes to be probed separately. We report electron and hole diffusivities of $D_{electrons} = 0.13 (\pm 0.05) \text{ cm}^2 \text{ s}^{-1}$ and $D_{holes} = 0.07 (\pm 0.03) \text{ cm}^2 \text{ s}^{-1}$, respectively. Our results show that, in our back-contact architecture, charge carriers are capable of long range diffusion and we find diffusion lengths of electrons and holes exceed $12 \mu\text{m}$. While grain boundaries may effect charge transport in the measured devices, we conclude that carriers can cross grain boundaries in the MAPbI₃ films investigated here. Finally, we demonstrate a QIBC device which achieves a short-circuit current density of 18.4 mA cm^{-2} , reaching 70% of the theoretical maximum. Our results demonstrate the potential of perovskite films for device architectures based on lateral charge diffusion, such as back-contact solar cells and LEDs.

Chapter 5

Effects of illumination on perovskite materials and devices

The previous chapter focused on the response of metal-halide perovskite devices to discontinuous, chopped illumination. In the presence of selective electrodes, illumination results in the segregation of photogenerated carriers. Thus *n*-type and, separately, *p*-type regions of perovskite are probed via photoexcitation of perovskite films deposited over different electrode materials. Under operating conditions, solar cells will be subject to continuous illumination both in time and spatially. In this chapter we aim to further investigate the behaviour of devices in operating conditions. We apply a continuous background white light illumination to establish carrier populations. We then perturb the system using a laser probe discontinuous in space and/or time to investigate the behaviour of the system as a result of the perturbation. For measurements in which the number of laser-induced carriers is less than the expected background-induced steady-state carrier density, the extraction length is found to increase dramatically: reaching 25 μm with background illumination. These results reveal important insights into the behaviour of perovskites under illumination, and further highlight the importance of back-contact device architectures both for probing such phenomena and as large-scale solar cell devices.

5.1 Background and motivation

While metal-halide perovskites have been the focus of a great deal of research and development for use in photovoltaic applications, the material's response to illumination remains a very active area of investigation. Questions stretch from the ultra-fast

regime, where reports consider the possibility of an indirect or direct transition,¹⁶⁶ Rashba splitting and the polarization dependence of photoexcitation,⁸⁹ to steady-state conditions where the internal and external quantum efficiencies,¹²³ light-induced passivation⁶⁶ and trap filling,¹⁰² and photo-induced halide migration^{55,56} are discussed. Steady-state effects of illumination on metal-halide perovskite materials are highly relevant to device operation. For solar cells and photodiodes, carrier transport dynamics and recombination directly influence light-harvesting efficiency; while all devices can be affected if the material degrades under illumination.

In Chapter 4, illumination of perovskite thin films over electrode materials results in the development of regions characterised by an excess of one type of charge carrier. To describe this phenomenon in another way, we consider the perovskite film from two perspectives. First, due to the high absorption coefficient of metal-halide perovskites, the thickness of perovskite films for device applications is thin relative to traditional materials such as silicon. At solar irradiance, even at short-circuit conditions, photogenerated carrier densities in operating devices are expected to be on the order of 10^{14} cm^{-3} .¹⁶⁷ Second, the intrinsic carrier density of perovskite materials is relatively low, under 10^{14} cm^{-3} .⁹⁰ Therefore, the densities of photogenerated carriers generated under solar illumination exceed intrinsic concentrations of both electrons and holes. Similarly, in LEDs injected carrier densities exceed intrinsic carrier values. Thus, for back-contact architectures where large regions of perovskite are contacted by selective electrodes, device behaviour is dominated by photo-induced charge density.

We have developed and demonstrated techniques to study the establishment of this carrier population. However, understanding the behaviour of carriers within already established *n*- and *p*-type regions is of direct relevance to the case of carriers generated within an operating solar cell. Here, we present time-resolved photoluminescence and photocurrent measurements of devices in the presence of continuous background illumination. We show that carriers generated in the presence of background illumination have extended lifetimes, and show that extraction lengths extend up to 25 μm in photocurrent measurements.

5.2 Continuous background illumination of vertical devices

In order to investigate the influence of illumination on carrier physics within operating devices, we perform time-resolved photoluminescence (TRPL) measurements on a mixed-cation, vertical “sandwich” perovskite device architecture. The composition of the active layer was $\text{Cs}_{0.06}\text{FA}_{0.79}\text{MA}_{0.15}\text{Pb}(\text{I}_{0.85}\text{Br}_{0.15})_3$, and was prepared and characterised to have a 15% PCE by Mojtaba Abdi-Jalebi. Figure 5.1a describes the investigated device architecture, which is composed of the mixed-cation perovskite infiltrated into a mesoporous TiO_2 electron-selective electrode formed over FTO-coated glass to form the transparent face of the device. Hole extraction is accomplished on the opposite surface of the perovskite layer using spiro-OMeTAD with a gold contact.

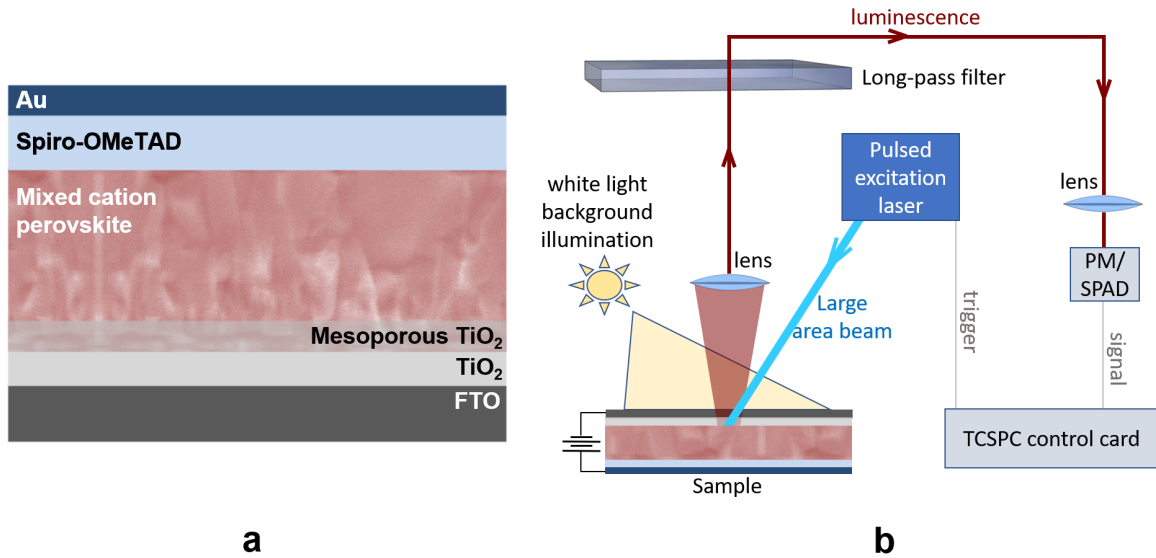


Figure 5.1 a) Schematic of the investigated vertical “sandwich” device architecture, composed of $\text{FTO}/\text{TiO}_2/\text{Cs}_{0.06}\text{FA}_{0.79}\text{MA}_{0.15}\text{Pb}(\text{I}_{0.85}\text{Br}_{0.15})_3/\text{spiro-OMeTAD}/\text{Au}$. a) Schematic of white light background (WLB) TCSPC measurements under applied voltage. The entire pixel is illuminated with continuous white light, while a large area (>1 mm) is illuminated by pulsed laser excitation.

Time-resolved photoluminescence spectra are obtained while varying two other conditions: applied voltage and background continuous wave illumination. For background illumination, the entire pixel of the solar cell was illuminated with truncated white light from a Thorlabs halogen lamp (OSL1). This we term application of white light background (WLB) illumination. A schematic of the setup used is presented in Figure 5.1b. Short pass filters at 665 nm were placed in the white light illumination

path to reduce the amount of light in the range of perovskite emission, and the resulting intensity of continuous background excitation was 0.2 suns. A Keithley 2400 Sourcemeter was used to apply constant voltage to the device during measurements. Background illumination and voltage were applied for at least one minute before TRPL measurements were begun to allow the system to stabilize. We note that this TRPL measurement, in addition to being performed over a large area, is performed at a low laser fluence (407 nm, 5 nJ cm⁻², 100 kHz, ~0.01 suns). Thus each pulse is expected to generate excitation densities of less than 10¹⁵ cm⁻³ in the investigated region.

Figure 5.2 presents the background corrected PL intensity of TRPL measurements measured at forward (red) and reverse (blue) bias, as well as with (light colours) and without (dark colours) background illumination. Each measurement is performed using identical integration times on the same region of the device. All four curves have two similar regions: i) an initial rapid decay in the first 30 ns, followed by ii) a return to a longer-lived decay in luminescence intensity. While each measurement was performed at varying conditions, we observe that background corrected initial photoluminescence intensity (PL₀) is very similar in each case. Indeed, the highest and lowest PL₀ values were obtained at +0.9 V, resulting in 987 and 921 counts at time zero for measurement with and without background illumination, respectively. This variation is less than 8%, and we therefore consider this to indicate that PL₀ is unaffected by background illumination or applied bias.

We link the initial decay of photoluminescence intensity to two factors: charge extraction by electrode materials and charge trapping. Charges generated in the perovskite material may diffuse within the device, and this occurs over the nanosecond timescale. Charges which diffuse to an interface with an extraction electrode may be removed from the perovskite. Additionally, perovskites have been shown to possess trap sites or defects which act to localise charge carriers.^{163,164,168} As photoluminescence is proportional to the density of free charge carriers within the material ($PL \propto bnp$, see Section 2.3), extracting or trapping either electrons or holes will act to reduce photoluminescence intensity. The long-lived decay after ~30 ns can be interpreted as the slowing of these two effects: traps which localise carriers can fill up, and charge extraction of electrode materials will slow as charge builds up at electrode interfaces. We observe that in each measurement, the long-lived decay component settles to similar decay rates. We therefore focus on the changes in photoluminescence intensity observed at early times.

We first consider the result of applied bias on time-resolved photoluminescence measurements. We observe that application of reverse bias leads to a higher rate of decay of PL intensity at early times, and we interpret this to indicate that reverse bias increases the number of charge carriers being extracted by the electrodes. This is expected behaviour as, under reverse bias, the device is operating in the photodetection regime and the applied field is enhancing charge extraction.

Next, we examine the influence of background illumination. In the case of both forward and reverse bias, application of background illumination acts to reduce the rate at which photoluminescence intensity decays at early times. We can interpret this result two ways: the background illumination could generate a steady-state charge carrier distribution which reduces the effects of charge extraction at the electrodes, or the background illumination is filling trap states and therefore reducing the number of laser-induced carriers which are trapped at early times.

Let us further consider the effects of trap filling on presented photoluminescence decays. Let us attempt to quantify the number of trap states which are filled as a result of background illumination assuming a constant level of charge extraction for a given bias. First, we recall that PL intensity is proportional to free charge carrier density ($PL \propto bnp$). It has been argued that trap states near the conduction band are the primary trap mechanism in perovskite films,¹⁶⁴ and therefore we will assume only the electrons are being trapped. We therefore focus on changes in free electron density, and write:

$$\frac{PL_{30ns}}{PL_0} = \frac{bpn_{30ns}}{bpn_0} = \frac{n_{30ns}}{n_0} \quad (5.1)$$

where PL_{30ns} (PL_0) and n_{30ns} (n_0) are the photoluminescence intensity and free electron density at $t = 30$ ns ($t = 0$ ns). We next implement our assumption that charge trapping and charge extraction are the dominant pathways of charge density reduction at early times in the investigated system. We then write:

$$\frac{PL_{30ns}}{PL_0} = \frac{n_0 - n_{trapped} - n_{extracted}}{n_0} \quad (5.2)$$

where $n_{trapped}$ ($n_{extracted}$) is the density of electrons trapped (extracted) after 30 ns. Next, we consider the filling of traps as a result of the application of background illumination. Considering that presented measurements are background corrected, we

write:

$$PL_{BG} = bp(n + n_{BG}) \quad (5.3)$$

where PL_{BG} and n_{BG} are the photoluminescence intensity and steady-state charge density in the presence of background illumination. By removing the background intensity we remove the contribution of n_{BG} . By taking the ratio of photoluminescence intensities as in Equation 5.2, we then write:

$$\frac{PL_{30ns}}{PL_{0,light}} = \frac{n_0 - (n_{trapped} - t_{filled}) - n_{extracted}}{n_0} \quad (5.4)$$

where $PL_{30ns}/PL_{0,light}$ is the ratio of photoluminescence intensities at 30 and 0 ns delay times in the presence of background illumination, and t_{filled} is the number of filled traps in the perovskite. Thus, by taking the difference in PL intensity ratios we arrive at an expression which estimates the density of trap states which are filled by background illumination:

$$\frac{PL_{30ns}}{PL_{0,light}} - \frac{PL_{30ns}}{PL_0} = n_0 t_{filled} \quad (5.5)$$

As n_0 corresponds to the density of carriers at early times, we consider this to be roughly equal to the number of expected carriers generated per pulse, or $3 \times 10^{14} \text{ cm}^{-3}$.

We observe that the ratio PL_{30ns}/PL_0 is different in each measurement condition. At reverse bias, they are 0.03 and 0.01 with and without background illumination, respectively. For forward bias they are 0.07 and 0.02 with and without background illumination, respectively. Comparing reverse and forward bias, we estimate filled trap densities on application of background illumination to be $6 \times 10^{12} \text{ cm}^{-3}$ and $1.5 \times 10^{13} \text{ cm}^{-3}$, respectively. On an uncontacted film with a monomolecular charge lifetime of 1 μs , we would expect 0.2 suns illumination to result in steady-state charge densities on the order of 10^{15} cm^{-3} . That this is higher than our estimation for filled trap density implies that there are either very few traps, that there are large errors in our approximation, or that background illumination additionally influences the kinetics of charge extraction at early times. We argue that introduction of background illumination results in the development of a segregated steady-state charge carrier population, both causing errors in our approximation and changing the kinetics of charge extraction at early times.

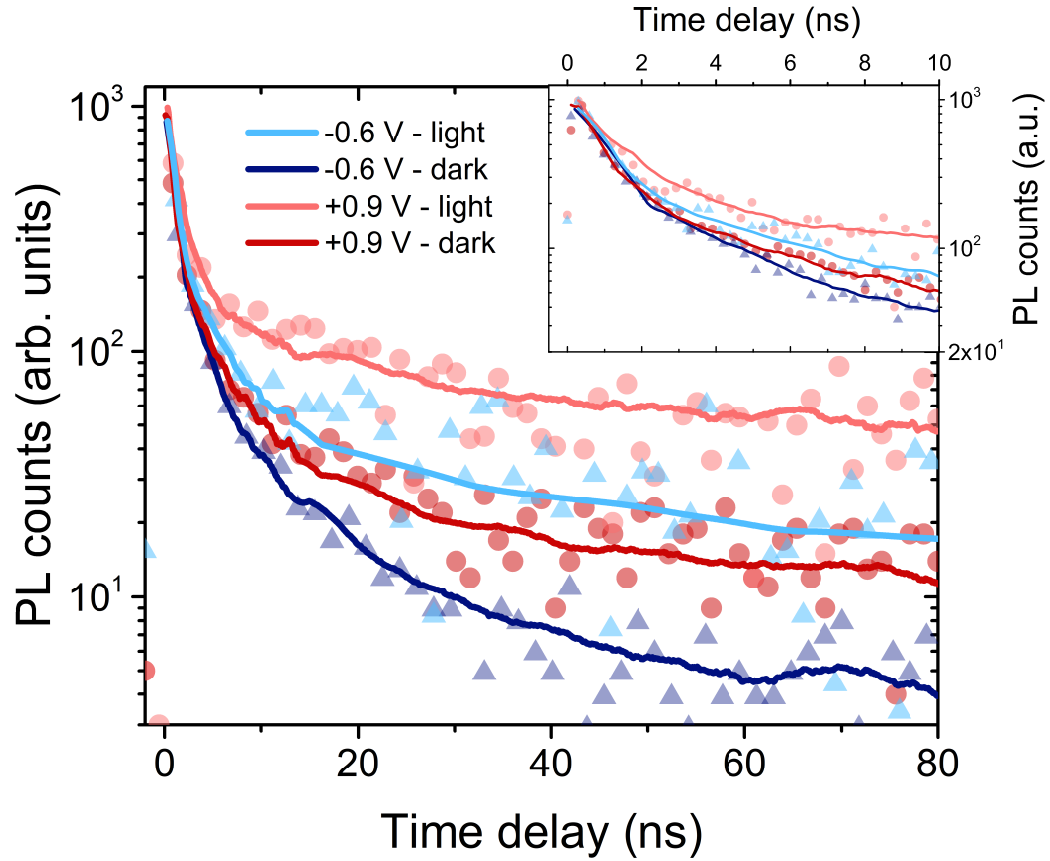


Figure 5.2 Background corrected, time-resolved photoluminescence of a sandwich device with $\text{Cs}_{0.06}\text{FA}_{0.79}\text{MA}_{0.15}\text{Pb}(\text{I}_{0.85}\text{Br}_{0.15})_3$ as the active material collected using time-correlated single photon counting (TCSPC). Blue triangles (with smoothed curves) are collected at a reverse bias of 0.6 V, while the red circles (with smoothed curves) are collected at a forward bias of 0.9 V. Each measurement is performed for the same integration time, and no normalisation is performed. Background corrected initial photoluminescence intensity is very similar in each measurement, with PL_0 variation under 8% between measurement conditions. Each curve shows two regions: an initial rapid decay in the first 30 ns, followed by a return to a longer-lived decay in luminescence intensity. Application of reverse bias increases the decay rate of photoluminescence at early times, as expected. Light curves are collected with the addition of a constant background illumination of roughly 0.2 suns of white light. The drop in photoluminescence intensity at early times is reduced upon exposure to constant background light in each case. Photoluminescence decay rates reduce after ~ 30 ns to similar levels in each measurement condition. Measurements were performed with 407 nm laser excitation fluences of 5 nJ cm^{-2} at a repetition rate of 0.1 MHz. The inset shows data collected at early times.

Here, we summarise the implications of presented TRPL measurements. First, we consider the influence of the electrodes. Extraction materials in this high performing device are contributing to the photoluminescence behaviour at early times, with changes in PL kinetics upon changes in applied bias. Furthermore, the addition of background illumination decreases the decay in PL intensity at early times, and we expect trap filling to contribute to this observed behaviour. We estimate the number of filled traps, and find that the filled trap density is higher under reverse bias conditions. This is expected behaviour as the density of charge carriers will certainly be reduced in the case of reverse bias conditions, therefore reducing the number of carriers available to fill trap states. The very low densities of filled states implies that steady-state charge densities on our contacted device are quite low, or that the addition of background illumination impacts the kinetics of charge extraction. The precise nature of this potential effect on extraction at the electrode, such as any field effects as a result of charge accumulation due to background illumination, are difficult to probe in this architecture. Indeed, the vertical architecture investigated in these measurements is complicated by the presence of both electron- and hole-extracting layers at the point of illumination.

5.3 Effects of background illumination on back-contact devices

In order to isolate the behaviour of carrier populations of one type under the influence of background illumination, we return to the back-contact architecture introduced in Chapter 4. In Figure 5.3a, a schematic of the measurement is presented. A focused laser spot ($\sim 1.5 \mu\text{m}$ diameter) photogenerates charges in a perovskite film a certain distance from the junction of NiO_x and SnO_x . Generated electrons are removed by the electron-selective electrode SnO_x . Concurrently, the entire device is illuminated by 0.2 suns of background illumination, which generates an equilibrium population of charge carriers within the perovskite (grey sloping curve). Blue curves represent the growth of the photogenerated hole population within the perovskite active layer, which develops until generation and charge diffusion balance charge extraction and recombination.

Figure 5.3b further details the temporal aspect of the measurement. The background illumination will create a constant photocurrent, on top of which the focused, pulsed illumination will generate intermittent photocurrent. By monitoring photoluminescence

and photocurrent phase and amplitude while varying the excitation—junction distance, the effect of the background illumination on charge carriers is monitored.

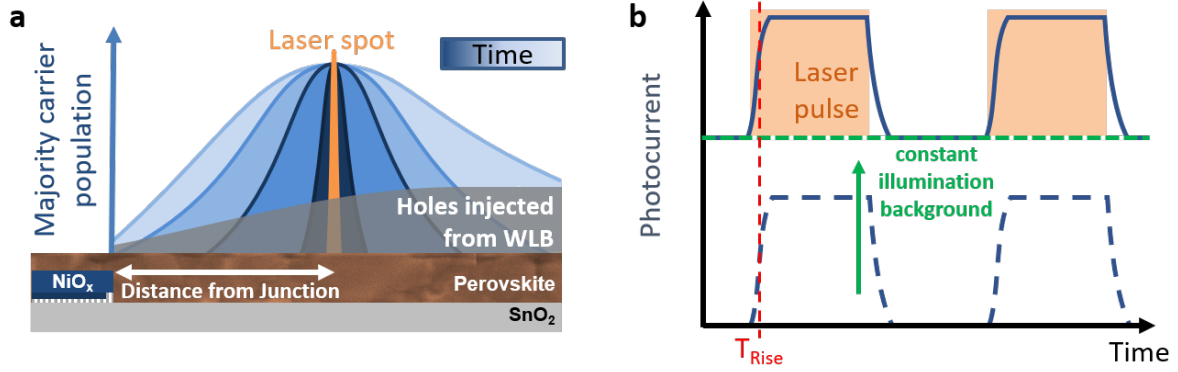


Figure 5.3 a) Schematic of the measurement conditions, in which illumination occurs at varying distance from the junction between two planes of continuous selective electrodes. In addition, a population of charge carriers resulting from constant white light background (WLB) illumination are presented in grey. Blue curves show the normalised majority carrier distributions at varying times from the beginning of laser illumination to the establishment of an equilibrium with recombination and extraction. (b) Evolution of photocurrent with time, with the equilibrium charge distribution shown along with the characteristic photocurrent rise time T_{Rise} , which is calculated from the phase offset measured by a lock-in amplifier (the orange area represents illumination time). The carriers injected from constant white light background are expected to raise the background carrier concentration uniformly, while the modulation is resolved over the constant background current.

To investigate the influence of background illumination on photoluminescence, Figure 5.4 compares photoluminescence intensity of a MAPbI_3 device with (red circles) and without (grey circles) background illumination. The focused laser excitation is rastered from the electrode junction to a distance $100\ \mu\text{m}$ away from the junction over a region of perovskite deposited on the electron extracting material SnO_x . The measurement is conducted over the same region, as evidenced by the identical trend in photoluminescence intensity moving away from the electrode junction. The presence of background illumination increases the overall luminescence intensity of the perovskite film (example obtained spectra in inset). This behaviour agrees with the results of time-resolved measurements on vertical devices in Figure 5.2, where overall photoluminescence intensity increased as a result of background illumination.

The near doubling of photoluminescence efficiency upon introduction of background illumination, however, is quite surprising. We expect 0.2 suns of background illumination to result in a steady-state carrier density of $10^{15}\ \text{cm}^{-3}$, while laser-induced populations at the point of excitation are expected to be much higher, roughly $\sim 10^{17}\ \text{cm}^{-3}$.

Considering the case of only one charge species being trapped within the perovskite film, background illumination would need to fill traps to a density similar to the dominant laser-induced carrier density. As the background-induced carrier density is too low to accomplish this, we consider this strong evidence of suppression of electrode-induced charge segregation effects upon introduction of background illumination. We postulate that such effects appear more strongly in this measurement condition, relative to measurement of vertical “sandwich” devices, as illumination of the perovskite away from the electrode junction will result in the build up of at least one carrier type. The influence of background illumination on transport behaviour is of great interest in contacted films, as these conditions are directly relevant to device operation.

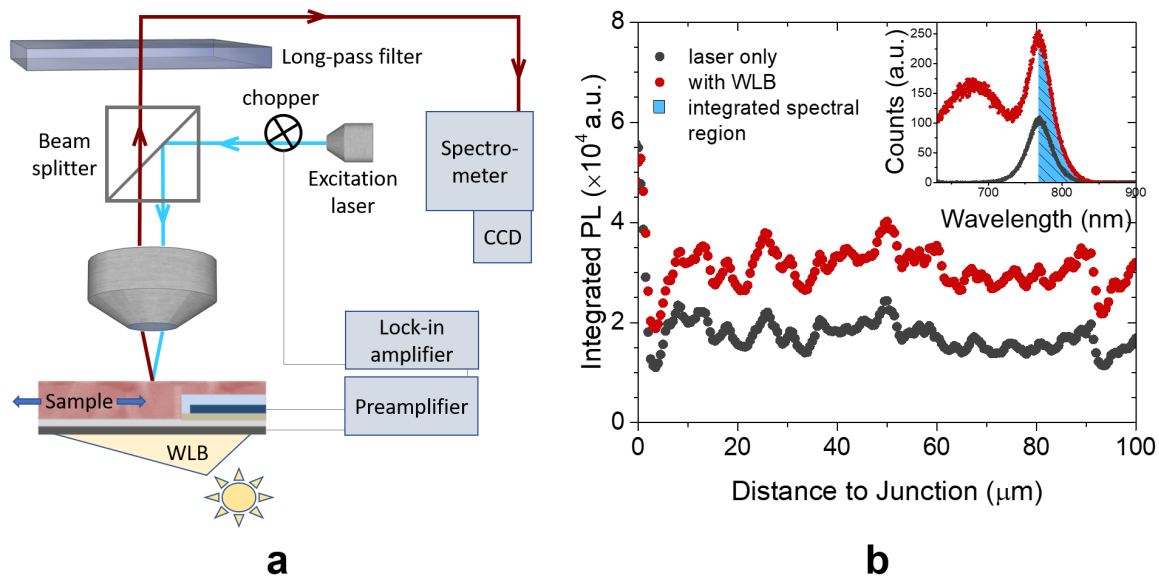


Figure 5.4 a) Schematic of SPCM measurement accomplished with white light background (WLB) illumination. b) Integrated photoluminescence intensity vs distance to the electrode junction of MAPbI₃ deposited over SnO_x. The grey curve is the number of counts accumulated as the result of laser-excitation only, while the red curve is the number of counts accumulated with the addition of white light background illumination equivalent to 0.2 suns. The region integrated is from 768 nm to 850 nm, which is highlighted in blue in an example spectra in the subset figure. Photoluminescence intensity is found to nearly double as the result of the addition of background illumination. Photoluminescence intensity is found to be higher over the NiO_x electrode, similar to results in Chapter 4. Measurements were taken with an average laser intensity of 5.6 W cm⁻², or ~80 suns.

To investigate how far charges travel in background illumination conditions, photocurrent amplitude is measured at varying distances between the excitation spot and the NiO_x—SnO_x junction (Figure 5.5a). In both the case of background illumination (red

circles), and no background illumination (black circles), the measured photocurrent follows an exponential decay with increasing excitation—junction distance.

We observe that the general trend for photocurrent decay does not change upon introduction of background illumination, indicating that monomolecular recombination remains the dominant form of recombination within our system. In Chapter 4 we explain that the electron and hole carrier diffusion lengths of this device are accessible via photocurrent measurements, due to the lack of field within the plane of the device under short-circuit conditions. In the case of background illumination, however, we expect the development of a gradient of hole density towards the electrode junction (as represented in the sketch in Figure 5.3a). We expect this to be caused by the increased chance of charge extraction for carriers generated by background illumination within a diffusion length of the electrode junction. As a result, we change our terminology to describe the length scale of charge extraction as the extraction length, the length over which photocurrent amplitude decays by a factor e . Thus, we attempt to characterise the marginal chance a photogenerated carrier will contribute to photocurrent at varying excitation—junction separation.

Comparing photocurrent obtained with and without background illumination, we observe that the presence of background illumination reduces the obtained amplitude of photocurrent signal at the junction. This could be the result of two factors. First, and most simply, background illumination could be increasing recombination resulting in a lower photocurrent. Second, the presence of an extended tail of photocurrent could reduce the observed photocurrent amplitude as measured by the lock-in amplifier (as presented in Figure 4.4).

Let us first consider origins of increased recombination. Slowing of charge extraction would be one means of increasing recombination, as carriers would spend more time within the perovskite material. We have suggested that background illumination results in charge accumulation of one type. Such charge collection could result in fields across the electrode which reduce charge extraction at high accumulated charge densities. Charge accumulation is expected to be maximised away from the electrode junction, particularly in short-circuit conditions, as both carriers can be removed at the junction. Therefore we would expect to see reduced photocurrent relative to the laser-only case especially towards the electrode junction, which is the opposite of observed behaviour. Therefore charge accumulation is not expected to reduce photocurrent amplitude in this case.

Another possible means of screening fields exists in perovskites, however. Numerous reports have shown light-induced ion migration in perovskite films,^{55,64,169,170} and exposure of the system to background illumination is likely to lead to ion migration. Each measurement takes ~ 40 minutes, throughout which injected carrier densities will induce a field toward the electrode junction, and ions will be capable of motion. We therefore cannot rule out the possibility that ions screen fields within the device, slowing charge extraction and increasing recombination relative to measurement without background illumination.

The other possible explanation of reduced photocurrent amplitude considered was the enhancement of a long-lived photocurrent tail. Long lived tails of photocurrent have been reported previously, with lifetimes up to 8 μs reported by Leijtens et al.¹⁶³ In addition, time-resolved PL results presented in Figure 5.2 show that introduction of background illumination increases the number of free charge carriers remaining after initial excitation. Both results, however, indicate that carriers persist for timescales far below those encountered in presented photocurrent measurements, where laser pulses are separated by ~ 1 ms. We presented, however, a frequency dependence of photocurrent measurements in Figure 4.4, and suggested this may be the result of such a long-lived tail. We therefore cannot exclude the influence of such effects on presented measurements.

Interestingly, the decay of photocurrent with increasing distance is reduced upon the introduction of background illumination. This indicates that regardless of the origin of reduced photocurrent magnitude towards the electrode junction, background illumination improves long-range transport. We will return to discuss this further in the next section.

In addition to photocurrent amplitude, we investigate the influence of background illumination on the temporal evolution of photocurrent rise time versus distance (Figure 5.5b). In both cases the rise time increases linearly with distance, as expected. The addition of background illumination, however, increases the speed of photocurrent onset. This indicates that in the presence of photogenerated carriers, steady-state conditions are reached more quickly. This could be the result of an increase in carrier diffusivity, or a reduction in pathways which prevent carriers from being collected such as charge trapping. Decreased rates in the fundamental scattering mechanisms, such as impurity scattering or scattering at grain boundaries,⁸⁵ would increase diffusivity. At the same time, filling traps in the system would decrease the time to equilibrium conditions as fewer injected carriers at early times would be captured by trap states.

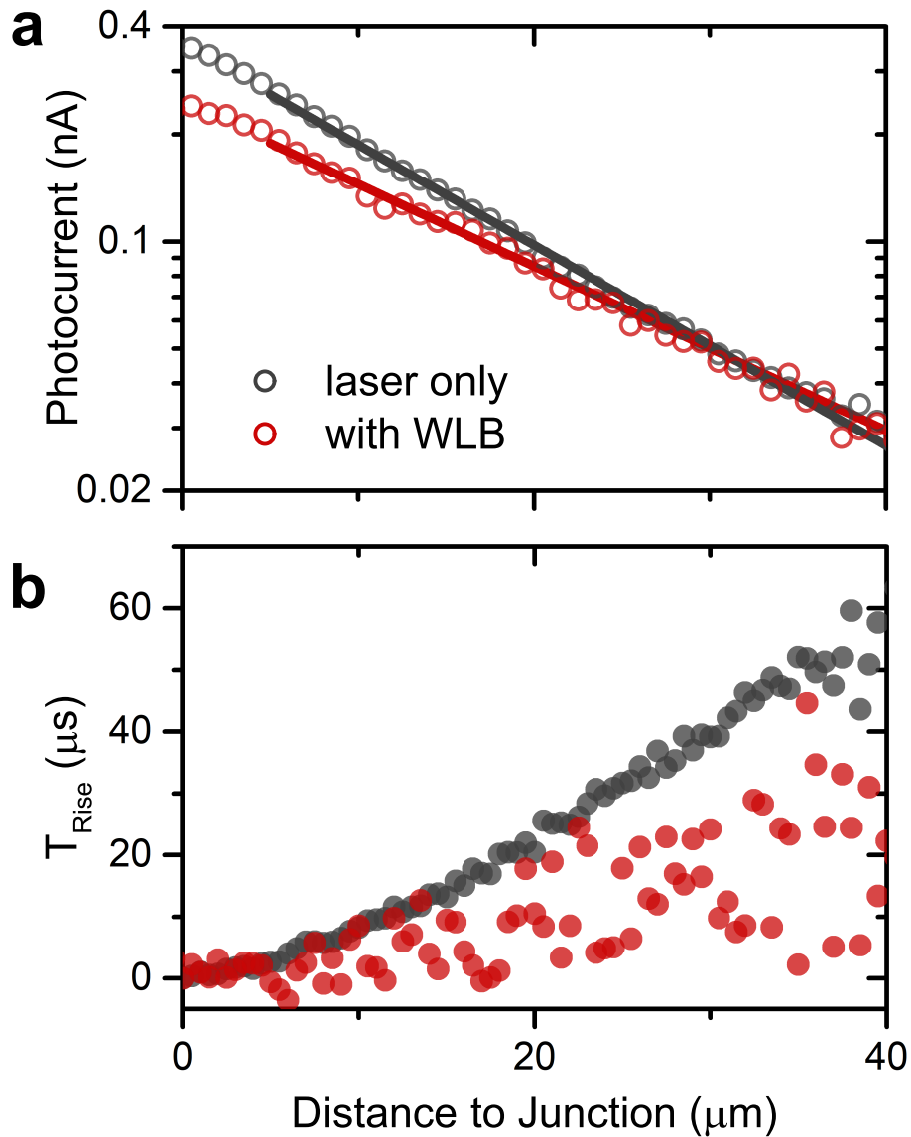


Figure 5.5 a) Photocurrent amplitude measured at varying distance from the electrode junction. The grey curve is with laser excitation only, while the red curve is with the addition of a white light background. In both cases photocurrent decays exponentially with distance to the electrode junction. The addition of white light background reduces the photocurrent signal at short distances, but reduces the rate of photocurrent decay with distance. b) Photocurrent rise time at varying distance from the electrode junction. The linear relationship of rise time and excitation—junction distance is retained, and the apparent rise time in the case of background illumination is shorter than that without WLB which indicates faster charge motion. The laser wavelength and intensity was 405 nm and 5.6 W cm^{-2} , respectively. Scans were performed over a $5 \times 170 \mu\text{m}$ with sampling points every 500 nm with 200 ms integration time.

The addition of background illumination increases charge density, but we expect carrier densities to be dominated by the high laser-induced carrier concentration, therefore we do not anticipate any effects on charge-charge scattering rates. In the case of grain boundaries, background charge densities could have an effect on any energetic barriers or traps which are localised at grain boundaries. In polycrystalline silicon, it has been shown that energetic barriers to charge carrier motion across grain boundaries are heavily excitation density-dependent.⁴¹ In addition, trap states, regardless of location, would be filled upon exposure to background illumination. From this data alone we are unable to identify the origin of improved apparent charge transport. Indeed, the addition of background illumination increases the noise of photocurrent phase significantly, possibly due to fluctuations in lamp intensity or incoherent detrapping of charge carriers; but the precise origin of the increased noise is not readily apparent.

5.4 Effects of background illumination on charge transport

In the previous section we discussed the impact of background illumination on photocurrent measurements at one laser intensity. Here, we probe the influence of the illumination intensity on photocurrent amplitude. Figure 5.6a displays the absolute photocurrent obtained at excitation—junction distances of 40 μm for varying laser intensities with (red circles) and without (black circles) background illumination. All measurements were performed with background illumination of 0.2 suns. Without background illumination, photocurrent follows a linear dependence upon laser intensity. At high power densities, photocurrent in the presence of background illumination matches photocurrent without background illumination. Interestingly, as laser intensity is reduced, the absolute photocurrent obtained with background illumination is increased relative to results without background illumination.

To further examine the improvement in photocurrent collection at low laser-induced carrier concentrations, the extraction length is plotted against laser intensity in Figure 5.6b. Similar to the case of photocurrent amplitude, at high power densities the extraction length obtained with (red circles) and without (black circles) background illumination is similar. At low laser intensities, however, the extraction length increases sharply in the case of background illumination. This indicates that as the intensity of the laser is reduced, the chance that carriers photogenerated further from the electrode

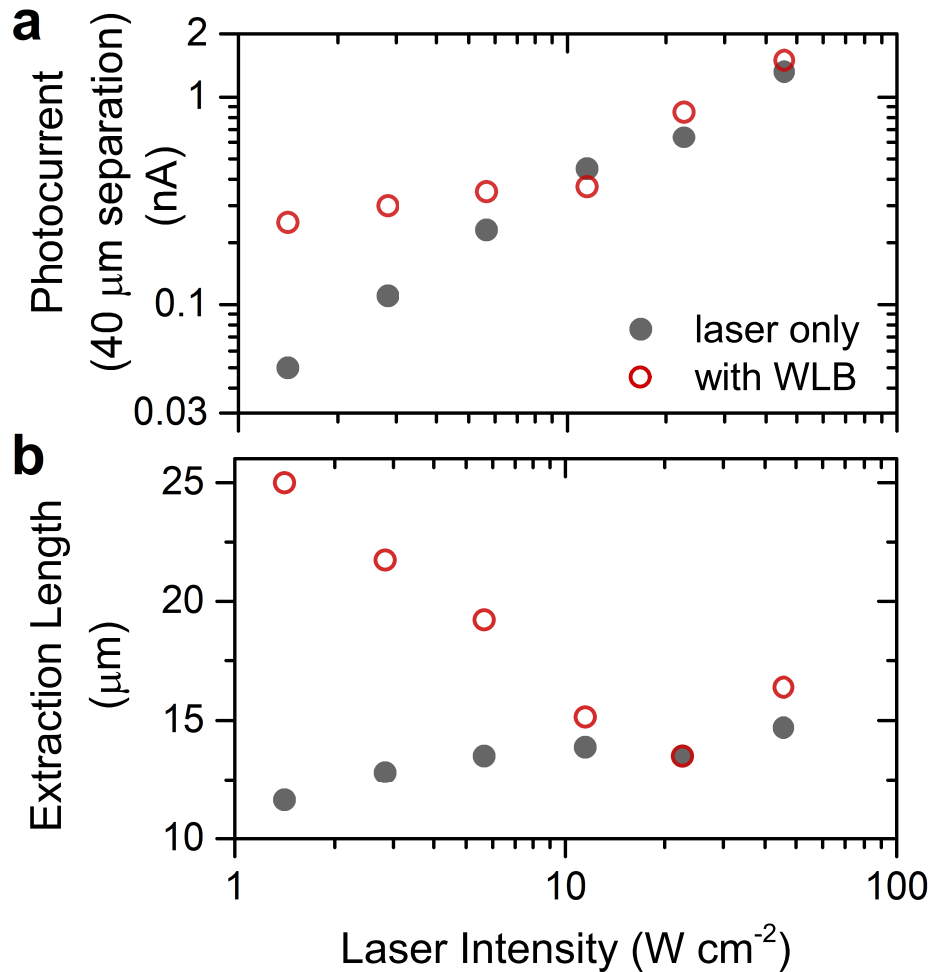


Figure 5.6 a) Photocurrent measured at an electrode-excitation separation of 40 μm versus laser intensity. Grey circles are obtained in measurements with laser illumination only, while open red circles are measured with the addition of a white light background. Measured currents in each case are similar at high laser intensities. As the intensity of the laser is reduced, however, the current obtained in the case of illumination in the presence of a white light background is increased significantly. b) Extraction length vs laser intensity. Dark circles are diffusion lengths extracted from photocurrent decays in the case of laser-only illumination. Red, open circles are the exponential decay rate with distance for measurements in the presence of white light background illumination. As we expect the formation of a substantially non-uniform charge population in the presence of white light illumination, we do not propose that this distance correlates directly to a diffusion length under the influence of background illumination. At high laser intensities, the extraction length in each measurement is found to roughly converge. At low laser intensities, however, the extraction length in the case of injection in the presence of WLB improves significantly, reaching 25 μm at the lowest-investigated laser intensity.

junction will contribute to photocurrent increases. It appears that we have two modes of operation. At high laser intensities, the number of carriers in the system is dominated by the number of carriers injected by the laser, and the effect of background illumination is not identifiable. At low injection densities, the laser is a small perturbation of the carrier population established by the background illumination. Thus, at high laser intensities the laser-induced carriers are dominant and the system appears to behave as described in Chapter 4. At low laser intensities, however, we are able to probe the result of adding small quantities of carriers to the already-established steady-state condition. Thus, we have developed a technique to probe the physics of these dynamic, photo-generated n - and p -type carrier populations. Here we probe the behaviour of a steady-state photogenerated hole population over SnO_x . We observe that for small perturbations of the carrier population, the distance over which carriers can travel to contribute to photocurrent increases to 25 μm , a remarkably large distance for a solution-processed polycrystalline material. We will discuss implications of this result further in the next section.

5.5 Influence of charge density and discussion

In order to examine our hypothesis that our measurements probe two regimes of device operation, we compare predicted photogenerated carrier densities for each laser intensity to that expected in the case of white light background illumination (Figure 5.7). We predict the carrier density resulting from various laser powers using the diffusivities and recombination rates found in Chapter 4. Furthermore, we apply the one-dimensionalised model in Ref. [156] which assumes only monomolecular recombination and predicted that carrier populations decay with distance from a point excitation as a Bessel function of the first order (coloured circles). These laser-induced carrier densities are compared to the predicted steady-state carrier density as a result of 0.2 suns illumination (dashed black line). We observe that, for the three higher laser powers (11, 23, and 45 W cm^{-2}), the number of carriers expected to diffuse 40 μm from the point of excitation is expected to exceed the number of carriers induced by a background illumination level of 0.2 suns. This is in agreement with results presented in Figure 5.6a, where photocurrent magnitude is the same with and without background illumination at these laser intensities.

For low laser powers (1.4, 2.8, and 5.6 W cm^{-2}), we observe that expected steady-state carrier concentration as a result of laser illumination is less than the background

illumination-induced carrier concentration. Again, this is in agreement with Figure 5.6b, where it was found that at low laser-induced carrier densities the introduction of background illumination significantly altered the trend in photocurrent decay with excitation density. These results further support our proposal that our low laser intensity measurements probe the behaviour of carriers within the photogenerated steady-state *p*-type perovskite.

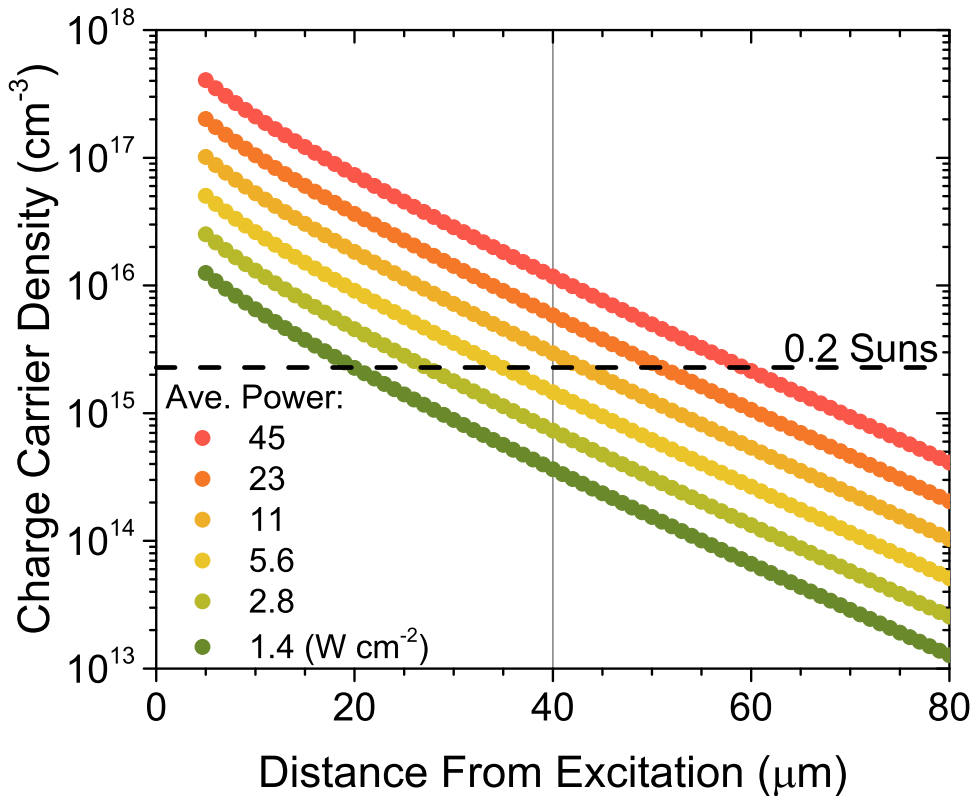


Figure 5.7 Simulated carrier densities versus distance from excitation point for each investigated illumination condition. Each curve follows a Bessel k function of the first order, as predicted by Lamboll et al.¹⁵⁶ The expected carrier density resulting from illumination of 0.2 suns is presented by the dashed black curve. Interestingly, the laser-induced carrier concentration is predicted to be less than the background-induced carrier concentration at 40 μm separation for the lower levels of laser-induced illumination. These are the same conditions which exhibit improvements in carrier extraction lengths and photocurrent values in Figure 5.6.

As mentioned previously, the impact of ion migration on photocurrent measurements in the presence of background illumination cannot be ruled out. In this case, however, we do not expect a significant variation in the impact of ion migration between

measurements with background illumination. Minutes pass between each laser raster, with each raster exposing film volumes to laser illumination for ~ 1 s. In addition, background illumination intensity is identical in each presented illumination condition. Therefore we do not expect ion migration to contribute significantly to changes in photocurrent amplitude or charge transport between measurements with background illumination.

Trap filling effects, however, are likely to contribute to presented measurements. As discussed previously, introduction of background illumination will result in filling of trap states. One possible interpretation of the results presented in Figure 5.6 is that, at high laser-induced carrier densities, all traps can be filled by the laser excitation, leading to similar behaviour with and without background illumination. For low laser intensities, however, laser-induced carrier densities are reduced. In the presence of background illumination, traps are filled, allowing laser-induced charges to travel further and therefore resulting in improved photocurrents and extraction lengths. If traps are filled, then the injected carrier density must be equal or greater than the number of traps present in the film. Observing the predicted steady-state density from Figure 5.7, the trap density implied by photocurrent results is $\leq 10^{15} \text{ cm}^{-3}$. In this interpretation, at low laser intensities the motion of charge carriers in the absence of trap states is investigated, and resulting diffusion and extraction lengths would increase, matching observed photocurrent trends. Estimated trap densities of 10^{15} cm^{-3} fall within the range reported for polycrystalline perovskite films.¹⁶⁴ We contrast this with estimated filled trap densities in TRPL results measured on $\text{Cs}_{0.06}\text{FA}_{0.79}\text{MA}_{0.15}\text{Pb}(\text{I}_{0.85}\text{Br}_{0.15})_3$ devices presented in Section 5.2. Lower trap densities could be the result of the addition of Cs and Br, which have been proposed to passivate trap states in thin films.^{171,172} We postulate, however, that other photo-induced effects on charge extraction reduce estimated densities of filled traps. Thus, we consider trap density estimations in photocurrent measurements to be more accurate than the estimated filled trap densities presented in Section 5.2.

Similar to traps, grain boundaries can have highly excitation-dependent influences on charge transport.⁴¹ The impact of grain boundaries on transport in perovskite films remains unclear, though some reports have postulated that they may be sites of trap states or charge-accumulation.^{173,174} If grain boundaries act to introduce trap states to perovskite films, then their impact would be tied up into discussions of carrier trapping in the previous paragraph. If grain boundaries presented energetic barriers for charge transport, then at a certain density of charge carriers this potential barrier would

flatten out and barriers to inter-grain transport would be removed. The removal of such a barrier, however, should result in relatively increased photocurrent amplitudes at overall higher excitation densities. Instead, we see that introduction of background illumination improve extraction as we lower laser-excitation density, we wherefore do not attribute observed trends to potential barriers at grain boundaries.

One weakness of the trap-filling interpretation of presented results is that extraction lengths do not also improve for high densities of laser-induced charge carriers. If filling of trap states is entirely responsible for improved transport parameters, then transport parameters at high laser intensities would match the improved parameters seen upon introduction of background illumination at low laser intensities. We therefore consider there to be two possible explanations of observed behaviour. First, the trap filling effect dominates transport measurements here, and the reduced transport lengths found at high laser intensities are the result of increased radiative (or possibly Auger) recombination. Second, charge segregation dominates, and the transport of carriers is improved through the development of segregated charge carrier populations. In this interpretation, high laser-induced carrier densities overwhelm background populations screening any improvement. At low laser-induced carrier densities, however, the transport parameters of the background carrier population is probed, and found to be significantly improved. To determine the root cause of improved transport with background illumination, measurements at varying background illumination intensities should be performed.

Presented results demonstrate measurement techniques to probe the behaviour of charge populations in full PV devices, under conditions approaching operating conditions. The increase in photocurrent at large excitation—junction distances upon application of background illumination at low laser intensities shows that the effective transport length of steady-state charge populations is improved upon application of background illumination. We have discussed how this is could be the result of trap filling or the superior transport parameters of segregated charge populations. Using the presented measurement techniques to investigate varying illumination conditions, electrode materials, and perovskite compositions would be a means of identifying the origins, and means of optimizing, charge transport parameters under operating conditions.

Improvements in charge transport behaviour upon introduction of background illumination could contribute to the observed improvement in device performance at early times as a result of light soaking.¹⁷⁵ Light soaking effects which occur on the

seconds timescale would not be explained by the mechanisms proposed to describe presented results, however, and are likely the result of another, slower process such as ion or defect migration.

Regardless of origin, identifying the limits of device improvement upon exposure to background illumination will determine ideal operating conditions for back-contact cells. Quantifying the extraction lengths for varying background steady-state concentrations would reveal the intensity-dependence of device performance and allow for optimisation of device geometries.

5.6 Conclusion

Here we show that continuous illumination results in the development of segregated charge populations in both vertical and sandwich perovskite architectures, and we introduce means of probing the behaviour of such charge populations at operating conditions. We investigate time-resolved luminescence and transport properties, and find that charge transport properties increase as a result of background illumination. Indeed, we show that charge extraction lengths reach 25 μm at low laser-induced charge densities. We suggest that trap filling, and possibly segregation of carrier populations plays a role in improving transport characteristics, and outline means of estimating trap densities using our measurements. Our results have profound implications for device operation, and demonstrate that vertical architectures likely benefit from the effects of charge segregation via electrode materials demonstrated in Chapter 4 on back-contact devices.

Chapter 6

Recombination in polycrystalline perovskite films and devices

In Chapter 4 we reported extended diffusion lengths within operating polycrystalline perovskite devices. The rate of diffusion of carriers was found to be within the range of previously reported diffusivities. We therefore report that recombination in our architecture, which we propose produces a large excess of one carrier type upon photoexcitation, is strongly suppressed. Resulting recombination velocities are below 2 cm s^{-1} , approaching values of high quality silicon¹²⁴ and an order of magnitude lower than under standard bipolar conditions.¹⁵⁸ To understand the low recombination observed in measured devices, we more closely examine the origins of recombination via photoluminescence measurements. We demonstrate that charge carrier segregation can cause photoluminescence quenching under steady-state conditions, and present a model to describe the behaviour of back-contact devices during photocurrent measurements.

This chapter is based on PL measurements and modelling in Ref. [149].

6.1 Background and motivation

nonradiative recombination of charge carriers negatively impacts photovoltaic device performance in two ways: it lowers the operating and open-circuit voltages¹⁷⁶ and it reduces the number of carriers available for extraction. Most perovskite solar cell development has focused on vertical “sandwich” architectures, while the highest-performing silicon technologies are based on back-contact architectures.⁶ Back-contact architectures rely on efficient lateral transport of photogenerated carriers across the absorber layer to alternating hole and electron selective contacts distributed on the

rear side of the device. Low recombination and high diffusivities in crystalline silicon allow for electrodes as wide as 1 mm,¹⁷⁷ while grain boundaries in poly-crystalline materials can present obstacles for efficient charge diffusion and therefore require shorter spacings.⁶⁸ Studies on single crystal lead-halide perovskites suggest that charge diffusion lengths can exceed 30 μm .⁸³ Recent reports suggest that such diffusion lengths and carrier lifetimes in polycrystalline films are obtainable owing to the effect of improved passivation techniques,⁶⁶ further enhanced by photon recycling.^{112,178} These results raise the prospect of achieving efficient perovskite-based back-contact devices. Back-contact architectures remove the requirement for a transparent top electrode, providing two potential benefits: higher currents due to improved light trapping and more flexibility in processing and passivation treatments.

Here we probe the origins of the reduced recombination velocities observed in transport measurements (Chapter 4). Our back-contact architecture employs charge-selective electrodes to isolate electron and hole populations. We investigate the influence of this charge segregation on recombination via photoluminescence measurements and one-dimensional modelling. From photoluminescence measurements, we find that charge segregation over the electron-selective electrode, SnO_x , is more profound than that over NiO_x . Furthermore, we show that photoluminescence quenching in the investigated architecture is driven by charge segregation, and not dominated by nonradiative recombination. Finally, we develop a model which describes photocurrent measurements, and find that charge carriers move across investigated electrode junctions with unexpectedly low losses.

6.2 Probing recombination in operating back-contact devices

In order to examine the origins of recombination within investigated MAPbI_3 devices presented in Chapter 4, we first examine the spatial variation of photoluminescence of the back-contact device. In Figure 4.1d, we presented measurements of the variation in photoluminescence intensity over the active region of a quasi-interdigitated back-contact (QIBC) device. Figure 6.1 expands upon these measurements, showing spectral and temporal dependence of luminescence as measured using confocal photoluminescence microscopy.

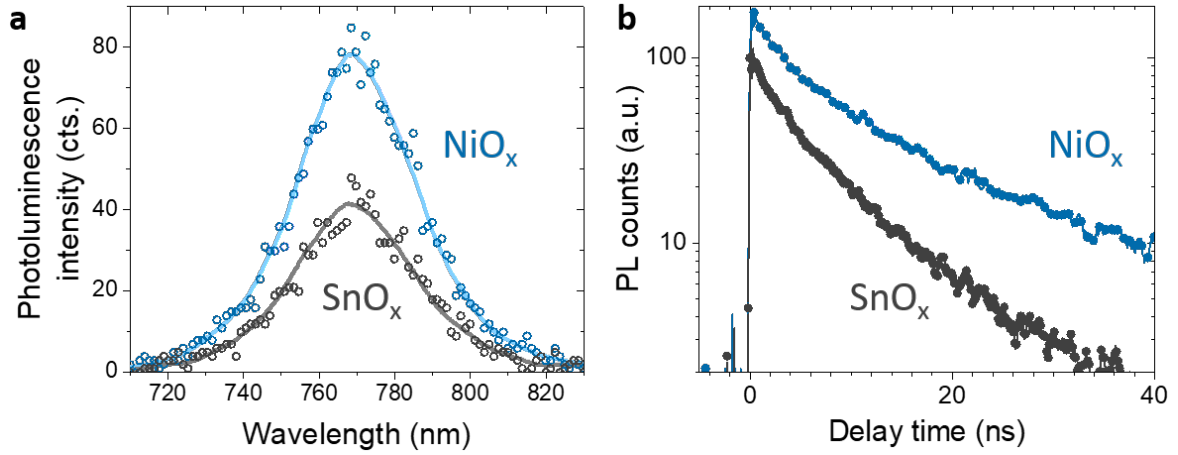


Figure 6.1 (a) Comparison of typical photoluminescence spectra obtained during scanning photocurrent and photoluminescence measurements of QIBC devices: excitation of MAPbI₃ deposited over the electron-conducting layer SnO_x (grey circles) versus emission of MAPbI₃ deposited over the hole-conducting layer NiO_x (blue circles). Measurements were obtained using a 405 nm excitation with intensities of 5.6 W cm² on a spot size of 1.5 μm, running through a chopper wheel at 800 Hz and a 50:50 duty cycle. (b) Comparison of time-resolved photoluminescence results for the device active region. Excitation was achieved using 450 nm pulsed illumination at 5 MHz with fluences of 2.8 μJ cm⁻² per pulse.

Figure 6.1a provides example spectra obtained in photoluminescence scans of the active area of a device, comparing the emission resulting from excitation of MAPbI₃ deposited over the electron-conducting layer SnO_x (grey circles) to the emission of MAPbI₃ deposited over the hole-conducting layer NiO_x (blue circles). Peak wavelength, spectral breadth, and spectral shape are the same in both cases, with emission centred at 768 nm. Emission over NiO_x is found to be higher in intensity, however, than emission over SnO_x.

The consistency in the shape and position of emission spectra implies that the buried electrode material is not changing the nature of emissive species of the MAPbI₃ film. This is expected, as we expect the pathways of charge carrier recombination within the MAPbI₃ to be unaffected by buried electrode materials. The change in the intensity of emission could be the result of several factors. First, the NiO_x electrode has a solid Ni core, which should result in a higher reflectivity for the NiO_x contact. We clarify that the SnO_x contact is composed entirely of transparent materials. This increase in back-reflection could result in higher levels of photoexcitation over the NiO_x electrode. Second, deposition over different electrodes could result in different levels of surface trap densities. This could have two possible effects: a higher density of nonradiative traps over SnO_x could potentially reduce the photoluminescence efficiency

relative to NiO_x , or NiO_x could be inducing a radiative recombination pathway which increases the fraction of carriers which recombine radiatively via formation of emissive trap states. While normally trap states are thought of as nonradiative in perovskite systems, radiative trap states have been reported in perovskite nanocrystal systems.¹⁷⁹ Third, electrode materials are deposited to facilitate the selective removal of one type of charge carrier. This will result in charge segregation, one species of charge carrier will be preferentially removed from the perovskite film while the other species remains. A difference in charge segregation behaviour between SnO_x and NiO_x (e.g. difference in segregation rate and/or level of segregation) would affect radiative efficiencies.

We first consider the potential influence of trap states. The presented measurements are performed at high excitation densities ($>10^{16} \text{ cm}^{-3}$), and therefore it is unlikely that nonradiative trap states remain unfilled over either electrode. More importantly, such a high density of nonradiative trap states would be expected to significantly impact short-circuit current, which is high in the investigated system. A similar argument may be made to rule out the influence of radiative trap states. In addition, significant contribution of radiative trap states would be expected to change the wavelength of emitted light. Therefore we consider it unlikely that trap states contribute significantly to the differences in photoluminescence behaviour presented in Figure 6.1a. The influences of charge segregation and level of absorption are better probed by time-resolved measurements.

To further compare the variation in photoluminescence behaviour over the active area of devices, time-resolved photoluminescence measurements are performed (Figure 6.1b). Time-resolved PL is accomplished here via confocal PL microscopy on MAPbI_3 deposited over the electron-conducting layer SnO_x (grey circles) and MAPbI_3 deposited over the hole-conducting layer NiO_x (blue circles). Here, we observe that the initial photoluminescence intensity (PL_0) is higher in the case of excitation over NiO_x . This could arise from two possible effects: a higher rate of generation over the NiO_x due to the higher reflectivity of the substrate, or significantly more quenching at early times over SnO_x below the resolution limit of the presented experiment. While quenching at such early times cannot be entirely ruled out, a diffusivity as high as $1 \text{ cm}^2 \text{ s}^{-1}$ would result in a diffusion velocity of $\sim 300 \text{ nm ns}^{-1}$. This indicates that quenching would occur on the nanosecond scale, and therefore should occur over timescales observable in the presented experiment. We therefore conclude that reflectivity of the buried electrode affects absorbed charge density in the different regions of the device. Beyond the initial period of emission, however, it is observed that there is a difference in

radiative behaviour between the two regions. As the initial PL intensities are only separated by a factor of two, we expect the injected charge densities to be within roughly a factor two of each other, therefore we consider it unlikely that changes in recombination kinetics can be described only by differences in the number of carriers absorbed. We therefore anticipate differences in charge segregation between the two regions. We observe that emission over SnO_x reduces at a faster rate than over NiO_x , indicating a higher rate of charge segregation over the electron-extracting electrode SnO_x . It is difficult to ascertain the nature of the change in radiative decay behaviour from these confocal measurements, however, as the small point of excitation and detection achieved via confocal time-resolved PL microscopy is additionally influenced by charge carrier diffusion away from the point of excitation, as explained by Yang et al.⁷²

6.3 Recombination in isolated perovskite films

To further examine the changes in photoluminescence for MAPbI_3 deposited over electrode materials, we prepare isolated films of MAPbI_3 deposited on glass, SnO_x , and NiO_x ; all topped with PMMA (details in Chapter 3). Measurements of isolated films on electrode materials provides two advantages over measurements on device structures: simplification of the probed system which allows for the influence of only one parameter to be identified (e.g. one electrode material), and sample uniformity allows for large-area measurements (i.e. non-confocal) whose results are not influenced by diffusion outside of the collection region. We perform photoluminescence quantum yield (PLQE) and time-resolved photoluminescence measurements on the achieved films.

Table 6.1 lists the photoluminescence quantum yields achieved for each film. When MAPbI_3 is deposited over electrode materials the quantum yield is found to be reduced. Photoluminescence quenching upon addition of an electrode material suggests either (i) increased interfacial nonradiative recombination or (ii) charge segregation which would lower radiative rates due to reduced overlap of electron and hole populations, and hence increase the competitiveness of nonradiative recombination channels. While we find a higher rate of recombination over NiO_x in photocurrent measurements (Chapter 4), we find less photoluminescence quenching in the case of MAPbI_3 on NiO_x than on SnO_x . This discrepancy between photocurrent and photoluminescence results suggest that nonradiative recombination is not the primary driver of photoluminescence quenching

Table 6.1 Summary of PLQE and TRPL measurements of MAPbI₃ films: PL yields for each electrode material, ratio of PL emission at 50 ns delay time and immediately after photoexcitation, and the long-lived lifetime component of TRPL results. PLQE measurements were obtained at ~ 1 sun illumination (532 nm, 75 mW cm⁻²).

Electrode Material	PLQE	TRPL	
		PL _{50ns} /PL ₀	Long-lived component
SnO _x /FTO	0.18%	0.01	750 ns
NiO _x /Ni	0.48%	0.06	620 ns
No Electrode (glass)	5.2%	0.17	1000 ns

in our system. This implies that charge segregation is the dominant mechanism driving PL quenching.

To further investigate recombination and the origin of photoluminescence quenching, we measure time-correlated single photon counting (TCSPC) photoluminescence of MAPbI₃ films prepared over electrode materials and on glass (Figure 6.2a). In all samples we find an initial drop in PL intensity in the first ~ 50 ns after excitation, after which the PL intensity decays at a much slower rate, with a lifetime that is comparable to the case of uncontacted films. We note that this measurement, in addition to being performed over a large area, is performed at a low laser fluence (407 nm, 5 nJ cm⁻², 100 kHz, ~ 0.01 suns). Thus each pulse is expected to generate excitation densities of less than 10¹⁵ cm⁻³ in the investigated region.

The initial drop in PL in the case of excitation on glass is indicative of the presence of trap states, which remove charge carriers at early times. As trap states fill, the rate of decay of free carriers reduces, resulting in a long-lived decay of photoluminescence intensity after ~ 50 ns. In the case of MAPbI₃ deposited on charge extracting electrodes, we also observe a reduction of photoluminescence intensity at early times. This reduction, however, is much more pronounced, agreeing with quenching by charge transfer to the electrode material. Furthermore, the return to a long-lived radiative process despite deposition over electrode materials demonstrates that nonradiative interface recombination is not the primary driver of PL quenching in our system, since such a recombination process would continue after 50 ns. Instead, our results show a difference in the level of charge segregation achieved in the case of each electrode. The PL intensity at 50 ns after excitation (Table 6.1) over SnO_x is reduced by a factor of ~ 6 relative to the case of NiO_x. This implies a larger spatial charge segregation in the

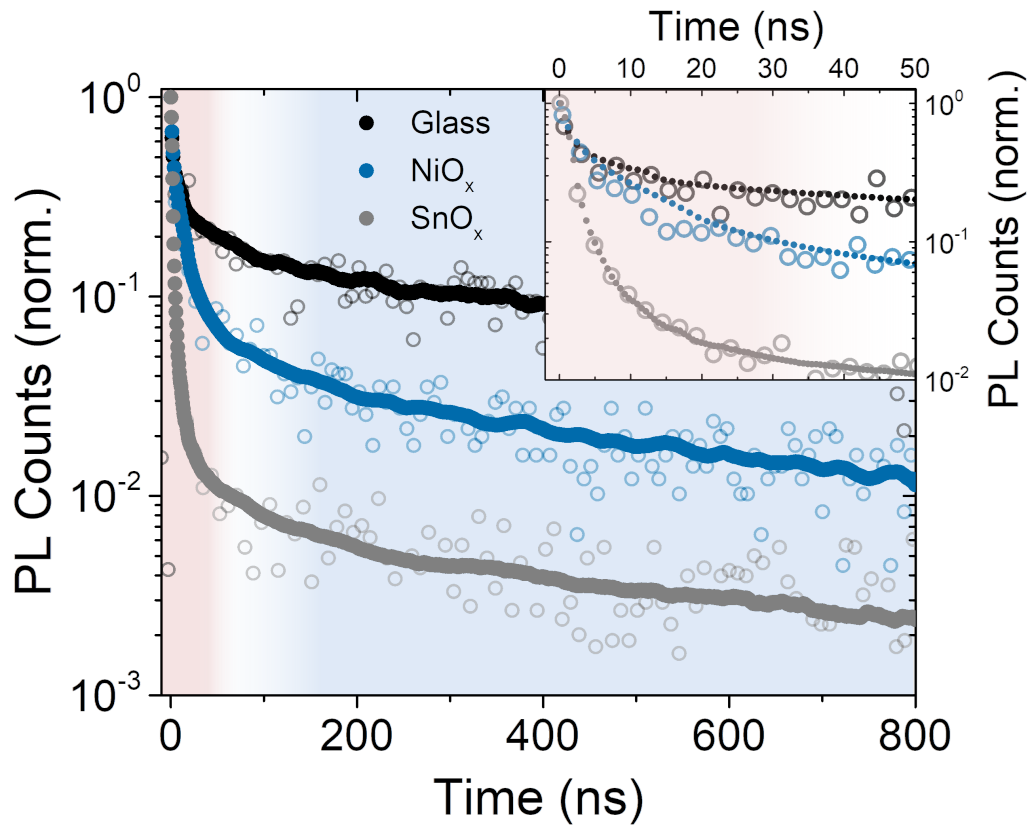


Figure 6.2 Time-resolved photoluminescence measurements for MAPbI₃ films on glass (black), NiO_x on nickel (blue), and SnO_x on FTO (grey). Data is presented in open circles together with smoothed curves. The decay in photoluminescence shows two regimes: (1) a fast decay in the initial ~ 50 ns, (2) a long-lived decay approaching similar lifetimes. The inset focuses on the early decay of PL intensity. On contact materials, the fast decay is more pronounced, with the largest drop in PL rate observed in MAPbI₃ deposited over the electron-extracting material, SnO_x. The long lifetime component in the case of electrode materials returns to a lifetime approaching the lifetime observed in MAPbI₃ deposited on glass. Measurements were performed at excitation fluences of 5 nJ cm^{-2} .

case of excitation over SnO_x (more complete extraction of electrons), which further reduces photoluminescence intensity. We suggest that the segregation process is the result of a band-offset at the electrode junction,¹⁷³ which our results suggest is larger over SnO_x . The return to the long-lived radiative component is possibly due to the release of carriers from trap states, as suggested by Leijtens et al.,¹⁶³ or possibly due to a limit to charge segregation as charges accumulate on either side of the electrode junction.

6.4 The effect of charge segregation on steady-state photoluminescence

While the behaviour of the presented devices and films reveals important charge segregation effects, it is important to examine the behaviour of the investigated system quantitatively. First, the influence of charge extraction electrodes on photoluminescence quantum yields will be examined to confirm that charge segregation alone can describe observed quenching effects. Therefore a one-dimensional kinetic model is prepared which incorporates charge segregation, diffusion, and monomolecular and bimolecular recombination. The system investigated is taken to be 500 nm thick, 300 nm of which is perovskite film and 200 nm of which is either inaccessible to both charge carriers, or is a charge-selective contact (i.e. accessible to one charge carrier type). In addition, a gradient of photo-induced charge generation is applied to reflect the reduced intensity of light as the excitation is reduced at larger film depths according to the Beer-Lambert law. As the film is assumed to be illuminated evenly, only transport through the thickness of the device is considered, and therefore the effects of photon recycling are simplified to a simple probability of photon re-absorption, similar to the work of Richter et al.¹²³ Illumination is taken to originate from the perovskite-side of the sample, and is equivalent to 1 sun of illumination.

In this way, the following rate equations are applied:

$$\frac{dn}{dt} = G_{sun} + D_n \frac{d^2n}{dx^2} - an - (1 - P)bnp \quad (6.1)$$

$$\frac{dp}{dt} = G_{sun} + D_p \frac{d^2p}{dx^2} - ap - (1 - P)bnp \quad (6.2)$$

where n and p are electron and hole densities, G_{sun} is the charge generation rate, $D_{n,p}$ is the diffusivity of each carrier type, P is the probability of photon escape, and a and

b are the monomolecular and bimolecular recombination coefficients. Diffusivities used here correspond to diffusivities found in Chapter 4.

Figure 6.3a presents the modelled charge carrier densities as a result of illuminating a film with no extraction electrode. Steady-state charge carrier density is expected to be $6 \times 10^{15} \text{ cm}^{-3}$ for each charge carrier, and a slight misalignment in charge density is predicted as a result of the differences in the diffusivity of each charge and the gradient in absorption. The overlap of charge carriers, however, is large. Therefore, the fraction of excitations which recombine radiatively is relatively high, at 11%.

Figure 6.3b show the results of modelling charge carrier populations in a film deposited over an electron-selective extraction electrode. To ensure that the effect of charge segregation is isolated, the extraction electrode is taken to be perfect: there is no surface or internal recombination pathway and the electrode removes electrons exclusively. In addition, the influence of a built-in potential driving charge extraction is modeled by assuming that 10% of electrons within 10 nm of the junction are extracted every time step, before diffusion is allowed to take place. The resulting charge segregation results in an overall increase in the peak charge density reached in the system. Holes accumulate in the perovskite film while electrons accumulate in the extraction electrode. As a result, PLQE is reduced to 3%.

These models correspond well to PLQE results in Table 6.1, where PLQE is found to drop by an order of magnitude or more as the result of deposition over electrode materials. It should be noted that, at open-circuit conditions, the increase in charge density upon charge segregation would likely lead to a higher proportion of carriers undergoing SRH recombination, as real electrodes and interfaces possess defects which will allow for nonradiative recombination. Our results demonstrate that charge segregation in films deposited over electrode materials can heavily impact photoluminescence quantum yield. Here we have investigated how this segregation affects PLQE results at open-circuit, but it is of great interest to investigate how charge recombination affects device performance and photocurrent.

6.5 Modelling device behaviour

Having identified that charge segregation is a driver of photoluminescence quenching in MAPbI_3 films deposited over electrode materials, a one-dimensional kinetic model is prepared to investigate the spatial dynamics of charge segregation in photocurrent measurements as presented in Chapter 4, and therefore uses a high fluence. The

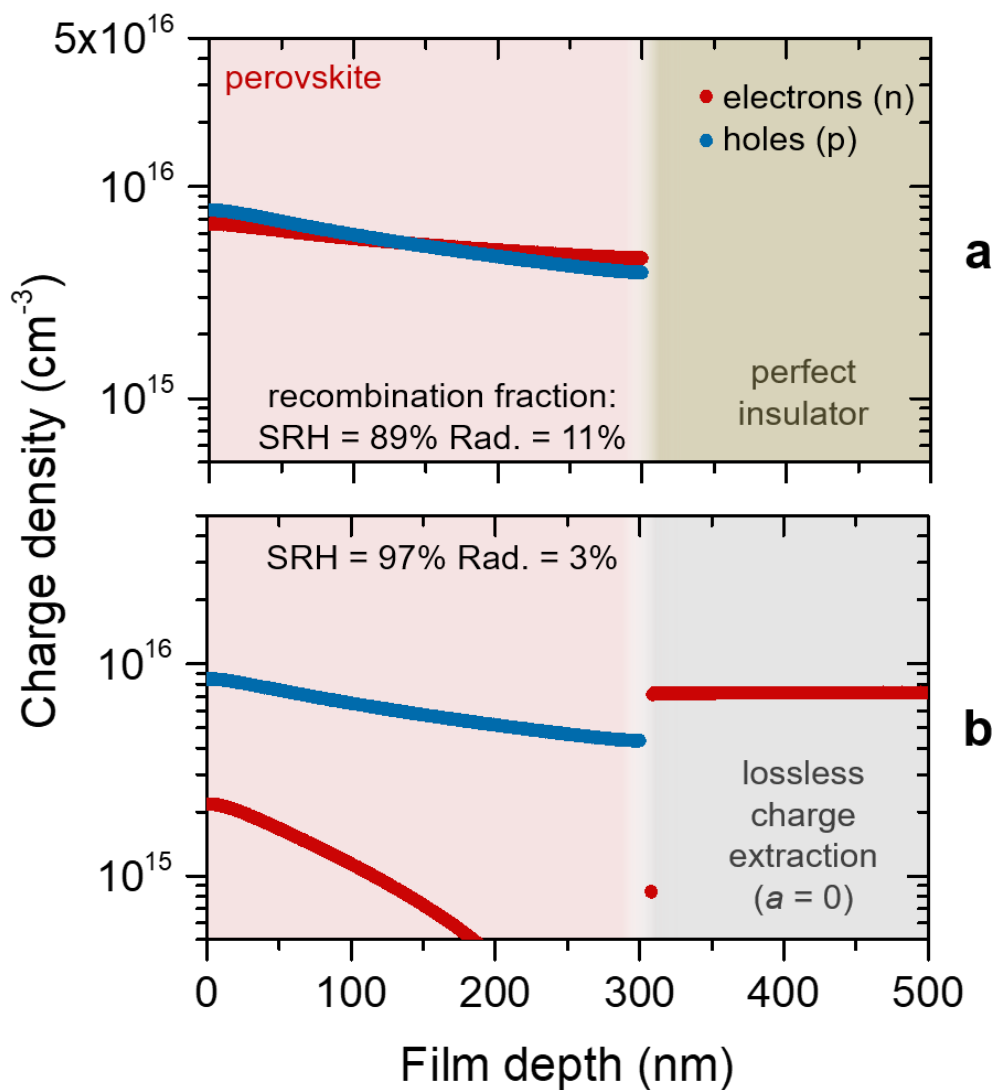


Figure 6.3 Modelling PL quenching as a result of charge segregation. a) Expected charge carrier population resulting from 1 sun illumination of a 300 nm thick perovskite film deposited on a perfect insulator. Slight imbalance of charge distribution is the result of a higher electron diffusivity. The predicted PLQE value is 11%. b) Expected charge carrier population resulting from 1 sun illumination of a 300 nm thick perovskite film deposited on an ideal electrode with a built-in potential driving electron extraction at the junction. The system is under open-circuit conditions, and no recombination pathway is provided for charge carriers within the electrode material. The resulting PLQE is reduced to 3%.

model aims to describe the situation encountered in excitation over SnO_x , that is, the evolution of charge populations as a result of point excitation of electrons and holes, global extraction of electrons and point extraction of holes. The model is then based on the following rate equations for hole concentration (p), and electron concentration (n) respectively:

$$\frac{dn}{dt} = G + D_n \frac{d^2n}{dx^2} - ap - (1 - P)bnp - J_e \quad (6.3)$$

$$\frac{dp}{dt} = G + D_p \frac{d^2p}{dx^2} - ap - (1 - P)bnp - J_h \quad (6.4)$$

where G is generation rate, a and b are the mono- and bimolecular recombination coefficients respectively, D_n is the diffusivity of electrons, D_p is the diffusivity of holes, P is the probability an emitted photon is reabsorbed, and $J_{e,h}$ is the extraction term for each charge carrier. The system is one-dimensionalised for lateral charge diffusion through a thin film of perovskite deposited over an electron-extracting electrode, as in Ref. [156].

An array of 1000 1 μm -wide and 300 nm-thick boxes was created to eliminate edge effects, with generation rate (G) zero everywhere except at the central position. Diffusivities are set from photocurrent measurements reported in Chapter 4. The monomolecular decay rate, a , is used as a fitting parameter and applied to the majority carrier population.

The extraction term ($J_{n,p}$) is modeled significantly differently in the two cases. In the case of holes, J_h is zero at each position save for a variable point of extraction which models the distance to the electrode junction. Holes which successfully diffuse to the junction are assumed to be collected efficiently. Therefore, 99% of excess carriers at this position are removed each time step.

For electrons, J_e is positive everywhere to reflect excitation over the electron-extracting electrode. We have discussed the possibility that segregated charge populations influence extraction behaviour. One possible influence is charge accumulation across the electrode. To describe this further, excitations generated via absorption will diffuse and eventually either recombine or be extracted. As electrons can be extracted everywhere and holes can only be extracted in one location, a build up of holes within the perovskite film is expected, particularly away from the electrode junction. The amount of accumulation will depend upon the rate of recombination and the rate of hole diffusion to the extraction electrode. As charges accumulate, a space charge layer may form within the electrode extraction material to maintain charge equilibrium. To

account for this possibility, we apply a charging term to describe a growing field which will resist electron extraction as charges accumulate within the perovskite film. For ease of modelling, we calculate the space charge based upon the number of holes remaining within the perovskite film, and predict they will accumulate near the electrode. As we use the population of holes to predict space charge effects, our model does not predict where the space charge layer would form within the electron-extracting electrode. Indeed, SnO_x is very thin, and it is likely electrons are extracted efficiently from SnO_x by FTO.

Therefore, we assume holes remain within the perovskite, creating a positive space charge dependent on the relative concentration of holes to electrons. The difference in charge between the perovskite film and the electrode is assumed to result in a field pointing into the electrode from the active layer, resisting electron extraction. The magnitude of the field will be related to the potential offset at the electrode junction and the amount of charge within the perovskite film. The charge-induced field (\vec{E}) will depend on the difference between the number of holes and electrons within the perovskite. Taking h to be the height of the film, the magnitude of the field will be:

$$\vec{E} = \frac{qh(p-n)}{\epsilon} \quad (6.5)$$

where q is the fundamental charge, and ϵ is the dielectric constant. As the charge increases, the extraction of carriers will be reduced. We modify a simple extraction rate times charge density with a term to overcome the building electric field minus the voltage offset (V_{bi}):

$$J_e = nve \frac{q\vec{E}d - qV_{bi}}{k_B T} \quad (6.6)$$

where v is the rate of carrier extraction, k_B is Boltzmann constant, T is the temperature, and d is average position of carriers in the perovskite. Carrier populations evolve independently, save for the population dependence of radiative recombination and the minimum ratio of electrons to holes set via the extraction term. A large fraction of radiative recombination is expected to be reabsorbed.¹²³ To account for this, the rate of carriers lost due to radiative recombination at each point is taken to be: $b \cdot (1 - P)$. Table 6.2 lists the parameters used in Figure 6.4. The built-in voltage offset is heavily dependent on the preparation technique of SnO_x , we use a moderate value of 0.15 eV.

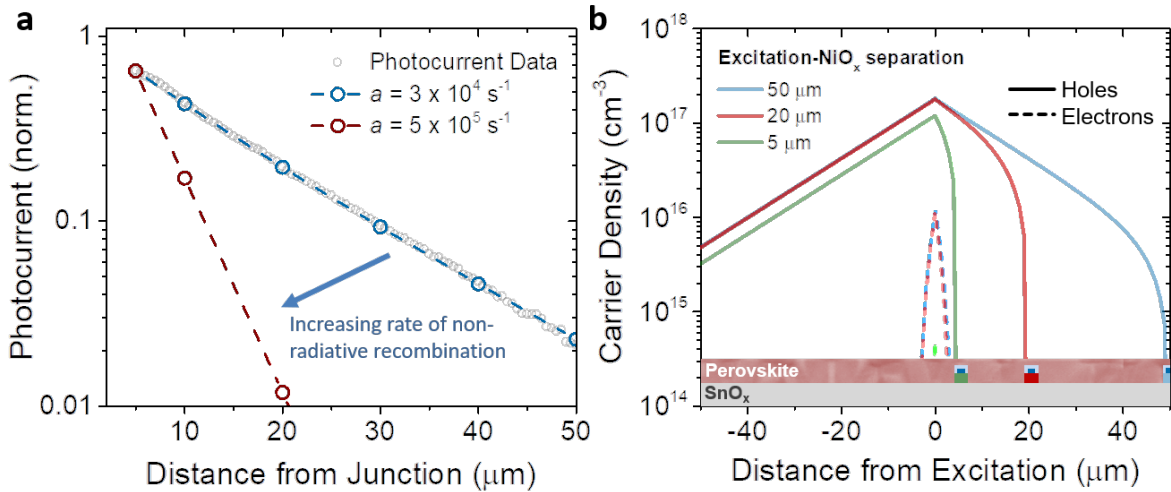


Figure 6.4 a) Predicted photocurrents one-dimensional model vs obtained photocurrents in Chapter 4. Grey circles are measured photocurrent values. The blue circles are fitted photocurrent values using diffusivity values found in Chapter 4, by varying recombination velocities and extraction and electrode parameters provided in Table 6.2. Here, the observed photocurrent trend is contrasted with predicted photocurrents similar to bipolar conditions using a different recombination velocity (red circles). The recombination rate used was reported for high-performing $\text{MAPbI}_{3-x}\text{Cl}_x$ by Richter et al., [123] and represents expected photocurrent behaviour if electron and hole populations do not segregate. b) Here we present predicted steady-state charge distributions for predicted photocurrent trends presented in blue in (a). Charge distributions are presented with excitation—junction separations of 5 (green), 20 (red), and 50 μm (blue) for excitation over the electron-extracting layer. Excitation is centred at 0 μm distance, no hole-extraction occurs at negative distances. Hole populations are represented by solid lines, while electron populations are represented by dashed lines. Increasing the distance to the extraction point increases the accumulation of charges away from the electrode junction.

Table 6.2 Parameters used in device modelling. Transport parameters and monomolecular recombination velocities match values in Chapter 4.

Parameter	Value	
Generation rate (G)	$1 \times 10^{11} \text{ s}^{-1}$	
Monomolecular recombination rate (a)	$3.6 \times 10^4 \text{ s}^{-1}$	
Bimolecular recombination coefficient (b)	$8.1 \times 10^{-11} \text{ cm}^3 \text{ s}^{-1}$	[123]
Hole diffusivity (D_p)	$0.07 \text{ cm}^2 \text{ s}^{-1}$	
Electron diffusivity (D_n)	$0.13 \text{ cm}^2 \text{ s}^{-1}$	
Probability of reabsorption (P)	0.86	[123]
Temperature (T)	298 K	
Extraction rate (v)	$3 \times 10^{11} \text{ s}^{-1}$	[156]
Position of electrons (d)	35 nm	
Dielectric constant (ϵ)	$70\epsilon_0$	[30]
Built-in potential (V_{bi})	0.15 V	
Thickness of film (h)	300 nm	

To examine the influence of nonradiative recombination rate on photocurrent measurements, Figure 6.4a presents the predicted photocurrent at varying excitation—junction separation. Grey circles represent measured photocurrent values. The monoexponential decay of photocurrent in our measurements demonstrates that the dominant form of recombination for charges traveling over the electrode material into which they cannot diffuse is monomolecular. Given the diffusivities found in transport measurements in Chapter 4 (also presented in Table 6.2), we vary recombination velocity and electrode behaviour (built-in potential, position of electrons) to fit obtained photocurrent values. In addition, predicted photocurrent from the presented model (blue circles) is compared to expected behaviour in the case of bipolar diffusion conditions in $\text{MAPbI}_{3-x}\text{Cl}_x$ (red circles). In bipolar conditions the recombination rate increases, and we apply a relatively low recombination velocity reported by Richter et al.¹²³ This exemplifies the remarkably extended transport parameters found in our architecture. As the diffusivities found here are on the low end of reported values, we have suggested that charge segregation is the primary driver of extended diffusion lengths in our system.

Figure 6.4b presents predicted steady-state carrier population distributions for varying excitation—junction distances for photocurrent measurements as modeled in Figure 6.4a (blue circles). This illustrates the expected overlap of electron and hole population. Most injected electrons (dashed lines) are extracted by the electrode material. Charge populations build up at the point of excitation. In the case of excitation near the electrode junction, holes have only a short distance to travel before extraction and the resulting build-up of generated carriers at the point of excitation is reduced relative to excitation further from the electrode junction. We note here that despite our assumptions that a space charge layer develops to limit charge extraction, the effects of charge accumulation are only visible in our predicted carrier populations near the point of excitation. This is expected behaviour, as significant overlap of charge populations would result in higher radiative recombination rates and we would not expect monoexponential behaviour in photocurrent trends. We therefore recognise that our assumptions concerning hole accumulation and the development of a space charge layer are difficult to probe in the given measurement architecture, and furthermore that presented photocurrent results do not demonstrate that a significant space charge layer is formed. A precise knowledge of energy offsets and band bending at the interface, as well as any screening contributions from e.g. charged defects and ions, are required to accurately predict the charge distribution within the device. If such effects screen any field effects of the accumulated hole population, then electrons are expected to be removed more efficiently from the perovskite film further segregating charge populations.

6.6 Discussion

These findings demonstrate that the investigated device architecture operates as postulated, segregating charge carriers and allowing electron and hole transport to be investigated. We show that upon charge segregation, the rate of nonradiative and radiative recombination is significantly reduced, and model how charge carrier populations build up within the device. Under short-circuit conditions the reduced rates of charge recombination allow charges to travel further. This improves charge collection as is indicated by the QIBC device with a J_{SC} of 18.4 mA cm^{-2} presented in Figure 4.1.

Futhermore, note that photocurrent measurements are sensitive only to carriers which successfully reach electrodes for extraction, and for this reason we choose

to present the recombination velocity of carriers travelling across the device. Total recombination velocity (v) is presented assuming a film thickness (h) of 300 nm ($v = ha$). Electron and hole lifetimes ($\tau_l = 1/a$) extracted from photocurrent measurements are therefore slightly overestimated due to insensitivity to recombination at the point of excitation. We can further explore this using the long-lived component of TCSPC results presented in Table 6.1, where the long-lifetime component of the radiative decay is found to be 620 ns and 750 ns in the case of MAPbI₃ on NiO_x and SnO_x, respectively. These values are shorter than the long-lifetime component on glass, which is $\sim 30\%$ longer (1 μ s). From this, it appears that the rate of nonradiative recombination (a) of charge carriers increases as a result of the introduction of the electrode interface. The total recombination rate, however, is reduced due to the reduced overlap of electron and hole populations. This vertical separation of charge carriers requires further information to accurately model, as our one-dimensionalization localises all carriers that remain within the perovskite layer in one volume. It is likely that further charge segregation as a result of ion migration and non-linear fields within the thickness of the perovskite film¹¹⁷ further affect charge population overlap and therefore recombination behaviour.

6.7 Conclusion

These results show that charge segregation effectively improves charge collection and reduces recombination at short-circuit conditions. While the interfaces between perovskite absorber layers and charge extraction materials are expected to contribute significantly to current and open-circuit voltage losses,¹⁸⁰ we show that carriers can move across perovskite—NiO_x/SnO_x interfaces with unexpectedly low losses, with recombination velocities found to be under 2 cm s⁻¹. For these IBC devices, improved fabrication to reduce the dark saturation current is expected to improve V_{OC} to beyond 1 V, and improved optical design and charge extraction will increase the photocurrent towards 27 mA cm⁻². By further combining the low recombination velocities demonstrated here with improved perovskite passivation via chemical treatment¹²⁵ and compositional tuning,^{62,128} highly efficient IBC perovskite devices will be achievable.

Chapter 7

Photoluminescence flickering in perovskite thin films

Previously, we discussed the process of charge recombination in back-contact films and devices (Chapter 6) and changes in recombination as a result of varying illumination and applied bias conditions (Chapter 5). Here, we investigate the local variation in charge recombination within polycrystalline thin films of a mixed-halide perovskite material: $\text{MAPbI}_{3-x}\text{Cl}_x$. We use scanning photoluminescence microscopy to investigate the temporal evolution of local photoluminescence behaviour, and find that the fundamental behaviour of investigated films varies on timescales of seconds to minutes. We further probe this behaviour using local TCSPC measurements to track changes in photoluminescence temporal behaviour. We observe that investigated $\text{MAPbI}_{3-x}\text{Cl}_x$ grains “flicker,” and the emission of individual domains changes in intensity, wavelength, and temporal behaviour. Our results indicate that the development of nonradiative recombination centres contribute to the variation in local photoluminescence, though further efforts are needed to identify the exact mechanism leading to flickering behaviour.

7.1 Background and motivation

The swift increase in metal-halide perovskite device efficiency over the past decade, as well as the resulting large number of research groups dedicated to optimizing device efficiency, may lead those outside the field to surmise that the fundamental behaviour of perovskites is well understood. Of great interest to the author, however, is the large volume of optical and electronic properties which remain unclear. Several open questions are listed in Section 2.1.3, but of relevance here is the spatial

variation in photoluminescence and photocurrent behaviour of perovskite films and devices.^{56,108,116,168}

Intermittancy in photoluminescence has been found in reduced-dimension materials such as quantum dots^{181,182} and organic single molecules.¹⁸³ In these cases, the variation is termed PL “blinking,” as the intermittancy can be described by high emission “on” states, and low emission “off” states. Recent studies have reported PL blinking in perovskite nanostructures,¹⁸⁴ which has been argued to be the result of changes in nonradiative pathways. Specifically, Merdasa et al. argue that a mobile trapping defect of one charge carrier type localises near an immobile trapping state of the opposite charge carrier, forming a highly efficient recombination channel which can ultimately dissociate once more.¹⁸⁵

Focusing on polycrystalline films, several studies have reported spatial variation in the PL behaviour, including variation in photoluminescence intensity,¹¹⁶ TRPL decay rate,⁷² and PL wavelength.¹⁶⁸ In addition, several studies have reported changes in photoluminescence with time, focusing on the degradation of perovskite films as a result of illumination,¹⁸⁶ or the influence of atmosphere on photoluminescence.¹⁸⁷ In 2016, Li et al. reported the observation of photoluminescence intermittency in perovskite thin films.¹⁴⁰ Here, we collaborate with Dr Chen Li to further investigate the origins of the flickering behaviour in polycrystalline films. We find that changes in photoluminescence behaviour occur on both long and short timescales, complicating interpretation. Nevertheless, we use spatially-resolved and time-resolved photoluminescence to rule out the Moss-Burnstein effect, and probe the influence of atmosphere on photoluminescence intermittency. While we are unable to indentify the precise origin of PL intermittency, we observe the development of defined states of emission. Our results indicate that the “supertraps” proposed to act in perovskite nanocrystals may act similarly in thin films, therefore the number of nonradiative recombination centres within the crystallite domain determines the emission state of the probed volume.

7.2 Changes in PL spectra upon flickering

In order to investigate spatial and temporal variation in photoluminescence, we use a confocal photoluminescence measurement of a selected region of a $\text{MAPbI}_{3-x}\text{Cl}_x$ thin film and monitor the evolution of PL spectra as the result of continuous CW laser excitation. Figure 7.1 outlines the means of measurement. Figures 7.1a and 7.1b show an example optical micrograph and a photoluminescence map of the region around

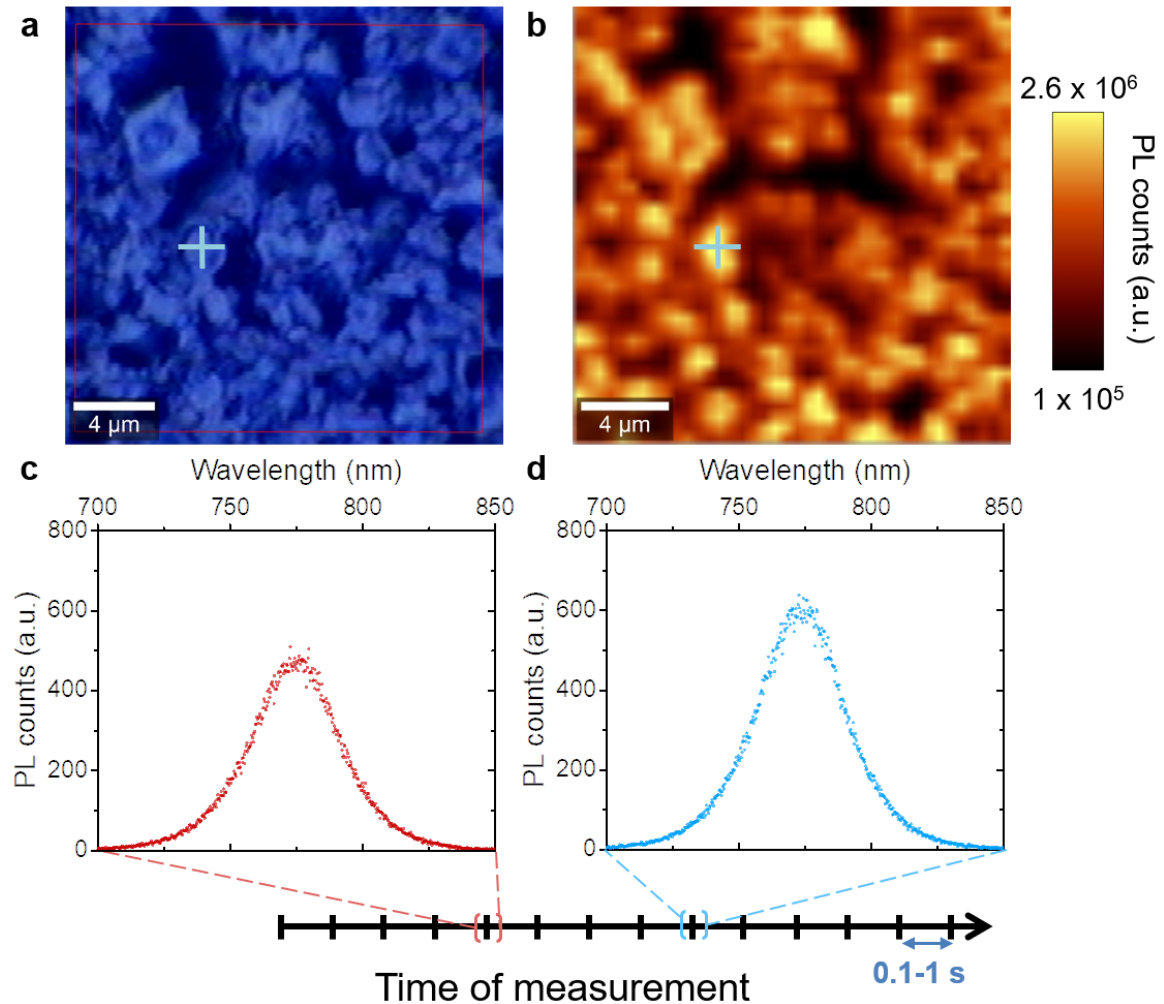


Figure 7.1 Measurement of the temporal evolution of local PL spectra. a) Optical micrograph of the investigated region of a polycrystalline $\text{MAPbI}_{3-x}\text{Cl}_x$ film, showing crystallite sizes of $<1 \mu\text{m}$ and the presence of pores in the film. Films are prepared on glass, and exposed to air. b) Scanning photoluminescence intensity map of investigated region in (a). Figures (c) and (d) provide examples of spectra obtained at different times while exciting, and detecting, photoluminescence at the investigated point (blue cross in (a) and (b)). The PL intensity is observed to increase and decrease with time during continuous illumination.

the point of interest, respectively. Scans are performed with 0.1 s integration time, allowing for a PL spectrum to be obtained at each point in space. After mapping is accomplished, the region of interest is identified (blue cross) and a measurement through time is obtained (Figure 7.1c,d). In this case, integration times vary from 0.1 to 1 s, and the changes in PL spectra are monitored.

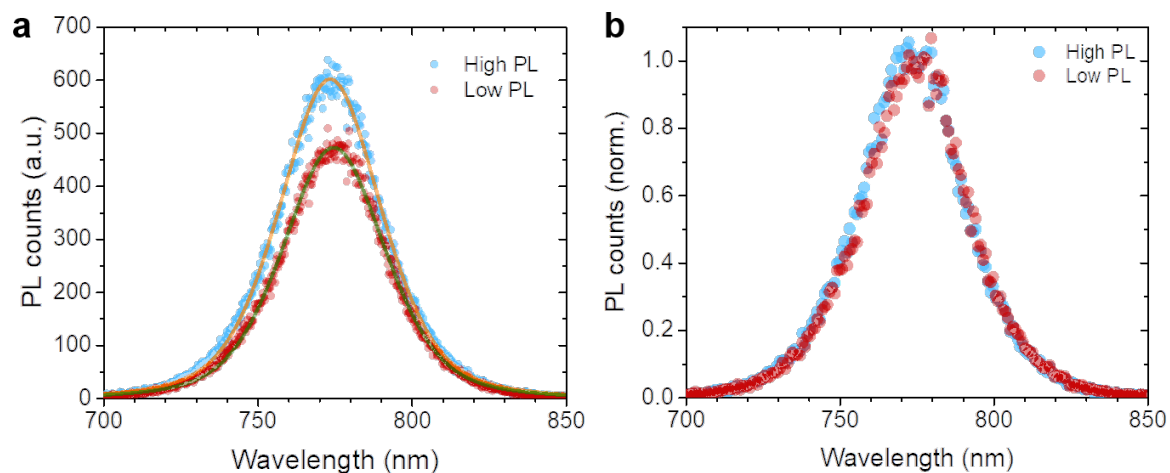


Figure 7.2 Changes in PL spectra with time. a) Two example photoluminescence spectra obtained at the same position within a $\text{MAPbI}_{3-x}\text{Cl}_x$ thin film at different times characterised by high PL intensity (blue circles) and low PL intensity (red circles). Example fits of PL spectra are presented for each case, from which peak position and peak intensity are acquired. b) Normalised PL spectra presented in (a). The full width at half maximum of emission appears unchanged upon changes in luminescence behaviour. Excitation is accomplished with 11 W cm^{-2} average power of 405 nm focused light (spot size $\sim 1.5 \mu\text{m}$).

In order to identify the origin of PL flickering, we examine the changes in photoluminescence spectra. Figure 7.2a shows two example obtained spectra, while Figure 7.2b presents normalised spectra from Figure 7.2a. First, we observe that the full-width half-maximum and shape of the emission does not change between emission levels. This indicates that the nature of the emissive state does not change. Second, we observe that the intensity and position of the PL peak are shifted. An increase in intensity implies that i) a larger number of charge carriers is being generated via increased absorption, ii) the kinetic balance of nonradiative and radiative recombination shifts to favour radiative recombination, iii) transport conditions change and generated carriers no longer diffuse from the excitation region, or iv) a new emissive state arises. The shift in photoluminescence peak position implies that the energetic landscape within the probed volume of film changes, however the shift is small therefore it is unlikely

an entirely new emissive species is being generated. More likely, local changes in quasi-Fermi level slightly shift the emission as the result of: i) compositional change, ii) development of field, or iii) the Moss-Burnstein effect (i.e. band filling).

We take a moment to discuss these potential changes. A compositional change could occur in perovskites, as vacancies, cations,¹⁸⁸ and especially halides^{55,56} have been shown to be mobile. The timescales for such motion has generally been found to occur over the seconds to minutes range. The development of field within the film could result from mismatched charge carrier diffusivity, as found in Chapter 4. The timescale for charge carriers to move across a grain is on the nanosecond regime. Similarly, charge transport from grain to grain across grain boundaries is expected to occur on a similar timescale. The Moss-Burstein effect occurs when the local density of charge carriers is very high, such that the conduction and valence band edges are filled and emission blue shifts. In this event, charge carrier emission is expected to be very efficient. Finally, changes in recombination pathways via the development of traps is proposed to be the general mechanism of PL blinking in perovskite nanocrystals.^{184,185} The proposed mechanism is the association and dissociation of electron and hole traps: when an electron trap is very near to a hole trap, a new “supertrap” is formed which adds a very efficient nonradiative recombination pathway.

As stated previously, we do not observe changes in the shape of photoluminescence spectra, instead observing shifts in PL peak position and PL intensity between flickering events. Figure 7.3 presents the changes in PL peak position and peak PL wavelength in time. We observe that shifts in each value occur simultaneously, and that increases in PL intensity couple with decreases in peak PL wavelength. Rapid changes in PL behaviour, such as at 4, 26 and 57 s, imply that the underlying process shifts emission behaviour in under 100 ms. We observe that the shift in PL intensity in these rapid events can be substantial, for example at 4 s the PL intensity drops 10%. The rapid transition between states in less than 100 ms indicates that simple ion or vacancy-driven compositional changes do not describe fast PL flickering behaviour, as such processes tend to be occur over the seconds to minutes range. Changes in charge transport leading to electrical isolation of the investigated region could still occur as charge carrier transport phenomena occur at timescales below the resolution of this investigation. Furthermore, changes in radiative or nonradiative recombination cannot be ruled out from these measurements. The underlying physics are better probed using time-resolved PL measurements, which we introduce in the next section.

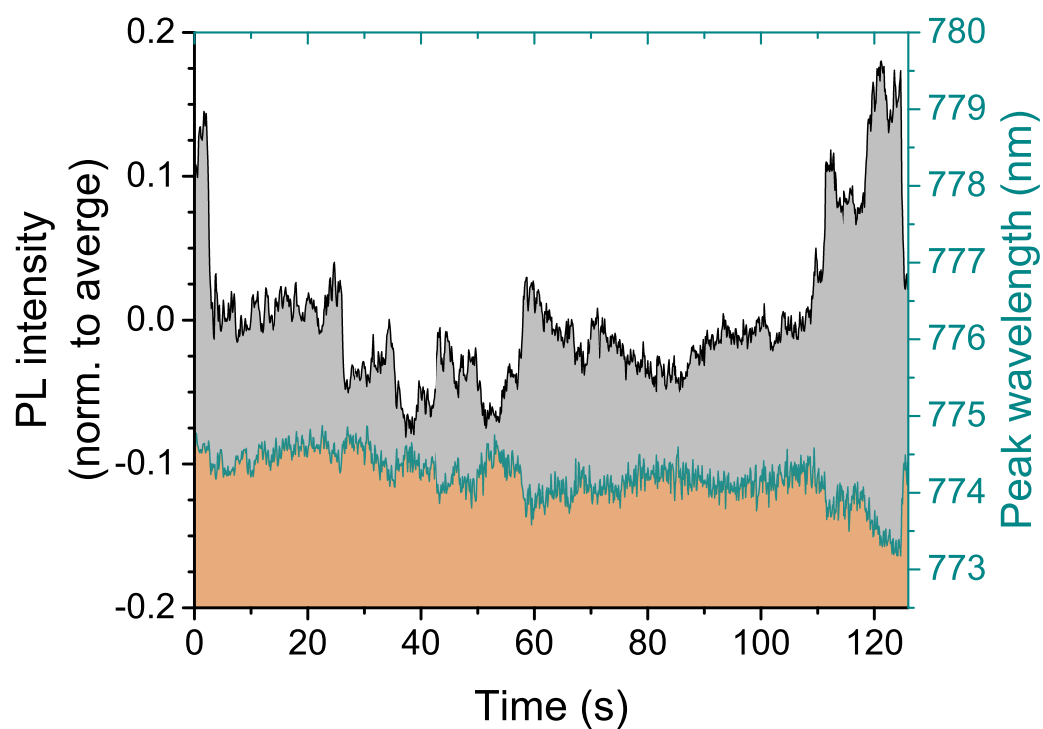


Figure 7.3 Evolution of fitted PL peak position and PL intensity for an investigated region under continuous illumination. The PL spectra for each timestep are fitted using a pseudo-Voigt function. Shifts to increasing PL intensity coincide with shifts to lower PL wavelength. Illumination is accomplished with 11 W cm^{-2} average power of 405 nm focused light (spot size $\sim 1.5 \mu\text{m}$).

7.3 Changes in TRPL decays upon flickering

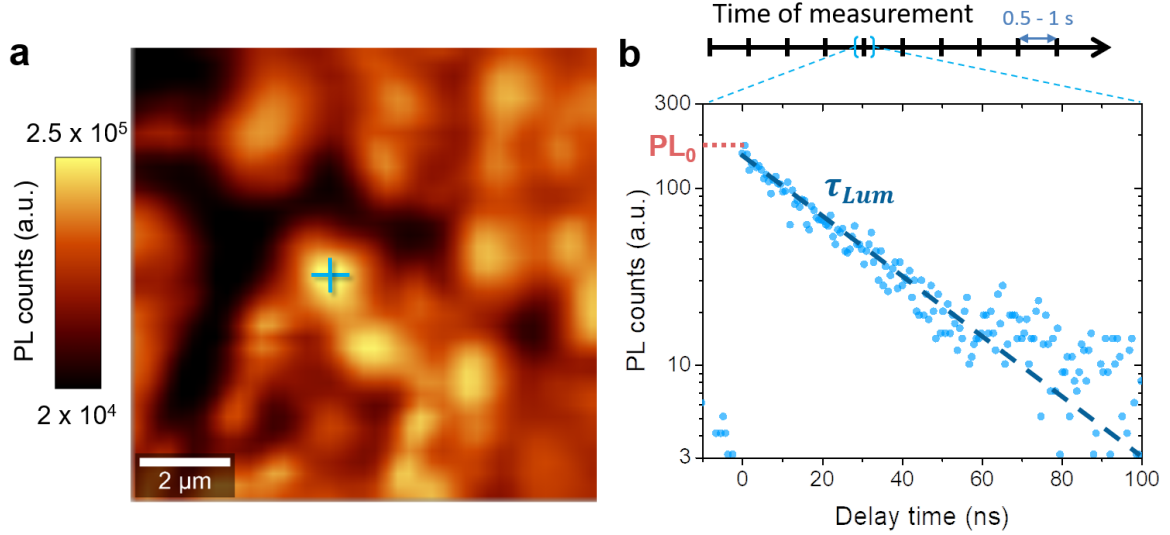


Figure 7.4 Tracking the temporal evolution of PL decays in time-resolved PL measurements. a) Example photoluminescence map of investigated region, with the point excitation shown by the blue cross. b) Example decay of photoluminescence intensity for a given timestep of measurement. PL decays are measured every 0.5 to 1 s at the same location (marked by a blue cross in (a)). The initial PL (PL_0) and luminescence lifetime, τ_{Lum} , are fitted using a monoexponential decay. Excitation is accomplished with 450 nm focused light (spot size $\sim 1.5 \mu\text{m}$) at fluences of $2.8 \mu\text{J cm}^{-2}$ and a 5 MHz repetition rate.

In order to further investigate the behaviour of flickering $\text{MAPbI}_{3-x}\text{Cl}_x$ thin films, we perform time-resolved photoluminescence measurements on a single spot in a film and monitor the change in PL decays as a result of constant pulsed illumination. The measurement technique is outlined in Figure 7.4, while the setup to accomplish local TRPL measurements is introduced in Figure 3.3. As in measurements of PL spectra (Figure 7.1), a photoluminescence map is obtained prior to measurement (blue cross in Figure 7.4a). Then, continuous TCSPC decays are obtained at the point of excitation. The initial PL intensity (PL_0) and a monoexponential luminescence lifetime (τ_{Lum}) are extracted from each PL decay.

Figure 7.5a describes the observed changes in photoluminescence behaviour. Upon transition from a high to low state of emission, both PL_0 and τ_{Lum} are reduced. From the observation that the luminescence lifetime increases with increasing luminescence intensity, we can rule out the Moss-Burstein effect as the origin of PL flickering. Band filling as a result of charge accumulation does blue-shift emission as found in PL spectra, but the high number of charges would increase the rate of radiative emission. We would

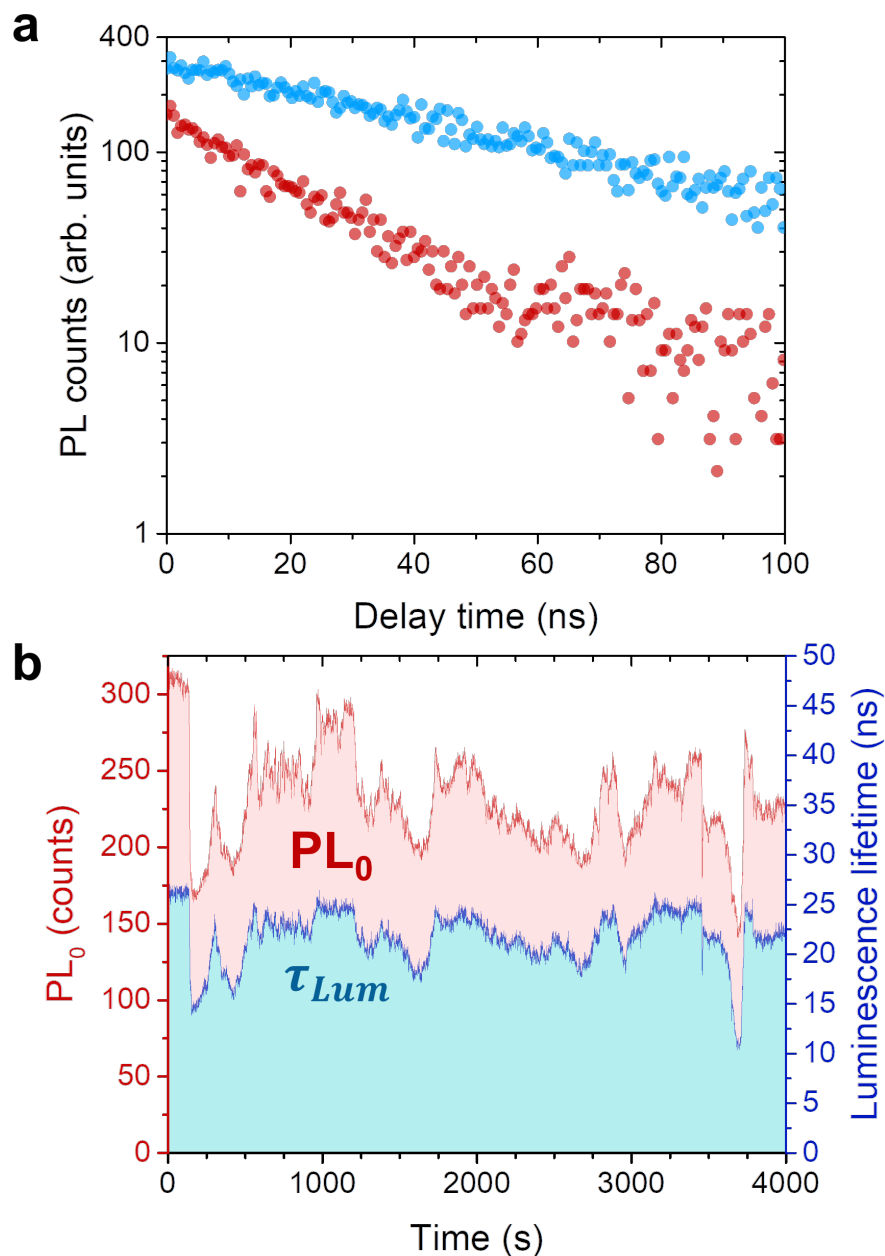


Figure 7.5 Temporal evolution of local PL_0 and PL lifetime (τ_{Lum}). a) Two example photoluminescence decays obtained during high (blue circles) and low (red circles) periods of PL intensity. Observed changes in photoluminescence decays include changes in PL_0 and τ_{Lum} . b) Evolution of PL_0 and τ_{Lum} for an investigated region under consistent pulsed excitation. PL_0 and τ_{Lum} are observed to evolve together. A Fianium supercontinuum laser with 6 ps pulses is employed at a repetition rate of 5 MHz. Measurements are accomplished with 450 nm focused light (spot size $\sim 1.5 \mu\text{m}$) at fluences of $2.8 \mu\text{J cm}^{-2}$.

therefore expect an increase in PL_0 and a decrease in luminescence lifetime upon band filling. In addition, changes in charge transport behaviour are not expected to influence PL_0 , as charge transport over the μm range occurs on the 100 ns timescale. Therefore, we consider it unlikely changes in charge transport behaviour are responsible for PL flickering. Changes in charge recombination pathways remain a possible explanation, however.

In Figure 7.5b the absolute change in PL_0 and luminescence lifetime are plotted against measurement time. As in the case of PL spectral changes in Figure 7.2, a variety of flickering intensities are observed. In addition, PL_0 and luminescence lifetime are found to change simultaneously, and therefore the underlying process must affect both the number of charge carriers available to recombine at early times and the dynamics of charge carrier recombination.

To better observe the change in time-resolved PL decays, we plot the normalised values of count rate, PL_0 , and τ_{Lum} in Figure 7.6. Here we observe that while both PL_0 and τ_{Lum} change simultaneously with changes in film emission, the relative shift in luminescence lifetime is less than the change in PL_0 . This indicates that changes in the number of charge carriers at early times is the primary driver of changes in photoluminescence behaviour. This result complicates interpretation. A highly-efficient charge recombination pathway that acts to reduce the number of charge carriers in the system within the time resolution of the TRPL measurements (e.g. first ~ 1 ns), should also continue to drive charge recombination beyond the first nanosecond. We therefore consider two potential effects of trap states. First, a general increase in the density of nonradiative recombination pathways may influence absorption behaviour of the system by altering the local band structure. This interpretation would agree with shifts in photoluminescence wavelength in PL spectra obtained in Figure 7.2, but disagrees with the decrease in PL_0 in TRPL measurements. Second, localised “supertraps” may depopulate a small volume of perovskite material, preventing emission from this region and reducing overall PL_0 . Subsequent recombination at the supertrap is then diffusion limited, and therefore would have only a marginal effect on the rate of PL decays in our measurements which already are diffusion-limited in nature due to the confined area of detection. Thus, we consider the formation of “supertraps” to be consistent with observed PL flickering behaviour.

We observe, however, transitions in photoluminescence count rate both over short timescales below the resolution of the measurement (< 1 s), and over long time scales (> 1 min). Figure 7.6 presents this behaviour clearly, with a fast transition process

marked at 214 s and a slow process occurring over ~ 100 s marked at 360 s. It is likely, therefore, that multiple processes occur in investigated $\text{MAPbI}_{3-x}\text{Cl}_x$ thin films which give rise to PL intermittency.

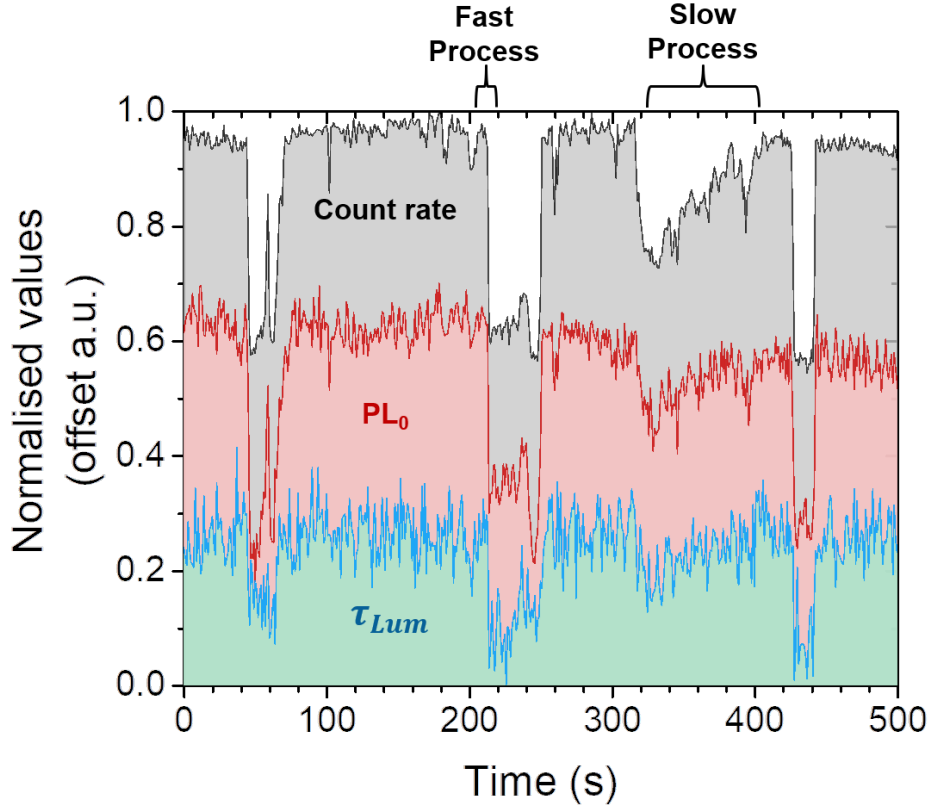


Figure 7.6 Evolution of count rate, PL_0 , and τ_{Lum} with time. Values are normalised and offset for clarity. While changes in PL_0 and τ_{Lum} occur simultaneously, we observe that the magnitude of change in PL_0 is higher than that in τ_{Lum} . In addition, we note that changes in all three values occur very quickly, below the temporal resolution of the measurement (Fast Process), and also more slowly, taking as long as a minute to occur (Slow Process). Excitation is accomplished with 450 nm focused light (spot size $\sim 1.5 \mu\text{m}$) at fluences of $2.8 \mu\text{J cm}^{-2}$ and a 5 MHz repetition rate.

7.4 Influence of atmosphere

In order to investigate the influence of atmosphere on photoluminescence behaviour, we perform measurements using a confocal microscope enclosed within an air-tight box. We flush the box with dry nitrogen gas, and observe changes in photoluminescence behaviour. In Figure 7.7, measurement is begun with the box filled with

air, at a temperature of 22 °C and a humidity of 48%. Nitrogen flow is begun at 25 s, and over the next minutes the air is displaced. This process is gradual, and the photoluminescence intensity is observed to decay over ~ 4 minutes. During this process, photoluminescence is observed to undergo at least two stages: a period of increased intermittency in photoluminescence between 70 and 170 s, followed by a period of more gradual decay in photoluminescence intensity until settling at roughly 10% of peak photoluminescence intensity from 390 s. After several minutes in dry nitrogen atmosphere, the box is opened, re-exposing the sample to air. Recovery of Photoluminescence intensity begins upon re-exposure, at 660 s. As photoluminescence intensity increases, intermittency is observed to increase with large flickering events at 774, 780, and 786 s. Initial photoluminescence intensity is not fully recovered within the time frame of the measurement.

This atmospheric dependence of photoluminescence intensity has been connected to water and oxygen vapour, which have been argued to adsorb to perovskite crystals and passivate crystallite surfaces and iodide vacancies, respectively.¹⁸⁷ Thus, exposure to dry nitrogen atmosphere would be expected to reduce photoluminescence intensity, as these passivation effects would be reduced increasing the rate of nonradiative recombination. The atmospheric dependence of photoluminescence behaviour shown here indicates that oxygen and/or water have an additional impact on PL intermittency, supporting the conclusion that intermittency is related to trap states. Interestingly, removal of both water and oxygen appears to suppress PL intermittency, while PL intermittency was maximised at lower-than-ambient oxygen and water concentrations. This indicates that a moderate amount of oxygen and/or water increases the rate and intensity shifts of PL flickering, though further investigations with precise atmospheric controls would help identify the precise connection between variations in atmosphere and photoluminescence flickering.

7.5 Discerning emissive levels and discussion

Generation of nonradiative recombination pathways via the formation of supertraps should result in defined levels of PL intensity depending upon the number of supertraps within an investigated volume. In order to visualise such emissive behaviour, Figure 7.8 plots the relative PL intensity against peak wavelength for PL spectra obtained as described in Figure 7.1. On each axis, histograms of PL peak position (yellow) and relative PL intensity (pink) are provided. We identify several probable wavelengths of

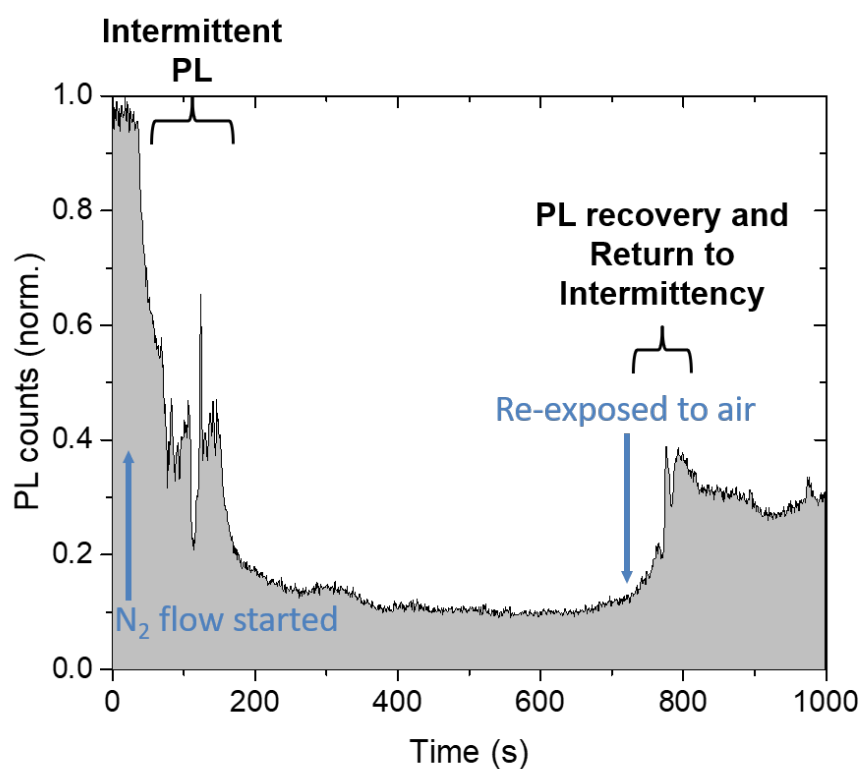


Figure 7.7 Evolution of PL intensity with exposure to dry nitrogen atmosphere. Measurement is accomplished within an air-tight box and begun in air. Dry nitrogen flow was begun at 25 s and ended at 720 s, at which time the door to the microscope was opened rapidly introducing air to the system. Photoluminescence intensity upon introduction of dry nitrogen reduces, and large variations in intensity are observed over the first ~ 100 s of nitrogen flow. As dry nitrogen displaces air, the photoluminescence intensity reduces further and flickering phenomena appear to end by 200 s. More gradual variation in PL intensity is observed until, at 720 s, nitrogen flow is halted and the sample is re-exposed to air. Some recovery of photoluminescence intensity is observed, as well as flickering. Excitation is accomplished with 450 nm focused light (spot size ~ 1.5 μm) at fluences of 9 $\mu\text{J cm}^{-2}$ and a 5 MHz repetition rate.

emissive species in the the histogram of PL wavelength, and shade them in blue. More clearly, several levels of photoluminescence intensity are observed, also shaded in blue. Observed shifts in intensity vary, however.

By combining the two histograms, we observe more clearly the nature of PL emission levels in the probed volume (Figure 7.8). Each level appears to provide peak wavelengths distributed over roughly 0.5 nm. We observe three long wavelength emissive levels with relative PL intensities centred at 0, -0.4 , and -0.7 ; each centred at 774.5 nm. At least two short wavelength and high intensity emission levels are observed, one centred at 773.8 nm and one at 773.5; though each of these states is broad in relative PL intensity. The majority of emission is at 774 nm, where it is challenging to identify clear changes in the level of emission. These step-like features in Figure 7.8 do not have regular separation, however. This does not discount the possibility that consistent supertrap behaviour is present in the system, however, as the location of a supertrap within the probed volume would determine its influence on PL. Finally, these step-like features indicate that a general increase in nonradiative recombination pathways is not the cause of observed PL flickering.

The presence of clearly discerned levels of emission presented in Figure 7.8, combined with TRPL results in Figure 7.6, is strong evidence for the formation of localised, efficient trapping centres within investigated $\text{MAPbI}_{3-x}\text{Cl}_x$ thin films. Such trapping centres act to deplete the charge carrier population locally via efficient nonradiative recombination and the formation and dissociation of supertraps impacts the response of investigated films to illumination. The presence of additional changes in photoluminescence behaviour over long timescales (as shown in Figure 7.6) indicates that slower processes, such as defect or ion migration, may influence local photoluminescence behaviour.

We argue that PL intermittency described here, though observed in $\text{MAPbI}_{3-x}\text{Cl}_x$ thin films, holds insights for wider phenomena in the family of metal-halide perovskite materials. The presence of trap centres would impact local photoluminescence efficiency, and therefore such trapping centres may contribute to the spatial variation of photoluminescence observed in literature.^{56,72,168} In addition, we observe that PL flickering necessarily results from illumination. The generation of recombination centres may be tied to observed degradation in device performance under illumination conditions.^{169,189} Furthermore, spatial variation in efficiency of photocurrent extraction has been reported in metal-halide solar cells,¹¹⁶ which could arise from the local variation in trap density. Finally, oxygen- and water-containing atmospheres have been reported to improve

perovskite photoluminescence.¹⁸⁷ This report has argued that oxygen acts to passivate iodide vacancies, and we demonstrate a connection between atmospheric conditions and PL flickering. Identifying the nature of trap states linked to photoluminescence flickering would therefore help elucidate the impact of atmosphere on nonradiative recombination in perovskite films.

7.6 Conclusion

Here we examine the process of variation in photoluminescence intensity under constant illumination: PL flickering. Specifically, we perform spatially- and time-resolved PL spectroscopy on $\text{MAPbI}_{3-x}\text{Cl}_x$ thin films. We identify that the most likely origins of flickering are changes in nonradiative recombination pathways, possibly via the association of electron and hole trap centres to form “supertraps” as proposed to describe the behaviour of perovskite nanocrystals.¹⁸⁵ Furthermore, we examine the effects of varying the atmosphere on flickering behaviour, and find strong evidence oxygen and/or water play a role in flickering behaviour. Finally, we show the process is significantly more complex in films than in perovskite nanocrystals as the variation in photoluminescence intensity involves fast and slow processes. We therefore conclude that it is likely photo-induced defect and/or ion migration also plays a role in photoluminescence intermittancy in polycrystalline films.

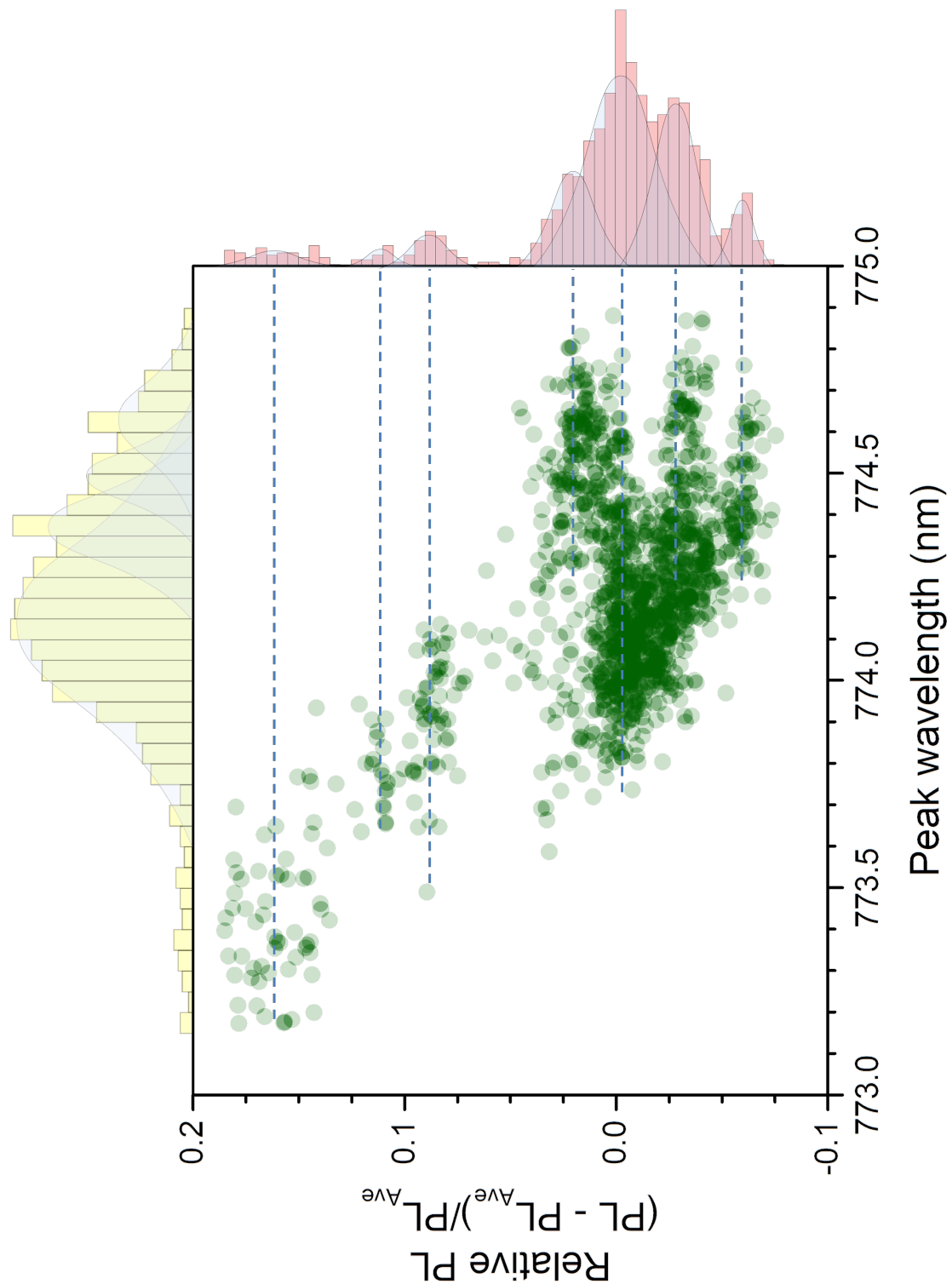


Figure 7.8 Relative PL intensity versus peak wavelength for obtained PL spectra. Here, we observe the general trend of lower PL wavelength with higher PL intensity. Within this, however, we observe several levels of PL emission, each distributed over roughly 0.5 nm in wavelength. Histograms of peak wavelength and relative PL intensity are provided in yellow and pink, respectively. Rough gaussian profiles outlining proposed states are outlined in light blue to guide the eye. Dashed lines marking the centre of peak PL emission levels are provided to guide the eye. The step-like features in PL intensity are not found to have regular separation. Excitation is accomplished with 11 W cm^{-2} average power of 405 nm focused light (spot size $\sim 1.5 \mu\text{m}$).

Chapter 8

Summary and Outlook

In this thesis I have investigated the transport and recombination dynamics of photo-generated charge carriers in metal-halide perovskite semiconductors. Chapters 4 and 5 focused on the characterisation of transport parameters of excited charge carriers, while Chapter 6 focused on the recombination of charge populations in metal-halide perovskites in contact with charge-selective electrodes. These chapters investigated the most common metal-halide perovskite composition $\text{CH}_3\text{NH}_3\text{PbI}_3$, which has shown great promise for application in solar cells. Furthermore, investigations on high-performing mixed-cation perovskite materials in Chapter 5 demonstrated that the improvements in transport and recombination reported here are directly applicable to the larger family of metal-halide perovskite materials. The transport and recombination properties presented in this work reaffirm the promise of perovskite-based devices: demonstrating extended diffusion ranges and long carrier lifetimes in the presence of extraction electrode materials. Our results highlight the potential for high-performing back-contact perovskite devices.

Chapter 4 introduced the device and measurement architecture employed to investigate the charge dynamics of electrons and holes separately. We found that photo-generated charges in polycrystalline perovskite films are capable of long-range diffusion over selective electrodes, with electrons and holes both having diffusion lengths exceeding 12 μm . We concluded that grain boundaries are not major barriers to charge transport in the $\text{CH}_3\text{NH}_3\text{PbI}_3$ films studied here. We further quantified the diffusivity of electrons and holes, and found that electrons are twice as mobile as holes. Finally, we demonstrated a back-contact solar cell which reaches 70% external quantum efficiency, showing the potential for perovskite back-contact devices. Further measurements are required to quantify effects grain boundaries have upon charge transport, as this

remains an open question in the field. Variation in the temperature of measurement and the size of crystalline domains would yield further information on the influence of grain boundaries on charge transport.

Under operating solar PV conditions, a metal-halide perovskite solar cell will develop a steady-state distribution of charge carrier populations. In Chapter 5 we presented a means of probing devices in such conditions. First, we investigated a vertical “sandwich” solar cell using time-resolved PL measurements, and argued that background illumination reduces the influence of charge segregation on time-resolved measurements. Then we turned to back-contact architectures and investigate charge extraction in the case of background illumination. We found that, under operating conditions, the extraction length for small perturbations increases significantly, up to 25 μm . These results have profound implications for device operation, as they demonstrate that vertical device structures likely benefit from the effects of charge segregation via electrode materials and show that charge transport of photogenerated carriers improves as the result of constant white light illumination. To understand further the influence of segregated background photoexcitation density on charge carrier transport, a careful comparison of results obtained from back-contact measurements and contacted films on glass or a non-ohmic contact should be accomplished. Such a measurement would reveal the influence the extraction electrode has on the steady-state charge population.

In Chapter 6, we investigated the origin of the low recombination velocities in photocurrent measurements, which are below 2 cm s^{-1} . We used PL quantum efficiency and time-resolved PL measurements to identify that the origin of reduced recombination velocities is charge segregation, which in turn is demonstrated to be the result of buried charge-selective electrodes. These remarkably low recombination velocities reveal that clever device design can suppress the detrimental effects of nonradiative charge recombination. Furthermore, we showed that carriers can move across electrode interfaces with unexpectedly low losses. To realise high-efficiency back-contact devices, metal-halide perovskite materials with superior transport characteristics should be used, and further optimisation of electrode interfaces may yet yield further reduced nonradiative recombination.

Spatial variations in photoluminescence and operation of perovskite films and devices have been reported and can limit device efficiencies. In Chapter 7, we examined the variation in photoluminescence in space and time in thin films of $\text{CH}_3\text{NH}_3\text{PbI}_{3-x}\text{Cl}_x$. Specifically, we observed an unexpected intermittency in $\text{CH}_3\text{NH}_3\text{PbI}_{3-x}\text{Cl}_x$ photolu-

minescence, and described it as a flickering phenomenon. We identified that the effect is caused by changes in available nonradiative recombination pathways, and found strong evidence for the presence of “supertrap” recombination centres proposed to describe blinking in nanocrystalline systems. We concluded, however, that the flickering phenomenon is significantly more complex in films than what has been reported in perovskite nanocrystals. Further investigations into the temperature-dependence of photoluminescence intermittency in mixed-halide systems are needed to reveal the exact origins of photoluminescence flickering.

There is great potential to improve our understanding of perovskite materials via investigation of back-contact architectures. This stretches from fundamental charge transport mechanisms, as discussed here, to overall processing effects. One means of both investigating and improving silicon solar cells involves gettering,¹⁹⁰ treating fully accomplished devices physically or chemically to remove impurities from the active region. Vertical “sandwich” device architectures, which have each major surface contacted by extraction materials, are poor candidates for gettering studies. Back-contact architectures, on the other hand, are ideal. Once prepared, the influence of varying chemical treatments, capping layers, and even varying perovskite compositions could be investigated on a single device: before and after treatment. In addition to demonstrating the potential of back-contact perovskite solar cells, this work presents techniques which would reveal the effects of such treatments on fundamental transport and recombination processes.

Presentations and Publications

Contributions during PhD

- **Tainter, D. Gregory**, Hörantner, M. T., Pazos-Outón, P. M., Lamboll, R. D., Āboliņš, H., Leijtens, T., Suhas, M., Friend, R. H., Snaith, H. J., Joyce, H. J. & Felix, D. Long-range charge extraction in back-contact perovskite solar cells via suppressed recombination. *Joule*, (**under review**) (2018).
- Alexander-Webber, J. A., Groschner, C. K., Sagade, A. A., **Tainter, D. Gregory**, Jagadish, C., Hofmann, S. *et al.* Engineering the photoresponse of InAs nanowires. *ACS Applied Materials & Interfaces* **9**, 43993–44000 (2017).
- **Tainter, D. Gregory**, Li, C., Hüttner, S. & Deschler, F. Investigating ion migration via photoluminescence blinking in perovskite films. *SPIE Nanoscience + Engineering, San Diego, USA* (August 2017).
- **Tainter, D. Gregory**, Li, C., Hüttner, S. & Deschler, F. Photoluminescence blinking in perovskite films. *Optical Probes 2017, Quebec City, Canada* (June 2017).

Master's Publications

- Guo, S., Wang, W., Herzig, E. M., Naumann, A., **Tainter, D. Gregory**, Perlich, J. & Müller-Buschbaum, P. Solvent-morphology-property relationship of PTB7:PC₇₁BM polymer solar cells. *ACS Applied Materials & Interfaces* **9**, 3740–3748 (2017).
- Niedermeier, M. A., **Tainter, D. Gregory**, Weiler, B., Lugli, P. & Müller-Buschbaum, P. Fabrication of hierarchically structured titania thin films via combining nano-imprint lithography with block copolymer assisted sol-gel templating. *Journal of Materials Chemistry A* **1**, 7870–7873 (2013).
- Guo, S., Herzig, E. M., Naumann, A., **Tainter, D. Gregory**, Perlich, J. & Müller-Buschbaum, P. Influence of solvent and solvent additive on the morphology of PTB7 films probed via X-ray scattering. *The Journal of Physical Chemistry B* **118**, 344–350 (2013).

References

1. IEA. *World Energy Outlook 2017* (Organisation for Economic Co-operation and Development, OECD, 2017).
2. Sargent, E. H. Colloidal quantum dot solar cells. *Nature Photonics* **6**, 133 (2012).
3. *Digest of UK Energy Statistics* (Department for Business, Energy & Industrial Strategy, 2017).
4. Philipps, S. *Photovoltaics Report* (Fraunhofer Institute for Solar Energy Systems, 2018).
5. Jeon, N. J., Na, H., Jung, E. H., Yang, T.-Y., Lee, Y. G., Kim, G., Shin, H.-W., Seok, S. I., Lee, J. & Seo, J. A fluorene-terminated hole-transporting material for highly efficient and stable perovskite solar cells. *Nature Energy* **3**, 682 (2018).
6. Yoshikawa, K., Kawasaki, H., Yoshida, W., Irie, T., Konishi, K., Nakano, K., Uto, T., Adachi, D., Kanematsu, M., Uzu, H. & Yamamoto, K. Silicon heterojunction solar cell with interdigitated back contacts for a photoconversion efficiency over 26%. *Nature Energy* **2** (2017).
7. Wells, H. L. Über die Cäsium-und Kalium-Bleihalogenide. *Zeitschrift für Anorganische und Allgemeine Chemie* **3**, 195–210 (1893).
8. Møller, C. K. Crystal structure and photoconductivity of caesium plumbahalides. *Nature* **182**, 1436 (1958).
9. Weber, D. $\text{CH}_3\text{NH}_3\text{PbX}_3$, ein Pb (II)-System mit kubischer Perowskitstruktur/
 $\text{CH}_3\text{NH}_3\text{PbX}_3$, a Pb (II)-system with cubic perovskite structure. *Zeitschrift für Naturforschung B* **33**, 1443–1445 (1978).
10. Mitzi, D. B. Synthesis, structure, and properties of organic-inorganic perovskites and related materials. *Progress in Inorganic Chemistry, Volume 48*, 1–121 (2007).
11. Kojima, A., Teshima, K., Shirai, Y. & Miyasaka, T. Organometal halide perovskites as visible-light sensitizers for photovoltaic cells. *Journal of the American Chemical Society* **131**, 6050–6051 (2009).
12. Lee, M. M., Teuscher, J., Miyasaka, T., Murakami, T. N. & Snaith, H. J. Efficient hybrid solar cells based on meso-superstructured organometal halide perovskites. *Science*, 1228604 (2012).
13. Service, R. Perovskite solar cells gear up to go commercial. *Science* **354**, 1214 (2016).

14. Grinberg, I., West, D. V., Torres, M., Gou, G., Stein, D. M., Wu, L., Chen, G., Gallo, E. M., Akbashev, A. R., Davies, P. K. *et al.* Perovskite oxides for visible-light-absorbing ferroelectric and photovoltaic materials. *Nature* **503**, 509 (2013).
15. Onoda-Yamamuro, N., Matsuo, T. & Suga, H. Calorimetric and IR spectroscopic studies of phase transitions in methylammonium trihalogenoplumbates (II). *Journal of Physics and Chemistry of Solids* **51**, 1383–1395 (1990).
16. Poglitsch, A. & Weber, D. Dynamic disorder in methylammonium trihalogenoplumbates (II) observed by millimeter-wave spectroscopy. *The Journal of Chemical Physics* **87**, 6373–6378 (1987).
17. Green, M. A., Ho-Baillie, A. & Snaith, H. J. The emergence of perovskite solar cells. *Nature Photonics* **8**, 506–514 (2014).
18. Sutter-Fella, C. M., Li, Y., Amani, M., Ager III, J. W., Toma, F. M., Yablonovitch, E., Sharp, I. D. & Javey, A. High photoluminescence quantum yield in bandgap tunable bromide containing mixed halide perovskites. *Nano Letters* **16**, 800–806 (2015).
19. Comin, R., Walters, G., Thibau, E. S., Voznyy, O., Lu, Z.-H. & Sargent, E. H. Structural, optical, and electronic studies of wide-bandgap lead halide perovskites. *Journal of Materials Chemistry C* **3**, 8839–8843 (2015).
20. Jeon, N. J., Noh, J. H., Yang, W. S., Kim, Y. C., Ryu, S., Seo, J. & Seok, S. I. Compositional engineering of perovskite materials for high-performance solar cells. *Nature* **517**, 476 (2015).
21. Colella, S., Mosconi, E., Fedeli, P., Listorti, A., Gazza, F., Orlandi, F., Ferro, P., Besagni, T., Rizzo, A., Calestani, G. *et al.* MAPbI_{3-x}Cl_x Mixed Halide Perovskite for Hybrid Solar Cells: The Role of Chloride as Dopant on the Transport and Structural Properties. *Chemistry of Materials* **25**, 4613–4618 (2013).
22. Zhang, M., Yu, H., Lyu, M., Wang, Q., Yun, J.-H. & Wang, L. Composition-dependent photoluminescence intensity and prolonged recombination lifetime of perovskite CH₃NH₃PbBr_{3-x}Cl_x films. *Chemical Communications* **50**, 11727–11730 (2014).
23. Swarnkar, A., Marshall, A. R., Sanehira, E. M., Chernomordik, B. D., Moore, D. T., Christians, J. A., Chakrabarti, T. & Luther, J. M. Quantum dot-induced phase stabilization of α -CsPbI₃ perovskite for high-efficiency photovoltaics. *Science* **354**, 92–95 (2016).
24. Saliba, M., Matsui, T., Seo, J.-Y., Domanski, K., Correa-Baena, J.-P., Nazeeeruddin, M. K., Zakeeruddin, S. M., Tress, W., Abate, A., Hagfeldt, A. *et al.* Cesium-containing triple cation perovskite solar cells: improved stability, reproducibility and high efficiency. *Energy & Environmental Science* **9**, 1989–1997 (2016).
25. Slavney, A. H., Hu, T., Lindenberg, A. M. & Karunadasa, H. I. A bismuth-halide double perovskite with long carrier recombination lifetime for photovoltaic applications. *Journal of the American Chemical Society* **138**, 2138–2141 (2016).

26. Koh, T. M., Krishnamoorthy, T., Yantara, N., Shi, C., Leong, W. L., Boix, P. P., Grimsdale, A. C., Mhaisalkar, S. G. & Mathews, N. Formamidinium tin-based perovskite with low E_g for photovoltaic applications. *Journal of Materials Chemistry A* **3**, 14996–15000 (2015).
27. Shao, S., Liu, J., Portale, G., Fang, H.-H., Blake, G. R., ten Brink, G. H., Koster, L. J. A. & Loi, M. A. Highly Reproducible Sn-Based Hybrid Perovskite Solar Cells with 9% Efficiency. *Advanced Energy Materials* **8**, 1702019 (2018).
28. Zhao, Z., Gu, F., Li, Y., Sun, W., Ye, S., Rao, H., Liu, Z., Bian, Z. & Huang, C. Mixed-Organic-Cation Tin Iodide for Lead-Free Perovskite Solar Cells with an Efficiency of 8.12%. *Advanced Science* **4**, 1700204 (2017).
29. Rühle, S. Tabulated values of the Shockley–Queisser limit for single junction solar cells. *Solar Energy* **130**, 139–147 (2016).
30. Lin, Q., Armin, A., Nagiri, R. C. R., Burn, P. L. & Meredith, P. Electro-optics of perovskite solar cells. *Nature Photonics* **9**, 106–112 (2015).
31. Yu, P. Y. & Cardona, M. *Fundamentals of Semiconductors* **3-6**, 14 (Springer, 1996).
32. Callaway, J. *Energy Band Theory* 3–5 (Academic Press Inc., 1964).
33. Kittel, C. *Introduction to Solid State Physics* (John Wiley & Sons Ltd., 1986).
34. Parr, R. G. Density functional theory. *Annual Review of Physical Chemistry* **34**, 631–656 (1983).
35. Mosconi, E., Umari, P. & De Angelis, F. Electronic and optical properties of MAPbX₃ perovskites (X= I, Br, Cl): a unified DFT and GW theoretical analysis. *Physical Chemistry Chemical Physics* **18**, 27158–27164 (2016).
36. He, Y. & Galli, G. Perovskites for solar thermoelectric applications: A first principle study of CH₃NH₃AI₃ (A= Pb and Sn). *Chemistry of Materials* **26**, 5394–5400 (2014).
37. Menéndez-Proupin, E., Palacios, P., Wahnón, P. & Conesa, J. Self-consistent relativistic band structure of the CH₃NH₃PbI₃ perovskite. *Physical Review B* **90**, 045207 (2014).
38. Amat, A., Mosconi, E., Ronca, E., Quarti, C., Umari, P., Nazeeruddin, M. K., Grätzel, M. & De Angelis, F. Cation-induced band-gap tuning in organohalide perovskites: interplay of spin–orbit coupling and octahedra tilting. *Nano Letters* **14**, 3608–3616 (2014).
39. Even, J., Pedesseau, L., Jancu, J.-M. & Katan, C. Importance of spin–orbit coupling in hybrid organic/inorganic perovskites for photovoltaic applications. *The Journal of Physical Chemistry Letters* **4**, 2999–3005 (2013).
40. Zheng, F., Tan, L. Z., Liu, S. & Rappe, A. M. Rashba spin–orbit coupling enhanced carrier lifetime in CH₃NH₃PbI₃. *Nano Letters* **15**, 7794–7800 (2015).
41. Grundmann, M. *The Physics of Semiconductors: An Introduction Including Nanophysics and Applications* (Springer, 2015).
42. Urbach, F. The long-wavelength edge of photographic sensitivity and of the electronic absorption of solids. *Physical Review* **92**, 1324 (1953).

43. Hoke, E. T., Slotcavage, D. J., Dohner, E. R., Bowring, A. R., Karunadasa, H. I. & McGehee, M. D. Reversible photo-induced trap formation in mixed-halide hybrid perovskites for photovoltaics. *Chemical Science* **6**, 613–617 (2015).
44. Zhai, Y., Sheng, C. X., Zhang, C. & Vardeny, Z. V. Ultrafast spectroscopy of photoexcitations in organometal trihalide perovskites. *Advanced Functional Materials* **26**, 1617–1627 (2016).
45. Stranks, S. D., Burlakov, V. M., Leijtens, T., Ball, J. M., Goriely, A. & Snaith, H. J. Recombination kinetics in organic-inorganic perovskites: excitons, free charge, and subgap states. *Physical Review Applied* **2**, 034007 (2014).
46. Sheng, C., Zhang, C., Zhai, Y., Mielczarek, K., Wang, W., Ma, W., Zakhidov, A. & Vardeny, Z. V. Exciton versus free carrier photogeneration in organometal trihalide perovskites probed by broadband ultrafast polarization memory dynamics. *Physical Review Letters* **114**, 116601 (2015).
47. Deschler, F. *et al.* High photoluminescence efficiency and optically pumped lasing in solution-processed mixed halide perovskite semiconductors. *Journal of Physical Chemistry Letters* **5**, 1421–1426 (2014).
48. Brenner, T. M., Egger, D. A., Kronik, L., Hodes, G. & Cahen, D. Hybrid organic-inorganic perovskites: low-cost semiconductors with intriguing charge-transport properties. *Nature Reviews Materials* **1**, 15007 (Jan. 2016).
49. D’Innocenzo, V., Grancini, G., Alcocer, M. J., Kandada, A. R. S., Stranks, S. D., Lee, M. M., Lanzani, G., Snaith, H. J. & Petrozza, A. Excitons versus free charges in organo-lead tri-halide perovskites. *Nature Comm.* **5**, 3586 (2014).
50. Miyata, A., Mitioglu, A., Plochocka, P., Portugall, O., Wang, J. T.-W., Stranks, S. D., Snaith, H. J. & Nicholas, R. J. Direct measurement of the exciton binding energy and effective masses for charge carriers in organic-inorganic tri-halide perovskites. *Nature Physics* **11**, 582–587 (2015).
51. Etienne, T., Mosconi, E. & De Angelis, F. Dynamical origin of the rashba effect in organohalide lead perovskites: A key to suppressed carrier recombination in perovskite solar cells? *The Journal of Physical Chemistry Letters* **7**, 1638–1645 (2016).
52. Azarhoosh, P., McKechnie, S., Frost, J. M., Walsh, A. & Van Schilfgaarde, M. Research Update: Relativistic origin of slow electron-hole recombination in hybrid halide perovskite solar cells. *APL Materials* **4**, 091501 (2016).
53. Niesner, D., Wilhelm, M., Levchuk, I., Osvet, A., Shrestha, S., Batentschuk, M., Brabec, C. & Fauster, T. Giant rashba splitting in $\text{CH}_3\text{NH}_3\text{PbBr}_3$ organic-inorganic perovskite. *Physical Review Letters* **117**, 126401 (2016).
54. Davies, C. L., Filip, M. R., Patel, J. B., Crothers, T. W., Verdi, C., Wright, A. D., Milot, R. L., Giustino, F., Johnston, M. B. & Herz, L. M. Bimolecular recombination in methylammonium lead triiodide perovskite is an inverse absorption process. *Nature Communications* **9**, 293 (2018).
55. Barker, A. J. *et al.* Defect-Assisted Photoinduced Halide Segregation in Mixed-Halide Perovskite Thin Films. *ACS Energy Letters* **2**, 1416–1424 (2017).

56. DeQuilettes, D. W., Zhang, W., Burlakov, V. M., Graham, D. J., Leijtens, T., Osherov, A., Bulović, V., Snaith, H. J., Ginger, D. S. & Stranks, S. D. Photo-induced halide redistribution in organic-inorganic perovskite films. *Nature Communications* **7**, 11683 (May 2016).
57. Meloni, S., Moehl, T., Tress, W., Franckevičius, M., Saliba, M., Lee, Y. H., Gao, P., Nazeeruddin, M. K., Zakeeruddin, S. M., Rothlisberger, U. *et al.* Ionic polarization-induced current–voltage hysteresis in $\text{CH}_3\text{NH}_3\text{PbX}_3$ perovskite solar cells. *Nature Communications* **7**, 10334 (2016).
58. Unger, E., Hoke, E., Bailie, C., Nguyen, W., Bowring, A., Heumüller, T., Christoforo, M. & McGehee, M. Hysteresis and transient behavior in current–voltage measurements of hybrid-perovskite absorber solar cells. *Energy & Environmental Science* **7**, 3690–3698 (2014).
59. Turren-Cruz, S.-H., Saliba, M., Mayer, M. T., Juárez-Santiesteban, H., Mathew, X., Nienhaus, L., Tress, W., Erodici, M. P., Sher, M.-J., Bawendi, M. G. *et al.* Enhanced charge carrier mobility and lifetime suppress hysteresis and improve efficiency in planar perovskite solar cells. *Energy & Environmental Science* **11**, 78–86 (2018).
60. Wang, C., Zhao, D., Yu, Y., Shrestha, N., Grice, C. R., Liao, W., Cimaroli, A. J., Chen, J., Ellingson, R. J., Zhao, X. *et al.* Compositional and morphological engineering of mixed cation perovskite films for highly efficient planar and flexible solar cells with reduced hysteresis. *Nano Energy* **35**, 223–232 (2017).
61. Tress, W., Marinova, N., Moehl, T., Zakeeruddin, S. M., Nazeeruddin, M. K. & Grätzel, M. Understanding the rate-dependent J–V hysteresis, slow time component, and aging in $\text{CH}_3\text{NH}_3\text{PbI}_3$ perovskite solar cells: the role of a compensated electric field. *Energy & Environmental Science* **8**, 995–1004 (2015).
62. Abdi-Jalebi, M. *et al.* Maximizing and stabilizing luminescence from halide perovskites with potassium passivation. *Nature* **555**, 497–501 (Mar. 2018).
63. Zhao, C., Chen, B., Qiao, X., Luan, L., Lu, K. & Hu, B. Revealing underlying processes involved in light soaking effects and hysteresis phenomena in perovskite solar cells. *Advanced Energy Materials* **5** (2015).
64. Zhang, T., Cheung, S. H., Meng, X., Zhu, L., Bai, Y., Ho, C. H. Y., Xiao, S., Xue, Q., So, S. K. & Yang, S. Pinning Down the Anomalous Light Soaking Effect toward High-Performance and Fast-Response Perovskite Solar Cells: The Ion-Migration-Induced Charge Accumulation. *The Journal of Physical Chemistry Letters* **8**, 5069–5076 (2017).
65. Tsai, H., Asadpour, R., Blancon, J.-C., Stoumpos, C. C., Durand, O., Strzalka, J. W., Chen, B., Verduzco, R., Ajayan, P. M., Tretiak, S. *et al.* Light-induced lattice expansion leads to high-efficiency perovskite solar cells. *Science* **360**, 67–70 (2018).
66. Brenes, R. *et al.* Metal Halide Perovskite Polycrystalline Films Exhibiting Properties of Single Crystals. *Joule* **1**, 155–167 (2017).
67. Tian, Y., Peter, M., Unger, E., Abdellah, M., Zheng, K., Pullerits, T., Yartsev, A., Sundström, V. & Scheblykin, I. G. Mechanistic insights into perovskite photoluminescence enhancement: light curing with oxygen can boost yield thousandfold. *Physical Chemistry Chemical Physics* **17**, 24978–24987 (2015).

68. Desa, M. K. M., Sapeai, S., Azhari, A. W., Sopian, K., Sulaiman, M. Y., Amin, N. & Zaidi, S. H. Silicon back contact solar cell configuration: A pathway towards higher efficiency. *Renewable and Sustainable Energy Reviews* **60**, 1516–1532 (2016).
69. Ansari, M. I. H., Qurashi, A. & Nazeeruddin, M. K. Frontiers, opportunities, and challenges in perovskite solar cells: a critical review. *Journal of Photochemistry and Photobiology C: Photochemistry Reviews* **35**, 1–24 (2018).
70. Zhu, K., Miyasaka, T., Kim, J. Y. & Mora-Sero, I. Trend of perovskite solar cells: dig deeper to build higher. *The Journal of Physical Chemistry Letters* **6**, 2315–2317 (2015).
71. Ciesielski, R., Schäfer, F., Hartmann, N. F., Giesbrecht, N., Bein, T., Docampo, P. & Hartschuh, A. Grain boundaries act as solid walls for charge carrier diffusion in large crystal MAPbI₃ thin films. *ACS Applied Materials and Interfaces* **10**, 7974–7981 (2018).
72. Yang, M., Zeng, Y., Li, Z., Kim, D. H., Jiang, C.-S., van de Lagemaat, J. & Zhu, K. Do grain boundaries dominate nonradiative recombination in CH₃NH₃PbI₃ perovskite thin films? *Phys. Chem. Chem. Phys.* **19**, 5043–5050 (2017).
73. Correa-Baena, J.-P., Tress, W., Domanski, K., Anaraki, E. H., Turren-Cruz, S.-H., Roose, B., Boix, P. P., Grätzel, M., Saliba, M., Abate, A. & Hagfeldt, A. Identifying and suppressing interfacial recombination to achieve high open-circuit voltage in perovskite solar cells. *Energy Environ. Sci.* **10**, 1207–1212 (2017).
74. Yun, J. S., Ho-Baillie, A., Huang, S., Woo, S. H., Heo, Y., Seidel, J., Huang, F., Cheng, Y.-B. & Green, M. A. Benefit of grain boundaries in organic–inorganic halide planar perovskite solar cells. *The Journal of Physical Chemistry Letters* **6**, 875–880 (2015).
75. Chen, Q., De Marco, N., Yang, Y. M., Song, T.-B., Chen, C.-C., Zhao, H., Hong, Z., Zhou, H. & Yang, Y. Under the spotlight: The organic–inorganic hybrid halide perovskite for optoelectronic applications. *Nano Today* **10**, 355–396 (2015).
76. Liu, M., Johnston, M. B. & Snaith, H. J. Efficient planar heterojunction perovskite solar cells by vapour deposition. *Nature* **501**, 395 (2013).
77. Zhu, X., Yang, D., Yang, R., Yang, B., Yang, Z., Ren, X., Zhang, J., Niu, J., Feng, J. & Liu, S. F. Superior stability for perovskite solar cells with 20% efficiency using vacuum co-evaporation. *Nanoscale* **9**, 12316–12323 (2017).
78. Chen, Q., Zhou, H., Hong, Z., Luo, S., Duan, H.-S., Wang, H.-H., Liu, Y., Li, G. & Yang, Y. Planar heterojunction perovskite solar cells via vapor-assisted solution process. *Journal of the American Chemical Society* **136**, 622–625 (2013).
79. Shi, D., Adinolfi, V., Comin, R., Yuan, M., Alarousu, E., Buin, A., Chen, Y., Hoogland, S., Rothenberger, A., Katsiev, K. *et al.* Low trap-state density and long carrier diffusion in organolead trihalide perovskite single crystals. *Science* **347**, 519–522 (2015).
80. Saidaminov, M. I., Abdelhady, A. L., Murali, B., Alarousu, E., Burlakov, V. M., Peng, W., Dursun, I., Wang, L., He, Y., Maculan, G. *et al.* High-quality bulk hybrid perovskite single crystals within minutes by inverse temperature crystallization. *Nature Communications* **6**, 7586 (2015).

81. Fang, H.-H., Raissa, R., Abdu-Aguye, M., Adjokatse, S., Blake, G. R., Even, J. & Loi, M. A. Photophysics of organic–inorganic hybrid lead iodide perovskite single crystals. *Advanced Functional Materials* **25**, 2378–2385 (2015).
82. Fang, Y., Dong, Q., Shao, Y., Yuan, Y. & Huang, J. Highly narrowband perovskite single-crystal photodetectors enabled by surface-charge recombination. *Nature Photonics* **9**, 679–686 (Oct. 2015).
83. Semonin, O. E., Elbaz, G. A., Straus, D. B., Hull, T. D., Paley, D. W., Van Der Zande, A. M., Hone, J. C., Kymissis, I., Kagan, C. R., Roy, X. & Owen, J. S. Limits of Carrier Diffusion in n-Type and p-Type CH₃NH₃PbI₃ Perovskite Single Crystals. *Journal of Physical Chemistry Letters* **7**, 3510–3518 (2016).
84. Sze, S. M. & Ng, K. K. *Physics of Semiconductor Devices* (John Wiley & Sons, 2006).
85. Wolfe, C. M., Stillman, G. E. & Lindley, W. T. Electron mobility in High-Purity GaAs. *Journal of Applied Physics* **41**, 3088–3091 (1970).
86. Lundstrom, M. *Fundamentals of Carrier Transport*. 2000
87. Mayadas, A. & Shatzkes, M. Electrical-resistivity model for polycrystalline films: the case of arbitrary reflection at external surfaces. *Physical Review B* **1**, 1382 (1970).
88. Wang, Y., Zhang, Y., Zhang, P. & Zhang, W. High intrinsic carrier mobility and photon absorption in the perovskite CH₃NH₃PbI₃. *Physical Chemistry Chemical Physics* **17**, 11516–11520 (2015).
89. Yu, Z.-G. Rashba effect and carrier mobility in hybrid organic–inorganic perovskites. *The Journal of Physical Chemistry Letters* **7**, 3078–3083 (2016).
90. Peng, J., Chen, Y., Zheng, K., Pullerits, T. & Liang, Z. Insights into charge carrier dynamics in organo-metal halide perovskites: from neat films to solar cells. *Chemical Society Reviews* **46**, 5714–5729 (2017).
91. Salim, T., Kadro, J., Khuc, M.-T., Haselsberger, R. *et al.* Elucidating the role of disorder and free-carrier recombination kinetics in CH₃NH₃PbI₃ perovskite films. *Nature Communications* **6**, 7903 (2015).
92. Wehrenfennig, C., Eperon, G. E., Johnston, M. B., Snaith, H. J. & Herz, L. M. High charge carrier mobilities and lifetimes in organolead trihalide perovskites. *Advanced Materials* **26**, 1584–1589 (2014).
93. Ponseca Jr, C. S., Savenije, T. J., Abdellah, M., Zheng, K., Yartsev, A., Pascher, T., Harlang, T., Chabera, P., Pullerits, T., Stepanov, A. *et al.* Organometal halide perovskite solar cell materials rationalized: ultrafast charge generation, high and microsecond-long balanced mobilities, and slow recombination. *Journal of the American Chemical Society* **136**, 5189–5192 (2014).
94. Milot, R. L., Eperon, G. E., Snaith, H. J., Johnston, M. B. & Herz, L. M. Temperature-dependent charge-carrier dynamics in CH₃NH₃PbI₃ perovskite thin films. *Advanced Functional Materials* **25**, 6218–6227 (2015).
95. Valverde-Chávez, D. A., Ponseca, C. S., Stoumpos, C. C., Yartsev, A., Kanatzidis, M. G., Sundström, V. & Cooke, D. G. Intrinsic femtosecond charge generation dynamics in single crystal CH₃NH₃PbI₃. *Energy & Environmental Science* **8**, 3700–3707 (2015).

96. Oga, H., Saeki, A., Ogomi, Y., Hayase, S. & Seki, S. Improved understanding of the electronic and energetic landscapes of perovskite solar cells: high local charge carrier mobility, reduced recombination, and extremely shallow traps. *Journal of the American Chemical Society* **136**, 13818–13825 (2014).
97. Chen, Y., Peng, J., Su, D., Chen, X. & Liang, Z. Efficient and balanced charge transport revealed in planar perovskite solar cells. *ACS Applied Materials & Interfaces* **7**, 4471–4475 (2015).
98. Chin, X. Y., Cortecchia, D., Yin, J., Bruno, A. & Soci, C. Lead iodide perovskite light-emitting field-effect transistor. *Nature Communications* **6**, 7383 (2015).
99. Saidaminov, M. I., Adinolfi, V., Comin, R., Abdelhady, A. L., Peng, W., Dursun, I., Yuan, M., Hoogland, S., Sargent, E. H. & Bakr, O. M. Planar-integrated single-crystalline perovskite photodetectors. *Nature Communications* **6**, 8724 (2015).
100. Ginting, R. T., Jung, E.-S., Jeon, M.-K., Jin, W.-Y., Song, M. & Kang, J.-W. Low-temperature operation of perovskite solar cells: With efficiency improvement and hysteresis-less. *Nano Energy* **27**, 569–576 (2016).
101. Xiao, Z., Bi, C., Shao, Y., Dong, Q., Wang, Q., Yuan, Y., Wang, C., Gao, Y. & Huang, J. Efficient, high yield perovskite photovoltaic devices grown by interdiffusion of solution-processed precursor stacking layers. *Energy & Environmental Science* **7**, 2619–2623 (2014).
102. Peng, J., Sun, Y., Chen, Y., Yao, Y. & Liang, Z. Light and Thermally Induced Evolutional Charge Transport in $\text{CH}_3\text{NH}_3\text{PbI}_3$ Perovskite Solar Cells. *ACS Energy Letters* **1**, 1000–1006 (2016).
153. Grill, I., Aygüler, M. F., Bein, T., Docampo, P., Hartmann, N. F., Handloser, M. & Hartschuh, A. Charge Transport Limitations in Perovskite Solar Cells: The Effect of Charge Extraction Layers. *ACS Applied Materials & Interfaces* **9**, 37655–37661 (2017).
103. Senanayak, S. P. *et al.* Understanding charge transport in lead iodide perovskite thin-film field-effect transistors. *Science Advances* **3**, e1601935 (2017).
104. Chen, Y., Yi, H. T., Wu, X., Haroldson, R., Gartstein, Y. N., Rodionov, Y. I., Tikhonov, K. S., Zakhidov, A., Zhu, X.-Y. & Podzorov, V. Extended carrier lifetimes and diffusion in hybrid perovskites revealed by Hall effect and photoconductivity measurements. *Nature Communications* **7**, 12253 (2016).
105. Richter, J. M., Branchi, F., Valduga De Almeida Camargo, F., Zhao, B., Friend, R. H., Cerullo, G. & Deschler, F. Ultrafast carrier thermalization in lead iodide perovskite probed with two-dimensional electronic spectroscopy. *Nature Communications* **8**, 1–7 (2017).
106. Yang, Y., Yan, Y., Yang, M., Choi, S., Zhu, K., Luther, J. M. & Beard, M. C. Low surface recombination velocity in solution-grown $\text{CH}_3\text{NH}_3\text{PbBr}_3$ perovskite single crystal. *Nature Communications* **6**, 7961 (2015).
107. Guo, Z., Manser, J. S., Wan, Y., Kamat, P. V. & Huang, L. Spatial and temporal imaging of long-range charge transport in perovskite thin films by ultrafast microscopy. *Nature Communications* **6**, 7471 (2015).

108. DeQuilettes, D. W., Jariwala, S., Burke, S., Ziffer, M. E., Wang, J. T.-W., Snaith, H. J. & Ginger, D. S. Tracking Photoexcited Carriers in Hybrid Perovskite Semiconductors: Trap-Dominated Spatial Heterogeneity and Diffusion. *ACS Nano* **11**, 11488–11496 (2017).
109. Tian, W., Cui, R., Leng, J., Liu, J., Li, Y., Zhao, C., Zhang, J., Deng, W., Lian, T. & Jin, S. Limiting Perovskite Solar Cell Performance by Heterogeneous Carrier Extraction. *Angewandte Chemie* **55**, 13067–13071 (2016).
110. Stranks, S. D., Eperon, G. E., Grancini, G., Menelaou, C., Alcocer, M. J. P., Leijtens, T., Herz, L. M., Petrozza, A. & Snaith, H. J. Electron-hole diffusion lengths exceeding 1 micrometer in an organometal trihalide perovskite absorber. *Science* **342**, 341–344 (2013).
111. Blancon, J.-C., Nie, W., Neukirch, A. J., Gupta, G., Tretiak, S., Cognet, L., Mohite, A. D. & Crochet, J. J. The Effects of Electronic Impurities and Electron–Hole Recombination Dynamics on Large-Grain Organic–Inorganic Perovskite Photovoltaic Efficiencies. *Advanced Functional Materials* **26**, 4283–4292 (2016).
112. Pazos-Outon, L. M. *et al.* Photon recycling in lead iodide perovskite solar cells. *Science* **351**, 1430–1434 (2016).
113. Wilson, T. & McCabe, E. M. Theory of optical beam induced current images of defects in semiconductors. *Journal of Applied Physics* **61** (1987).
114. Pauls, K., Mitchell, K. & Chesarek, W. *The effect of dislocations on the performance of silicon solar cells in Photovoltaic Specialists Conference, 1993., Conference Record of the Twenty Third IEEE* (1993), 209–213.
115. Camanzi, A., Parretta, A., Garozzo, M. & Vittori, M. OBIC and EBIC investigations on GaAs shallow homojunction solar cells. *Solar Energy Materials* **17**, 457–469 (1988).
116. Eperon, G. E., Moerman, D. & Ginger, D. S. Anticorrelation between Local Photoluminescence and Photocurrent Suggests Variability in Contact to Active Layer in Perovskite Solar Cells. *ACS Nano* **10**, 10258–10266 (2016).
117. Edri, E., Kirmayer, S., Mukhopadhyay, S., Gartsman, K., Hodes, G. & Cahen, D. Elucidating the charge carrier separation and working mechanism of $\text{CH}_3\text{NH}_3\text{PbI}_{3-x}\text{Cl}_x$ perovskite solar cells. *Nature Communications* **5**, 3461 (2014).
118. Van Roosbroeck, W. & Shockley, W. Photon-radiative recombination of electrons and holes in germanium. *Physical Review* **94**, 1558 (1954).
119. Nelson, J. *The Physics of Solar Cells* (World Scientific Publishing Company, 2003).
120. Shockley, W. & Read, W. T. Statistics of the Recombination of Holes and Electrons. *Physical Review* **87**, 835–842 (1952).
121. Hall, R. N. Electron-hole recombination in germanium. *Physical Review* **87**, 387 (1952).
122. O’Kane, S. E., Richardson, G., Pockett, A., Niemann, R. G., Cave, J. M., Sakai, N., Eperon, G. E., Snaith, H. J., Foster, J. M., Cameron, P. J. *et al.* Measurement and modelling of dark current decay transients in perovskite solar cells. *Journal of Materials Chemistry C* **5**, 452–462 (2017).

123. Richter, J. M., Abdi-Jalebi, M., Sadhanala, A., Tabachnyk, M., Rivett, J. P., Pazos-Outón, L. M., Gödel, K. C., Price, M., Deschler, F. & Friend, R. H. Enhancing photoluminescence yields in lead halide perovskites by photon recycling and light out-coupling. *Nature Communications* **7**, 13941 (2016).
124. Yablonovitch, E., Allara, D. L., Chang, C. C., Gmitter, T. & Bright, T. B. Unusually Low Surface-Recombination Velocity on Silicon and Germanium Surfaces. *Physical Review Letters* **57**, 249–252 (1986).
125. DeQuilettes, D. W., Koch, S., Burke, S., Paranji, R. K., Shropshire, A. J., Ziffer, M. E. & Ginger, D. S. Photoluminescence Lifetimes Exceeding 8 μ s and Quantum Yields Exceeding 30% in Hybrid Perovskite Thin Films by Ligand Passivation. *ACS Energy Letters* **1**, 438–444 (2016).
126. Abate, A., Saliba, M., Hollman, D. J., Stranks, S. D., Wojciechowski, K., Avolio, R., Grancini, G., Petrozza, A. & Snaith, H. J. Supramolecular halogen bond passivation of organic-inorganic halide perovskite solar cells. *Nano Letters* **14**, 3247–3254 (2014).
127. Noel, N. K., Abate, A., Stranks, S. D., Parrott, E. S., Burlakov, V. M., Goriely, A. & Snaith, H. J. Enhanced photoluminescence and solar cell performance via Lewis base passivation of organic-inorganic lead halide perovskites. *ACS Nano* **8**, 9815–9821 (2014).
128. Saliba, M., Matsui, T., Domanski, K., Seo, J.-Y., Ummadisingu, A., Zakeeruddin, S. M., Correa-Baena, J.-P., Tress, W. R., Abate, A., Hagfeldt, A. & Grätzel, M. Incorporation of rubidium cations into perovskite solar cells improves photovoltaic performance. *Science* **354**, 4–8 (2016).
129. Shockley, W. The theory of p-n junctions in semiconductors and p-n junction transistors. *Bell Labs Technical Journal* **28**, 435–489 (1949).
130. Olthof, S. & Meerholz, K. Substrate-dependent electronic structure and film formation of MAPbI₃ perovskites. *Scientific Reports* **7**, 40267 (2017).
131. Chapin, D. M., Fuller, C. & Pearson, G. A new silicon p-n junction photocell for converting solar radiation into electrical power. *Journal of Applied Physics* **25**, 676–677 (1954).
132. Shockley, W. & Queisser, H. J. Detailed balance limit of efficiency of p-n junction solar cells. *Journal of applied physics* **32**, 510–519 (1961).
133. Ross, R. T. Some thermodynamics of photochemical systems. *The Journal of Chemical Physics* **46**, 4590–4593 (1967).
134. Miller, O. D., Yablonovitch, E. & Kurtz, S. R. Strong internal and external luminescence as solar cells approach the Shockley–Queisser limit. *IEEE Journal of Photovoltaics* **2**, 303–311 (2012).
135. Yablonovitch, E. Lead halides join the top optoelectronic league. *Science* **351**, 1401–1401 (2016).
136. Lee, Y., Park, C., Balaji, N., Lee, Y.-J. & Dao, V. A. High-efficiency Silicon Solar Cells: A Review. *Israel Journal of Chemistry* **55**, 1050–1063 (2015).
137. Hu, Z., Kapil, G., Shimazaki, H., Pandey, S. S., Ma, T. & Hayase, S. Transparent conductive oxide layer and hole selective layer free back-contacted hybrid perovskite solar cell. *J. Phys. Chem. C* **121**, 4214–4219 (2017).

138. Jumabekov, A. N., Della Gaspera, E., Xu, Z.-Q., Chesman, A. S. R., van Embden, J., Bonke, S. A., Bao, Q., Vak, D. & Bach, U. Back-contacted hybrid organic–inorganic perovskite solar cells. *J. Mater. Chem. C* **4**, 3125–3130 (2016).
139. Anaraki, E. H., Kermanpur, A., Steier, L., Domanski, K., Matsui, T., Tress, W., Saliba, M., Abate, A., Grä, M., Hagfeldt, A. & Correa-Baena, J.-P. Highly efficient and stable planar perovskite solar cells by solution-processed tin oxide. *Energy Environ. Sci.* **3128**, 3128–3134 (2016).
140. Li, C. *et al.* Emission enhancement and intermittency in polycrystalline organolead halide perovskite films. *Molecules* **21**, 1–12 (2016).
141. Cosens, C. A balance-detector for alternating-current bridges. *Proceedings of the Physical Society* **46**, 818 (1934).
142. Michels, W. C. & Curtis, N. L. A pentode lock-in amplifier of high frequency selectivity. *Review of Scientific Instruments* **12**, 444–447 (1941).
143. *Model SR830 DSP Lock-In Amplifier* English. Version 2.5. Stanford Research Systems (Oct. 2011). 178 pp.
144. De Mello, J. C., Wittmann, H. F. & Friend, R. H. An improved experimental determination of external photoluminescence quantum efficiency. *Advanced Materials* **9**, 230–232 (1997).
145. Song, Z., Wathage, S. C., Phillips, A. B., Liyanage, G. K., Khanal, R. R., Tompkins, B. L., Ellingson, R. J. & Heben, M. J. *Investigation of degradation mechanisms of perovskite-based photovoltaic devices using laser beam induced current mapping in Thin Films for Solar and Energy Technology VII* **9561** (2015), 956107.
146. ASTM International. Standard Tables for Reference Solar Spectral Irradiances: Direct Normal and Hemispherical on 37° Tilted Surface. (ASTM G173-03 Reference Spectra Derived from SMARTS v. 2.9.2) (2012).
147. Filimonov, E., Kozhukhovskaia, S., Bogomolova, S. & Shvarts, M. *About significance of absolute photocurrent values determination during the solar cell external quantum efficiency measurements in Journal of Physics: Conference Series* **917** (2017), 052026.
148. Wang, J. *et al.* Interfacial control toward efficient and low-voltage perovskite light-emitting diodes. *Advanced Materials* **27**, 2311–2316 (2015).
149. Tainter, G. D., Hörantner, M. T., Pazos-Outón, L. M., Lamboll, R. D., Āboliņš, H., Leijtens, T., Suhas, M., Friend, R. H., Snaith, H. J., Joyce, H. J. & Felix, D. Long-range charge extraction in back-contact perovskite solar cells via suppressed recombination. *Joule* (**under review**) (2018).
150. Runyan, W. R. *Semiconductor Measurements and Instrumentation* (eds Hicks, T. G. & Strong, L.) 105–129 (McGraw-Hill, New York, 1975).
151. Casey, H. C., Miller, B. I. & Pinkas, E. Variation of minority-carrier diffusion length with carrier concentration in GaAs liquid-phase epitaxial layers. *Journal of Applied Physics* **44**, 1281–1287 (1972).
152. Cahen, D., Abecassis, D. & Soltz, D. Doping of CuInSe₂ Crystals: Evidence for Influence of Thermal Defects. *Chemistry of Materials* **1**, 202–207 (1989).

154. Lin, X., Jumabekov, A. N., Lal, N. N., Pascoe, A. R., Gómez, D. E., Duffy, N. W., Chesman, A. S., Sears, K., Fournier, M., Zhang, Y. *et al.* Dipole-field-assisted charge extraction in metal-perovskite-metal back-contact solar cells. *Nature Communications* **8**, 613 (2017).
155. Jumabekov, A. N., Lloyd, J. A., Bacal, D. M., Bach, U. & Chesman, A. S. Fabrication of Back-Contact Electrodes Using Modified Natural Lithography. *ACS Applied Energy Materials* **1**, 1077–1082 (2018).
156. Lamboll, R. D. & Greenham, N. C. Reduced dimensionality in drift-diffusion models of back-contact solar cells and scanning photocurrent microscopy. *Journal of Applied Physics* **122**, 133106 (2017).
157. Bischak, C. G., Hetherington, C. L., Wu, H., Aloni, S., Ogletree, D. F., Limmer, D. T. & Ginsberg, N. S. Origin of Reversible Photoinduced Phase Separation in Hybrid Perovskites. *Nano Letters* **17**, 1028–1033 (2017).
158. Staub, F., Hempel, H., Hebig, J. C., Mock, J., Paetzold, U. W., Rau, U., Unold, T. & Kirchartz, T. Beyond Bulk Lifetimes: Insights into Lead Halide Perovskite Films from Time-Resolved Photoluminescence. *Phys. Rev. Appl* **6**, 1–13 (2016).
159. Snaith, H. J. & Grätzel, M. Light-enhanced charge mobility in a molecular hole transporter. *Physical Review Letters* **98**, 177402 (2007).
160. Hutter, E. M., Eperon, G. E., Stranks, S. D. & Savenije, T. J. Charge carriers in planar and meso-structured organic–inorganic perovskites: mobilities, lifetimes, and concentrations of trap states. *The Journal of Physical Chemistry Letters* **6**, 3082–3090 (2015).
161. Kim, D. H., Park, J., Li, Z., Yang, M., Park, J.-S., Park, I. J., Kim, J. Y., Berry, J. J., Rumbles, G. & Zhu, K. 300% enhancement of carrier mobility in uniaxial-oriented perovskite films formed by topotactic-oriented attachment. *Advanced Materials* **29** (2017).
162. Liu, S., Wang, L., Lin, W.-C., Sucharitakul, S., Burda, C. & Gao, X. P. Imaging the long transport lengths of photo-generated carriers in oriented perovskite films. *Nano Letters* **16**, 7925–7929 (2016).
163. Leijtens, T., Eperon, G. E., Barker, A. J., Grancini, G., Zhang, W., Ball, J. M., Kandada, A. R. S., Snaith, H. J. & Petrozza, A. Carrier trapping and recombination: the role of defect physics in enhancing the open-circuit voltage of metal halide perovskite solar cells. *Energy Environ. Sci.* **9**, 3472–3481 (2016).
164. Stranks, S. D. Nonradiative losses in metal halide perovskites. *ACS Energy Letters* **2**, 1515–1525 (2017).
165. Price, M. B., Butkus, J., Jellicoe, T. C., Sadhanala, A., Briane, A., Halpert, J. E., Broch, K., Hodgkiss, J. M., Friend, R. H. & Deschler, F. Hot-carrier cooling and photoinduced refractive index changes in organic-inorganic lead halide perovskites. *Nature Communications* **6**, 8420 (2015).
166. Yang, Y., Yang, M., Li, Z., Crisp, R., Zhu, K. & Beard, M. C. Comparison of Recombination Dynamics in $\text{CH}_3\text{NH}_3\text{PbBr}_3$ and $\text{CH}_3\text{NH}_3\text{PbI}_3$ Perovskite Films: Influence of Exciton Binding Energy. *Journal of Physical Chemistry Letters* **6**, 4688–4692 (2015).

167. Sherkar, T. S., Momblona, C., Gil-Escrig, L., Bolink, H. J. & Koster, L. J. A. Improving Perovskite Solar Cells: Insights From a Validated Device Model. *Advanced Energy Materials* **7**, 1602532 (2017).
168. Draguta, S., Thakur, S., Morozov, Y. V., Wang, Y., Manser, J. S., Kamat, P. V. & Kuno, M. Spatially non-uniform trap state densities in solution-processed hybrid perovskite thin films. *The Journal of Physical Chemistry Letters* **7**, 715–721 (2016).
169. Yuan, H., Debroye, E., Janssen, K., Naiki, H., Steuwe, C., Lu, G., Moris, M., Orgiu, E., Uji-i, H., De Schryver, F. *et al.* Degradation of methylammonium lead iodide perovskite structures through light and electron beam driven ion migration. *The Journal of Physical Chemistry Letters* **7**, 561–566 (2016).
170. Guan, X., Hu, W., Haque, M. A., Wei, N., Liu, Z., Chen, A. & Wu, T. Light-Responsive Ion-Redistribution-Induced Resistive Switching in Hybrid Perovskite Schottky Junctions. *Advanced Functional Materials* **28**, 1704665 (2017).
171. Fu, Q., Tang, X., Huang, B., Hu, T., Tan, L., Chen, L. & Chen, Y. Recent progress on the long-term stability of perovskite solar cells. *Advanced Science* **5**, 1700387 (2018).
172. Hu, Y., Hutter, E. M., Rieder, P., Grill, I., Hanisch, J., Aygüler, M. F., Hufnagel, A. G., Handloser, M., Bein, T., Hartschuh, A. *et al.* Understanding the role of cesium and rubidium additives in perovskite solar cells: trap states, charge transport, and recombination. *Advanced Energy Materials*, 1703057 (2018).
173. Dymshits, A., Henning, A., Segev, G., Rosenwaks, Y. & Etgar, L. The electronic structure of metal oxide/organo metal halide perovskite junctions in perovskite based solar cells. *Scientific Reports* **5**, 1–6 (2015).
174. De Quilettes, D. W., Vorpahl, S. M., Stranks, S. D., Nagaoka, H., Eperon, G. E., Ziffer, M. E., Snaith, H. J. & Ginger, D. S. Impact of microstructure on local carrier lifetime in perovskite solar cells. *Science* **348**, 683–686 (2015).
175. Shao, S., Abdu-Aguye, M., Sherkar, T. S., Fang, H.-H., Adjokatse, S., Brink, G. t., Kooi, B. J., Koster, L. J. A. & Loi, M. A. The effect of the microstructure on trap-assisted recombination and light soaking phenomenon in hybrid perovskite solar cells. *Advanced Functional Materials* **26**, 8094–8102 (2016).
176. Pazos-Outón, L. M., Xiao, T. P. & Yablonovitch, E. Fundamental efficiency limit of lead iodide perovskite solar cells. *The Journal of Physical Chemistry Letters* **9**, 1703–1711 (2018).
177. Lu, M., Bowden, S., Das, U. & Birkmire, R. Interdigitated back contact silicon heterojunction solar cell and the effect of front surface passivation. *Applied Physics Letters* **91**, 063507 (2007).
178. Braly, I. L., DeQuilettes, D. W., Pazos-Outón, L. M., Burke, S., Ziffer, M. E., Ginger, D. S. & Hillhouse, H. W. Hybrid perovskite films approaching the radiative limit with over 90% photoluminescence quantum efficiency. *Nature Photonics*, 1 (2018).
179. Teunis, M. B., Lawrence, K. N., Dutta, P., Siegel, A. P. & Sardar, R. Pure white-light emitting ultrasmall organic–inorganic hybrid perovskite nanoclusters. *Nanoscale* **8**, 17433–17439 (2016).

180. Sandberg, O. J., Sundqvist, A., Nyman, M. & Österbacka, R. Relating charge transport, contact properties, and recombination to open-circuit voltage in sandwich-type thin-film solar cells. *Physical Review Applied* **5**, 044005 (2016).
181. Banin, U., Bruchez, M., Alivisatos, A., Ha, T., Weiss, S. & Chemla, D. Evidence for a thermal contribution to emission intermittency in single CdSe/CdS core/shell nanocrystals. *The Journal of Chemical Physics* **110**, 1195–1201 (1999).
182. Baker, T. A., Rouge, J. L. & Nesbitt, D. J. Single molecule studies of quantum dot fluorescence intermittency: Evidence for both dark and light-assisted blinking dynamics. *Molecular Physics* **107**, 1867–1878 (2009).
183. Haase, M., Hübner, C. G., Reuther, E., Herrmann, A., Müllen, K. & Basché, T. Exponential and power-law kinetics in single-molecule fluorescence intermittency. *The Journal of Physical Chemistry B* **108**, 10445–10450 (2004).
184. Tian, Y. *et al.* Giant photoluminescence blinking of perovskite nanocrystals reveals single-trap control of luminescence. *Nano Letters* **15**, 1603–1608 (2015).
185. Merdasa, A., Tian, Y., Camacho, R., Dobrovolsky, A., Debroye, E., Unger, E. L., Hofkens, J., Sundström, V. & Scheblykin, I. G. "Supertrap" at Work: Extremely Efficient Nonradiative Recombination Channels in MAPbI₃ Perovskites Revealed by Luminescence Super-Resolution Imaging and Spectroscopy. *ACS Nano* **11**, 5391–5404 (2017).
186. Okano, M., Endo, M., Wakamiya, A., Yoshita, M., Akiyama, H. & Kanemitsu, Y. Degradation mechanism of perovskite CH₃NH₃PbI₃ diode devices studied by electroluminescence and photoluminescence imaging spectroscopy. *Applied Physics Express* **8**, 102302 (2015).
187. Brenes, R., Eames, C., Bulović, V., Islam, M. S. & Stranks, S. D. The Impact of Atmosphere on the Local Luminescence Properties of Metal Halide Perovskite Grains. *Advanced Materials* **30**, 1706208 (2018).
188. Merdasa, A., Bag, M., Tian, Y., Källman, E., Dobrovolsky, A. & Scheblykin, I. G. Super-resolution luminescence microspectroscopy reveals the mechanism of photoinduced degradation in CH₃NH₃PbI₃ perovskite nanocrystals. *The Journal of Physical Chemistry C* **120**, 10711–10719 (2016).
189. Ahn, N., Kwak, K., Jang, M. S., Yoon, H., Lee, B. Y., Lee, J.-K., Pikhitsa, P. V., Byun, J. & Choi, M. Trapped charge-driven degradation of perovskite solar cells. *Nature Communications* **7**, 13422 (2016).
190. Kang, J. & Schroder, D. Gettering in silicon. *Journal of Applied Physics* **65**, 2974–2985 (1989).